

CHARACTERIZATION OF FRACTURE ROUGHNESS
AND ITS ROLE IN MODELLING THE STRESS-FLOW
BEHAVIOUR OF FRACTURED ROCK

CENTRE FOR NEWFOUNDLAND STUDIES

**TOTAL OF 10 PAGES ONLY
MAY BE XEROXED**

(Without Author's Permission)

DAVID RODNEY BRIGGINS, B.Sc.





National Library
of Canada

Acquisitions and
Bibliographic Services Branch

395 Wellington Street
Ottawa, Ontario
K1A 0N4

Bibliothèque nationale
du Canada

Direction des acquisitions et
des services bibliographiques

395, rue Wellington
Ottawa (Ontario)
K1A 0N4

Voici votre référence

Ceci est votre référence

NOTICE

The quality of this microform is heavily dependent upon the quality of the original thesis submitted for microfilming. Every effort has been made to ensure the highest quality of reproduction possible.

If pages are missing, contact the university which granted the degree.

Some pages may have indistinct print especially if the original pages were typed with a poor typewriter ribbon or if the university sent us an inferior photocopy.

Reproduction in full or in part of this microform is governed by the Canadian Copyright Act, R.S.C. 1970, c. C-30, and subsequent amendments.

AVIS

La qualité de cette microforme dépend grandement de la qualité de la thèse soumise au microfilmage. Nous avons tout fait pour assurer une qualité supérieure de reproduction.

S'il manque des pages, veuillez communiquer avec l'université qui a conféré le grade.

La qualité d'impression de certaines pages peut laisser à désirer, surtout si les pages originales ont été dactylographiées à l'aide d'un ruban usé ou si l'université nous a fait parvenir une photocopie de qualité inférieure.

La reproduction, même partielle, de cette microforme est soumise à la Loi canadienne sur le droit d'auteur, SRC 1970, c. C-30, et ses amendements subséquents.

**CHARACTERIZATION OF FRACTURE ROUGHNESS
AND ITS ROLE IN MODELLING
THE STRESS - FLOW BEHAVIOUR OF FRACTURED ROCK**

BY

© David Rodney Briggins, B.Sc.

A thesis submitted to the School of Graduate
Studies in partial fulfilment of the
requirements for the degree of
Master of Science

Department of Earth Sciences
Memorial University of Newfoundland

1992

St. John's

Newfoundland



National Library
of Canada

Acquisitions and
Bibliographic Services Branch

395 Wellington Street
Ottawa, Ontario
K1A 0N4

Bibliothèque nationale
du Canada

Direction des acquisitions et
des services bibliographiques

395, rue Wellington
Ottawa (Ontario)
K1A 0N4

Ex. 101 - 10/10/1988

Ex. 101 - 10/10/1988

The author has granted an irrevocable non-exclusive licence allowing the National Library of Canada to reproduce, loan, distribute or sell copies of his/her thesis by any means and in any form or format, making this thesis available to interested persons.

L'auteur a accordé une licence irrévocable et non exclusive permettant à la Bibliothèque nationale du Canada de reproduire, prêter, distribuer ou vendre des copies de sa thèse de quelque manière et sous quelque forme que ce soit pour mettre des exemplaires de cette thèse à la disposition des personnes intéressées.

The author retains ownership of the copyright in his/her thesis. Neither the thesis nor substantial extracts from it may be printed or otherwise reproduced without his/her permission.

L'auteur conserve la propriété du droit d'auteur qui protège sa thèse. Ni la thèse ni des extraits substantiels de celle-ci ne doivent être imprimés ou autrement reproduits sans son autorisation.

ISBN 0-315-78081-9

Canada

ABSTRACT

The importance of fracture roughness in the mechanical and hydraulic behaviour of fractured rock has long been recognized but quantitative modelling of its effects has proven to be difficult. This study addresses the characterization of fracture roughness and assesses some of the existing stress-flow models that exist in the literature. As part of the study, laboratory stress-flow tests were carried out on a single, natural fracture in a 20 cm diameter granite core. These were followed by injection of an epoxy resin into the fracture plane at a specified normal stress and flow rate. The resin injection experiment enabled direct measurements and characterization of the roughness of both sides of the fracture, contact area, aperture and void space. Statistical analysis of these parameters indicated that the distributions were skewed towards zero and could be approximated reasonably well by a log-normal distribution. All of the stress-flow models examined, including the parallel plate model, were found to have limited application or required simplifying assumptions with respect to fracture roughness. From the results of this study it is clear that fracture flow theory must take into account both sides of the fracture, the variation and spatial distribution of fracture aperture, and the different scales of roughness that exist.

ACKNOWLEDGEMENTS

Special thanks are extended to Mr. Ken Hayward who helped with sample preparation and testing and to Mr. David Press who prepared the computer programs for statistical analysis of the data as part of the overall Engineering Geology stress-flow laboratory research program. Their assistance was instrumental in the completion of this work and is gratefully acknowledged. I must also thank staff of the Engineering Department machine shop for fabricating various components of the testing system and other colleagues and co-workers with the Earth Sciences Department for helpful discussions on many aspects of the study. I also thank my supervisor, Dr. John Gale, for providing the impetus for the study and the guidance to carry it through to completion. This study was funded by an NSERC operating grant (#A2309) to Dr. Gale. Last, but certainly not least, I thank my wife Kim for providing much needed moral support and persevering through to the end.

TABLE OF CONTENTS

	Page
ABSTRACT	ii
ACKNOWLEDGEMENTS	iii
LIST OF TABLES	vi
LIST OF FIGURES	vii
 Chapter 1 INTRODUCTION	
1.1 Statement of Problem	1
1.2 Objectives and Scope	3
1.3 Background and Previous Work	4
 Chapter 2 EXPERIMENTAL DESIGN AND PROCEDURES	
2.1 Sample Preparation	15
2.2 Stress-Flow Tests	16
2.3 Resin Injection Technique	22
2.4 Resin Analysis Method	24
 Chapter 3 EXPERIMENTAL RESULTS AND DATA ANALYSIS	
3.1 Stress-Flow Results	28
3.2 Characterization of a Rough Fracture	35
3.2.1 Large-scale roughness	35
3.2.2 Small-scale roughness	45
3.2.3 Contact area	55
3.2.4 Aperture and void space	60

**Chapter 4 EVALUATION AND COMPARISON OF STRESS-FLOW
MODELS**

4.1 The Gangi Bed of Nails Model	76
4.2 The Walsh Normal Closure - Conductivity Model	82
4.3 The Swan Normal Closure - Conductivity Model	91
4.4 The Tsang and Witherspoon Void/Asperity Model	100
4.5 The Barton-Bandis Empirical Model	109

Chapter 5 SUMMARY AND CONCLUSIONS

REFERENCES	128
APPENDIX A	137

LIST OF TABLES

- Table 3.1 Stress-flow test results and computed hydraulic apertures for final loading - unloading cycle and resin injection cycle.
- Table 3.2 Summary statistics on large-scale roughness measurements from all fracture profiles combined.
- Table 3.3 Summary statistics on small-scale roughness measurements from all fracture profiles combined.
- Table 3.4 Summary statistics on individual contact length measurements from all fracture profiles combined.
- Table 3.5 Summary statistics on aperture and resin thickness measurements from all fracture profiles combined.
- Table 3.6 Summary statistics on void area and aspect ratio measurements from all fracture profiles combined.
- Table 4.1 Predicted standard deviation of asperity heights, h , from normal stiffness vs. normal stress curve (after Walsh and Grosenbaugh, 1979).
- Table 4.2 Values of h/a_0 used in fitting the Walsh (1981) model to measured stress-flow data.
- Table 4.3 Parameters for the Swan (1983) model derived from linear regression analysis of stress - closure and stress - hydraulic conductivity curves.

LIST OF FIGURES

- Figure 2.1 Schematic of fully instrumented sample for stress-flow testing (after Gale, 1982).
- Figure 2.2 Schematic of stress-flow testing components: (1) loading frame (2) flow system (3) temperature control system and (4) data acquisition system.
- Figure 2.3 Schematic of the resin injection system.
- Figure 2.4 Plan drawing showing the number and location of fracture profiles obtained by cross-sectional cuts through the resin-filled fracture plane.
- Figure 2.5 Examples of 1:1 line drawings of the fracture trace for selected profiles.
- Figure 3.1 Fracture closure as a function of normal stress for the first, second, third, final and resin loading cycles (cycle 1, 2 and 3 data from Gale and Raven, 1980).
- Figure 3.2 Normalized fracture flow rate as a function of normal stress for the first, second, third, final and resin loading cycles (cycle 1, 2 and 3 data from Gale and Raven, 1980).
- Figure 3.3 Computed hydraulic apertures plotted against normalized flow for the first, second, third, final and resin loading cycles (cycle 1, 2 and 3 data from Gale and Raven, 1980).
- Figure 3.4 Roughness profiles for two selected cross-sections. The vertical scale is twice the horizontal scale and a small vertical separation has been added between the two surfaces.
- Figure 3.5 Schematic of the definition of asperity height used for determining asperity height distributions.
- Figure 3.6 Frequency histograms of large-scale asperity heights for top and bottom surfaces of two selected profiles with superimposed normal distribution curves.

- Figure 3.7 Frequency histograms of the natural logarithms of large-scale asperity heights for two selected profiles with superimposed log-normal distribution curves.
- Figure 3.8 A 3-D perspective diagram of the large-scale roughness of the bottom fracture surface created by combining individual profile data.
- Figure 3.9 Schematic of the technique for graphical filtering in which reference lines are fitted to small segments of the fracture profile to remove large-scale roughness effects.
- Figure 3.10 Filtered roughness profiles for both the top and bottom surfaces of profile 80-3DX01 using segment lengths of 30, 20, 10, 5 and 2 mm.
- Figure 3.11 (a) Mean asperity height vs. segment length diagram for profile 80-3DX01 (b) Frequency histogram of small-scale asperity heights for profile 80-3DX01 using a segment length of 3.5 mm.
- Figure 3.12 Mean asperity height vs. segment length diagram for selected profiles.
- Figure 3.13 Frequency histograms of small-scale asperity heights for top and bottom surfaces of all combined profiles with superimposed normal distribution curves.
- Figure 3.14 Frequency histograms of the natural logarithms of small-scale asperity heights for top and bottom surfaces of all combined profiles with superimposed log-normal distribution curves.
- Figure 3.15 (a) Frequency histogram of individual contact lengths from all combined profiles (b) log-normal distribution of contact lengths.
- Figure 3.16 Spatial distribution of contact points across the fracture plane.
- Figure 3.17 Plots of aperture and resin thickness against profile length for two selected profiles. The vertical scale has been exaggerated to bring out the details.
- Figure 3.18 Frequency histograms of aperture and resin thickness from all profiles combined.

- Figure 3.19 Frequency histograms of the natural logarithms of aperture and resin thickness from all profiles combined.
- Figure 3.20 Modified box plots of aperture distributions for selected fracture profiles.
- Figure 3.21 Frequency histograms of (a) void areas and (b) natural logarithm of void areas from all profiles combined. Normal and log-normal distribution curves are shown.
- Figure 3.22 Frequency histograms of (a) aspect ratios and (b) natural logarithms of aspect ratios from all profiles combined. Normal and log-normal distribution curves are shown.
- Figure 3.23 Aperture contour diagram showing the spatial distribution of apertures within the fracture plane. The contour interval is $20 \mu\text{m}$.
- Figure 3.24 Resin thickness contour diagram showing the spatial distribution of resin within the fracture plane. The contour interval is $20 \mu\text{m}$.
- Figure 3.25 A 3-D mesh plot of apertures within the fracture plane. A vertical exaggeration has been added to highlight the aperture differences.
- Figure 4.1 Comparison of Gangi (1978) model curves with stress-flow data from the first loading cycle ($P_1=750 \text{ MPa}$, $m=.06,.07,.08$).
- Figure 4.2 Comparison of Gangi (1978) model curves with stress-flow data from the final loading cycle ($P_1=7500 \text{ MPa}$, $m=.04,.05,.06$).
- Figure 4.3 Normal fracture stiffness as a function of normal stress following the Walsh and Grosenbaugh (1979) model (cycle 1, 2 and 3 data from Gale & Raven, 1980).
- Figure 4.4 Plot of cube-root of hydraulic conductivity vs. logarithm of normal stress following the Walsh (1981) model (cycle 1, 2 and 3 data from Gale and Raven, 1980).
- Figure 4.5 Comparison of the Walsh (1981) model curve with stress-flow data from (a) the second loading cycle, $P_o=30 \text{ MPa}$ and (b) the final loading cycle, $P_o=10 \text{ MPa}$.

- Figure 4.6 Fracture closure vs. logarithm of normal stress following the Swan (1983) model (cycle 1, 2 and 3 data from Gale and Raven, 1980).
- Figure 4.7 Normalized conductivity vs. logarithm of normal stress following the Swan (1983) model (cycle 1, 2 and 3 data from Gale and Raven, 1980).
- Figure 4.8 Comparison of the Swan (1983) model predicted curves with measured stress-flow data from the second loading cycle.
- Figure 4.9 Analytic functions fitted to intact rock and fracture deformation measurements from the final loading cycle following the Tsang & Witherspoon (1981) model.
- Figure 4.10 The 'asperities in contact' function for the final loading cycle following the Tsang and Witherspoon (1981) model.
- Figure 4.11 Comparison of the Tsang and Witherspoon (1981) model predicted curves with measured stress-flow data for the final loading cycle.
- Figure 4.12 Comparison of the Barton-Bandis model curves for four loading cycles with measured stress - fracture closure data (cycle 1, 2 and 3 data from Gale and Raven, 1980).
- Figure 4.13 Comparison of the Barton-Bandis model curves for four loading cycles with measured fracture flow rate data (cycle 1, 2 and 3 data from Gale and Raven, 1980).
- Figure A.1 Surface map of sample showing location of LVDT posts, anchor posts, pressure port and strain gauges with respect to the fracture (modified after Gale and Raven, 1980).

Chapter 1 INTRODUCTION

1.1 Statement of Problem

The word "fracture" is used as a collective term representing any of a series of discontinuous features in rocks such as joints, faults, fissures and bedding planes. Representing as they do a disruption in the continuum of intact rock, fractures have a significant effect on both the mechanical and hydraulic (hydromechanical) properties of rock masses. Changes in the stress conditions of a rock body cause a deformation of the rock - a large part of which is manifest as fracture dilation or fracture closure. In the case of rocks with low matrix permeabilities, fractures constitute the primary flow paths for the flow of fluids through the rock mass.

Much of the work on fracture flow has been based on the parallel plate analogy in which the two sides of the fracture are idealized as smooth, non-contacting, parallel plates. This simplification leads to an expression relating fracture flow rate to an effective hydraulic aperture. Although modifications have been suggested to account for fracture roughness, the parallel plate model has generally been proven not to be applicable to natural fractures subjected to a range of normal stresses (Gale, 1982; Raven and Gale, 1985; Pyrak-Nolte et al., 1987; Gentier, 1990b). As rough fractures close under applied stress, the relationships between fracture roughness, contact area and void space become very significant as fluid movement is restricted to a series of tortuous flow channels within the fracture plane. Clearly, a simple flat plate model for flow is unsuitable.

Attempts to model the stress-flow behaviour of fractured rock, both those based on experimentally observed behaviour and those based on fundamental rock mechanics, have only found limited application or require simplifying assumptions with respect to fracture roughness. The changes in contact area and void space imposed by two rough surfaces being pressed together, and the corresponding effects on fluid movement within the fracture plane, have proven to be difficult parameters to measure. Another difficulty has been the observation of different scales of roughness and trying to determine what scale is important for fluid flow considerations.

Fracture surface roughness is without a doubt a key constitutive parameter in the stress-flow behaviour of fractured rock since it controls the overall structure of the fracture plane and hence the movement of fluids through the fracture. Roughness parameters alone do not describe the effect that surface roughness has on the shape and distribution of openings within the fracture plane under changing stresses. If none of the existing models satisfactorily reflect the role of fracture roughness, then it is apparent that direct measurements of roughness, contact area and void space of natural fractures under a range of stresses are necessary to define the basic input data needed to develop a suitable stress-flow model.

1.2 Objectives and Scope

This thesis evaluates the relevance and general applicability of several existing stress - flow models for fractured rock. Specifically, it examines the Gangi (1978) "bed of nails" model, the Walsh (1981) normal closure - conductivity model, the Tsang and Witherspoon (1981) void/asperity model, the Swan (1983) normal closure - conductivity model, and the Barton-Bandis (Barton et al., 1985) empirical model. Particular emphasis is given to the treatment of fracture roughness having identified it as a key element of stress - flow behaviour. Evaluation of these models requires accurate measurements of surface roughness, contact area and void space for input.

As part of this study, normal stress - fracture flow tests were conducted on a natural granite fracture under controlled laboratory conditions. These were followed by injection of an epoxy resin into the fracture plane at a specified normal stress and flow rate. The stress - flow test provided data on the hydromechanical behaviour of the fracture while the resin injection experiment enabled measurement of roughness and related features of the fracture plane through the use of digitized cross-sectional profiles.

The work presented here follows and expands upon other similar experiments on granite fractures using the resin injection technique developed at Memorial University (Gale, 1987). It is hoped that these types of experiments will provide the necessary database required to evaluate existing fracture flow models or provide the basis for which to develop a new constitutive model.

1.3 Background and Previous Work

Initial studies on flow through fractures, such as the work by Lomize (1951), Baker (1955), Huitt (1956), Romm (1966) and Louis (1969), were based upon the assumption that a fracture could be represented by two smooth parallel plates separated by some uniform opening, $2b$. This parallel plate model allows the derivation of an expression (Lomize, 1951) relating fracture hydraulic conductivity, K_f , to fracture opening or aperture such that,

$$K_f = \frac{\rho g}{12\mu} (2b)^2 \quad (1-1)$$

where ρ is the fluid density, g is the gravitational acceleration and μ is the dynamic viscosity of the fluid.

Substituting equation (1-1) into Darcy's law, Witherspoon et al. (1980) show that flow rate is related to the cube of the fracture aperture by the expression

$$\frac{Q}{\Delta H} = C (2b)^3 \quad (1-2)$$

where $Q/\Delta H$ is the fracture flow rate per unit head and C is a constant incorporating the geometry of the flow system and the properties of the fluid. Equation (1-2) is also known as the cubic law. For radial flow through a cylindrical core sample,

$$\frac{Q}{\Delta H} = \frac{2\pi}{\ln(r/r_w)} \cdot \frac{\rho g}{12\mu} (2b)^3 \quad (1-3)$$

with r_e and r_w being the outer sample radius and inner borehole radius respectively.

Through the use of the relative roughness concept, in which the roughness of the fracture wall is compared to the size of the fracture opening, the work on smooth surfaces was extended to rough surfaces resulting in a series of empirical flow laws covering the range of laminar to turbulent flow. More detailed discussions of these developments are given by Rissler (1978), Pearce and Murphy (1979) and Gale (1985). Assuming laminar flow predominates in rough fractures, the cubic law (equation 1-2) can then be modified to include roughness effects (Witherspoon et al., 1980) such that,

$$\frac{Q}{\Delta H} = \frac{C}{f} (2b)^3 \quad (1-4)$$

where f is a factor that accounts for deviations from ideal, smooth conditions. Witherspoon et al. (1980) determined f using a least squares fit to their experimental data points. From a hydraulic standpoint, f is a function of the relative roughness and takes the following form:

$$f = 1 + A(k/D_b)^{1.5} \quad (1-5)$$

Following the definition of Lomize (1951), relative roughness, k/D_b , is the absolute height of asperities divided by the fracture aperture, $2b$, and $A = 17$. According to

Louis (1969), k/D_h is defined as the mean height of asperities divided by the hydraulic diameter which is twice the fracture aperture and $A = 8.8$.

Most of these studies have dealt with two smooth or two uniformly rough artificial surfaces not in contact with each other. When it comes to natural fractures under stress, both sides of the fracture are in contact and the non-uniform roughness imparts a tortuous nature to fluid flow. Under these conditions, the friction factor - Reynolds number approach to describing flow behaviour breaks down. Experimental results by Sharp (1970) using a natural granite fracture under self weight conditions ($k/D_h = 0.5$) did not show agreement with the parallel plate model. This was attributed to the complex flow behaviour imposed by the irregular geometry of the fracture surface. Maini (1971) was able to visually show the diffuse, three-dimensional nature of flow between contacting rough surfaces using dye tests in transparent replicas of natural fractures. Both came to the conclusion (Sharp and Maini, 1972) that it would be impossible to derive general flow laws to account for the influence of detailed geometrical effects of natural fractures. Pearce and Murphy (1979) also suggested that because of the complexity of trying to specify a natural fracture flow surface, general flow laws describing fracture flow would probably never be developed.

The problems encountered with trying to develop general flow laws for rough fractures in contact has necessitated the need for in-situ and laboratory studies using natural and artificial fractures in an attempt to isolate the fundamental factors that

control stress-flow behaviour. Given the sensitivity of fracture flow rates to fracture aperture, many of these studies have examined the effects of stress and hence aperture changes on fracture permeability. Gale (1975), Jones (1975), Iwai (1976), Pratt et al. (1977), Nelson and Handin (1977), Kranz et al. (1979), Voegele et al. (1981), Engelder and Scholz (1981), Gale (1982), Gale (1984), Raven and Gale (1985), Elliott et al. (1985), Pyrak-Nolte et al. (1987), Gale (1987) and Gentier (1990b) have all investigated experimentally the stress-flow behaviour of natural and artificial fractures in many different rock types.

Empirical relationships between fracture permeability and effective stress are given by Jones (1975), Nelson and Handin (1977), Kranz et al. (1979) and Gale (1982). Several workers have addressed the applicability of the cubic law to describing fluid flow in fractures but with the exception of Iwai (1976) and Witherspoon et al. (1980) have generally found that it does not apply, especially at high stresses. Neuzil and Tracy (1981), Engelder and Scholz (1981), Sato et al. (1984) and Elliott et al. (1985) have proposed modified parallel plate models to try and make the theory more generally applicable to rough fractures.

One of the more useful empirical models developed so far is the coupled stress-deformation-conductivity model described by Barton and Bakhtar (1983) and Barton et al. (1985). Developed from many years of research on fracture behaviour and literally hundreds of tests on many different rock types, the model encompasses most of the fundamental processes of fracture behaviour. All that is needed to

define the required input for the model are a few simple index tests and an estimate of the initial fracture aperture. The differences between the real aperture and the theoretical smooth plate aperture are attributed to asperity contact, tortuous flow and surface roughness and are quantified in the model.

Theoretical treatment of the stress-closure-flow behaviour of fractures has involved the use of various asperity and void models that incorporate elastic contact behaviour of surface asperities and deformation behaviour of the void spaces around them. One of the more commonly used asperity models assumes that a rough surface consists of uniformly distributed, spherically-shaped asperities of equal radii and varying heights given by some statistical distribution function. Using this model, Greenwood and Williamson (1966) applied Hertzian theory for elastic contact of spheres to define the deformation of a rough metal surface being pressed against a flat plate as a function of the elastic properties of the material and the asperity height distribution. The theory was extended by Greenwood and Tripp (1971) to include the case of two rough surfaces in contact. Walsh and Grosenbaugh (1979) combined compressibility theory for rock fractures with the Greenwood and Williamson model. Assuming an exponential distribution of asperity heights, they derived a linear relationship between fracture stiffness and applied stress for mismatched fracture surfaces. The same experimentally-derived relationship was proposed by Goodman (1976).

Walsh (1981) showed that the Walsh and Grosenbaugh model could be used for fluid flow considerations since it included the effects of changes in both aperture and contact area. Using a heat flow analogy, he showed that the cube-root of flow rate should vary linearly with the logarithm of effective stress. Experimental results for artificial fractures tested by other workers showed good agreement with his theoretical relationship. Swan (1981) found that while the Walsh and Grosenbaugh theory modelled the fracture closure process it only provided a qualitative approximation of the stiffness behaviour of real fractures. Rather than using an assumed asperity height distribution, he showed that the use of actual asperity height data measured from roughness profiles led to a much better prediction of the experimental results. The concept was extended (Swan, 1983) to include changes in contact area and hydraulic conductivity as simple functions of normal stress and initial aperture. A more general contact theory for both mated and unmated fractures was presented by Brown (1984) based upon an extension of the Greenwood and Williamson asperity model. His measurements of surface roughness enabled him to compare the theory with experimental test results and demonstrate that fracture closure depends strongly on the roughness statistics of the contacting surfaces. Recent theoretical analysis of the permeability of rough fractures by Zimmerman et al. (1991) has shown how hydraulic aperture depends on the statistics of the aperture distribution.

Another asperity model was introduced by Gangi (1978) in which the asperities of a fracture surface were assumed to be pencil-shaped rods of various heights and diameters. The variation of the fracture aperture, and hence fracture permeability, with applied pressure was controlled by the elastic deformation of an assumed distribution of rod heights. Tsang and Witherspoon (1981) found that Gangi's model needed an unrealistically low contact area ratio or low Young's modulus for the asperities to give quantitative agreement with experimental data. These limitations led them to develop a physical model for fracture - flow behaviour which utilizes a void model to describe the deformation behaviour of the fracture and an asperity model to describe the hydraulic behaviour. Fracture closure was the result of deformation of the series of voids making up the fracture. The asperity model enabled the roughness of the fracture to be characterized which led to a statistical average of the variable aperture for fluid flow considerations. Hopkins et al. (1987) also describe a void - asperity model for the mechanical response of a fracture to applied stress which takes into account the deformation of both the asperities in contact and the surrounding void spaces. Their model predicts changes in aperture geometry that are not included in other asperity models and highlights the significant effects of the size, height distribution and spatial orientation of asperities.

The inconsistencies in experimental results and the limitations of theoretical models have proven that simplifying assumptions about fracture roughness are not

adequate for describing the stress-flow behaviour of fractured rock. Despite the recognition of the important role of surface roughness in controlling mechanical and hydraulic behaviour, very few workers have actually measured the roughness of the fractures they were testing. Of the studies mentioned thus far, only Sato et al. (1984), Swan (1981, 1983) and Brown (1984) include roughness measurements in their work.

The role of surface roughness in controlling the shearing behaviour of fractures has been studied for many years including the work of Patton (1966), Rengers (1970) and Barton (1971, 1973). Rengers (1970) was one of the first to actually measure roughness profiles for natural fracture surfaces. Since then there have been a number of different devices and techniques described in the literature for obtaining fracture roughness profiles. These include contour gauges (Stimpson, 1982; Jackson et al., 1985), mechanical profilometers (Swan, 1981; Brown, 1984; Sun, 1985; Voss et al., 1986; Hutson and Dowding, 1987) and digitized sectional photographs (Tse and Cruden, 1979; Dight and Chiu, 1981; Sato et al., 1984; Gale, 1987).

Once the roughness profile has been attained the problem becomes one of determining what scale of roughness needs to be measured and how to describe or characterize it. Most workers have recognized that there is more than one scale of roughness that may exist for fracture surfaces. It has been variously described as first-order irregularities vs. second-order irregularities (Patton, 1966), waviness vs.

roughness (Piteau, 1971), unevenness vs. roughness (Fecker, 1978), waviness vs. unevenness (ISRM, 1978) and large scale undulation vs. small scale roughness (Tsang and Witherspoon, 1982). The use of descriptive terms however only gives a qualitative characterization of roughness and for this reason many workers have opted to use statistical analysis of roughness profiles to quantify surface roughness. Profile statistics typically involve analysis of the heights of asperities, their spatial distribution and the angles they make with the mean plane of the surface. Many of these methods have their origin in the field of tribology where they have received detailed consideration (Thomas, 1982). Examples of where some of these methods have been used for fracture surfaces in rock include Wu and Ali (1978), Krahn and Morgenstern (1979), Tse and Cruden (1979), Dight and Chiu (1981), Westerman et al. (1982), Herdocia (1985), Lam and Johnston (1985), Reeves (1985) and Gentier (1990a).

Several workers have suggested that there may be a sample size effect on surface roughness (Barton and Bandis, 1982; Brown, 1984; Raven and Gale, 1985). One of the drawbacks of using profile statistics to characterize roughness is that if the sample length changes the statistical properties also change. An alternative approach to characterizing surface roughness that avoids this scaling problem involves the use of fractal geometry (Mandelbrot, 1977). The fractal concept is based on the idea that random, irregular surfaces display statistical self-similarity at all scales of magnification. The roughness of such surfaces at different scales of

measurement is specified by its fractal dimension which defines the rate at which roughness changes with sample size. Examples of the use of the fractal model to describe natural rock surfaces include Brown (1984), Carr and Warriner (1987), Turk et al. (1987), Lee et al. (1990) and Sakellariou et al. (1991). The fractal nature of fracture apertures and flow paths has also been demonstrated (Nolte et al., 1987; Wang et al., 1988; Wong et al., 1989). Brown (1987) has used simulated fractal surfaces to study the effects of surface roughness on fluid flow in rock fractures.

It has become apparent that mechanical and hydraulic experiments with rock fractures must be accompanied by measurements of roughness, contact area and pore space in order to understand and model stress-flow behaviour. This means that both sides of the fracture must be considered and the measurements must be made under various conditions of stress. This has proven to be a difficult task. Recent attempts at solving this problem include the work of Gale (1987), Pyrak-Nolte et al. (1987) and Gentier (1990a, 1990b). Gale (1987) describes a resin impregnation technique for measuring surface roughness, contact area and pore structure of natural fractures under known flow and stress conditions. An epoxy resin was injected into the fracture, the resin-filled fracture was sectioned and the resulting cross-sectional profiles were digitized to allow a direct measure of the surface roughness and related features of the fracture plane. Pyrak-Nolte et al. (1987) and Gentier (1990a, 1990b) describe a casting technique in which molten metal and resin, respectively, were injected into the fracture under various stress conditions. Image analysis of the

resulting casts was used to provide quantitative data on the void space geometry and contact area. Using this data, they were able to qualitatively link measured mechanical and hydraulic behaviour to the geometry of the fracture plane. Studies of these types are needed to provide the quantitative measurements of surface roughness effects on fracture-flow behaviour.

Chapter 2 EXPERIMENTAL DESIGN AND PROCEDURES

Stress-flow tests were carried out on a granite core sample measuring roughly 20 cm in diameter by 42 cm in length and containing a natural fracture perpendicular to the core axis. The sample was incrementally loaded and flow tested at normal compressive stresses up to a maximum of 30 MPa. It was similarly unloaded and reloaded to a final normal stress of 1 MPa at which time the fracture was injected with a room temperature curing epoxy resin. The stress-flow tests provided measurements of fracture closure and fracture flow rates while the resin injection enabled measurements of fracture roughness and aperture at known stress and fluid flow conditions.

2.1 Sample Preparation

The sample used in this investigation was collected from a fresh, natural fracture plane at the "Charcoal Grey" granite quarry near St. Cloud, Minnesota using a rock bolt-overcoring technique to provide a relatively undisturbed sample of a natural fracture. Details of the original collection and preparation procedures for this sample are given in Gale and Raven (1980) and will only be summarized here. A rock bolt was installed in a small borehole drilled across the fracture plane and then overcored with a 20 cm diameter core barrel. At the laboratory, anchor posts were mounted on the outside of the sample to keep the fracture together so that the rock bolt could be removed and the ends prepared for uniaxial testing. A water inlet

plate was attached to the bottom of the sample to allow injection of water through the central borehole and out the fracture plane, i.e. radially-divergent flow. A small diameter hole was drilled from the outside of the sample to the end of the central borehole to act as a pressure port for bleeding air from the fracture plane and measuring fluid pressures during flow testing.

To measure rock and fracture deformation, three Schaevitz linear variable differential transducers (LVDT's) were mounted across the fracture at 120° spacings around the outside of the sample. A fourth LVDT was mounted above the fracture plane to measure the deformation of the rock only. The LVDT's were capable of measuring deformations of less than 1 μm . To measure the variation in strain between the top of the sample and the fracture plane, Bean strain gauges were attached to the upper half of the sample in a vertical string and in vertical-horizontal pairs near the fracture at each LVDT (see Figure A.1). The sample was placed between two aluminum loading plates and lowered into a Plexiglas tank filled with water that maintained a constant water level above the fracture plane. A schematic of the sample after final preparation and instrumentation is shown in Figure 2.1.

2.2 Stress-Flow Tests

The equipment for flow testing the fracture consisted of four main components as shown in Figure 2.2: (1) the loading frame (2) the flow system (3) the temperature control system and (4) the data acquisition system. A 2.67 MN Material Testing

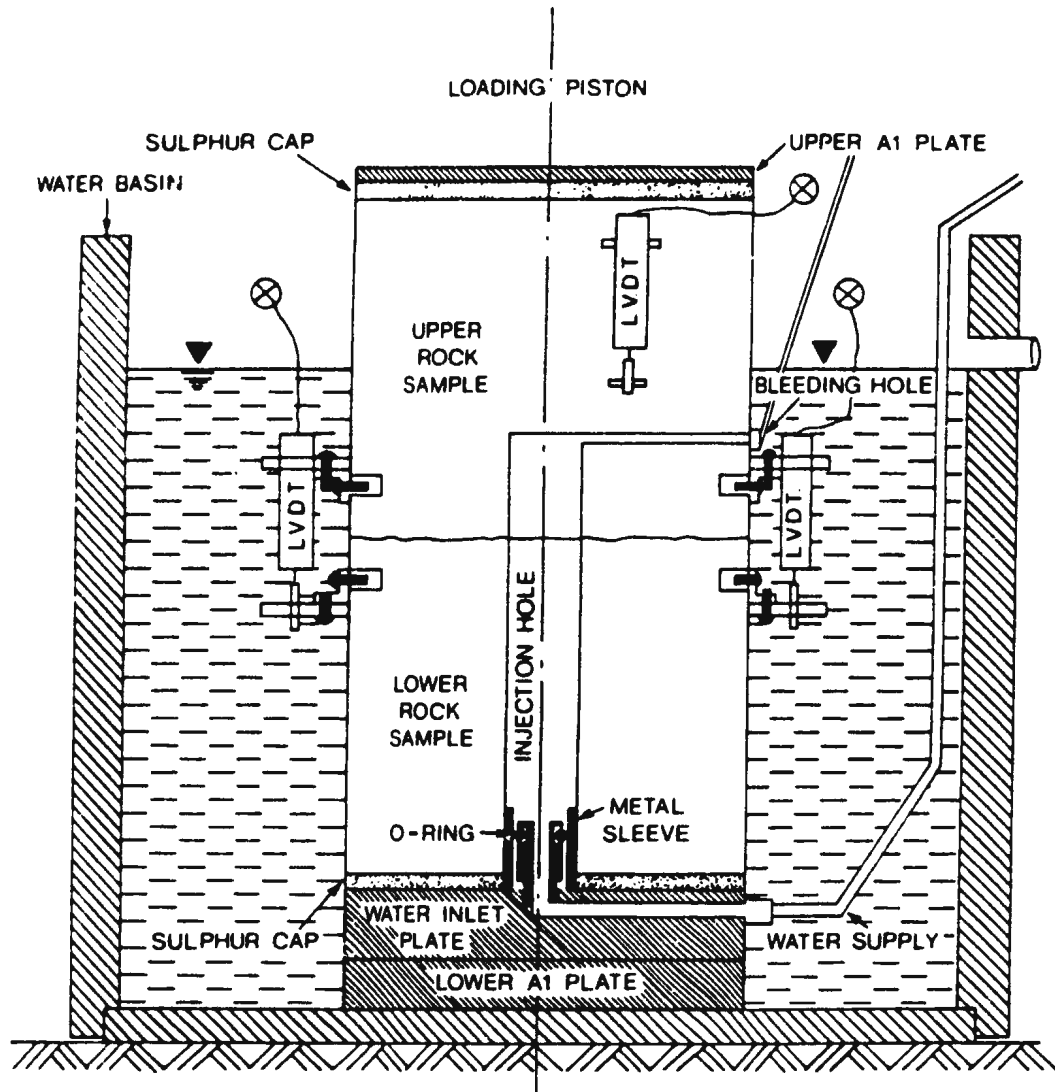


Figure 2.1 Schematic of fully instrumented sample for stress-flow testing (after Gale, 1982).

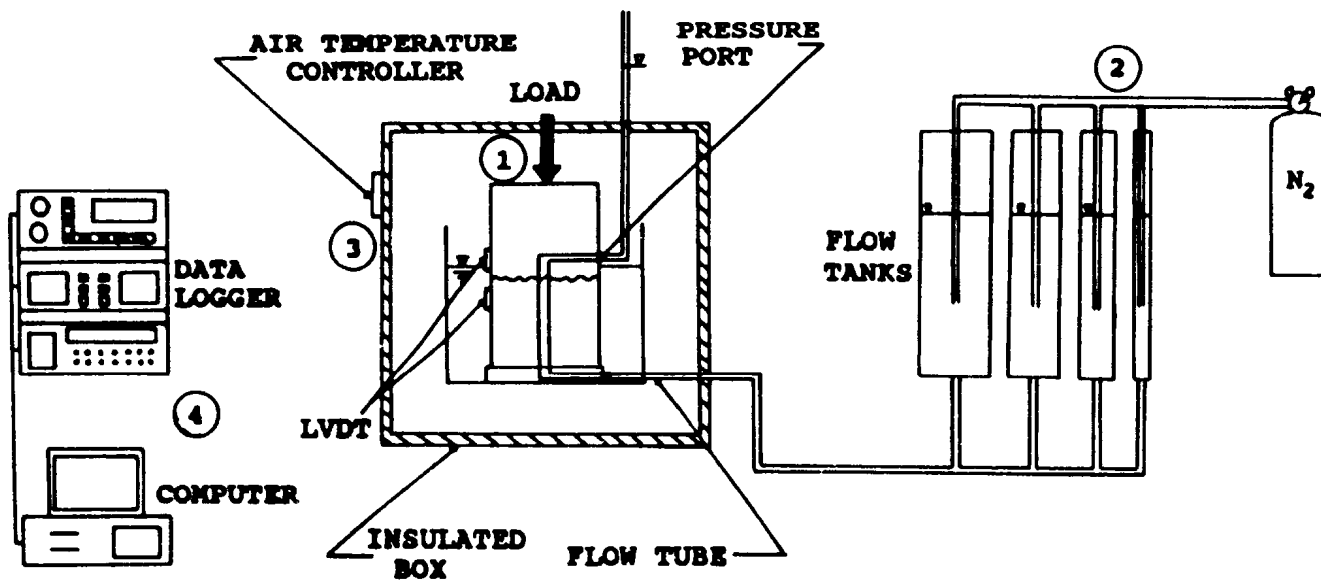


Figure 2.2 Schematic of stress-flow testing components: (1) loading frame (2) flow system (3) temperature control system and (4) data acquisition system.

Services (MTS) closed-loop, servo-controlled testing machine was used to apply the axial loads. Three 0.89 MN capacity BLH load cells built into the upper loading platen measured the applied loads. The samples were tested under load control feedback conditions. A steel plate was placed between the top of the sample and the upper loading platen to ensure uniform load distribution over the sample. Before testing the sample, the MTS hydraulic pump was cycled for several hours to remove any air in the system and the load cells were calibrated. A hollow steel cylinder was placed in the testing frame and loaded to properly seat the loading platens so that no eccentric loading was taking place and to ensure that the system was working properly.

The flow system consisted of a series of four positive displacement flow tanks connected to the water inlet plate. The cylindrical flow tanks were of four different diameters and arranged so that flow could be switched to either tank. The flow rates were determined by measuring the change in water level in a tank over a given time period. By switching to a tank of different diameter, flow rates could be measured over several orders of magnitude. Compressed nitrogen was used to pressurize the tanks and provide a constant fluid pressure during the injection tests. The applied pressures did not exceed 5 psi (0.035 MPa). A manometer tube connected to the pressure port allowed measurements of hydraulic head to be made. Distilled water was used throughout the test.

To avoid thermal effects on the measuring devices and testing equipment due to temperature fluctuations within the testing environment, a temperature control system was devised using air as the controlling medium. This consisted of a 0.77 m x 0.61 m x 0.48 m box frame covered with 2 inch (5 cm) thick styrofoam and attached to the testing frame so as to enclose the sample and Plexiglas water tank. An RFL Industries Model 70A Air Temperature Controller (range 25-90°C) was used with two heater bars built into the front panel to control the air temperature inside the box. A small fan built into the front panel circulated the air inside the box. Two thermocouples were installed inside the insulated box, one to monitor the air temperature and one to measure the temperature of the water surrounding the sample. A dial thermometer was also inserted into the insulated box to provide a rapid visual check of the inside air temperature. The system was able to maintain a constant temperature to within ± 1 °C.

The basic data acquisition system was an HP - 3497A data acquisition/control unit with 60 multiplexer channels for reading output signals from LVDT's, strain gauges, load cells, thermocouples, thermistors, etc. The system had a sensitivity of 1 microvolt and provided a digital output (VDC) signal for control purposes. The data acquisition unit was interfaced with a Tandy 1200-HD personal computer with 10 Mbytes of disk storage. A software program written specifically for these tests allowed manual or automatic scanning of all data channels with continuous display and/or print out of the data.

Having undergone three previous loading and unloading cycles, described by Gale and Raven (1980) and Raven and Gale (1985), the sample was subjected to a final complete loading-unloading cycle to remove as much hysteresis as possible and obtain reproducible behaviour. First the sample was placed in the loading frame and a small seating load of 0.02 MPa was applied. The anchor posts were removed from the sample and the LVDT's, strain gauge leads and flow lines were connected. The water tank was filled to a level just above the fracture and the flow lines and fracture were flushed with carbon dioxide and deaired water to remove any air pockets and thoroughly saturate the sample. The temperature control system was put in place and the temperature adjusted to about five degrees above room temperature. In order for the temperature of the rock, equipment mass, water and air inside the insulated box to equilibrate, the temperature control unit was allowed to run overnight prior to testing.

The normal load on the sample was increased in steps up to a maximum stress of 30 MPa and then unloaded using the following nominal load path: 0.2, 0.6, 1.0, 3.0, 7.0, 10.0, 20.0, 30.0, 20.0, 10.0, 3.0, 1.0, 0.2 MPa. At each normal stress level, steady-state radial flow tests were conducted from the central borehole. Computerized data scans recorded measurements of applied load, fracture and rock closure, fluid pressure, strain gauge readings and temperature at 10 to 15 minute intervals or "runs". Flow rates were calculated at the end of each run. The occurrence of stable flow rates for three consecutive runs constituted a complete

testing sequence for a given stress level. A similar procedure was followed for unloading the sample. It took several hours for the flow rates to stabilize at each stress level, thus flow testing for the full loading-unloading cycle took over 72 hours to complete.

2.3 Resin Injection Technique

Prior to the resin injection experiment, the sample was loaded again in 0.2 MPa increments to an injection stress level of 1 MPa with radial flow tests conducted at each step as before. After the final flow test and with the injection stress held constant, the water was drained from the fracture and the sample allowed to dry overnight inside the temperature control unit. As a further measure, carbon dioxide was flushed through the system to remove any remaining moisture. The fracture plane was isolated with an aluminum bracket collared around the circumference of the sample. Strips of soft impression rubber were placed between the sample and the aluminum bracket above and below the fracture to create a seal with the outside edge of the fracture. The bracket contained three ports to allow the resin to exit the fracture plane. A pressurized holding cylinder for the resin and a vacuum pump were connected to the system as shown in Figure 2.3.

To inject the resin, a negative pressure of 20 - 30 psi was created using the vacuum pump connected to the borehole pressure port and the three ports in the aluminum bracket. A blue-coloured epoxy resin was then added to the holding

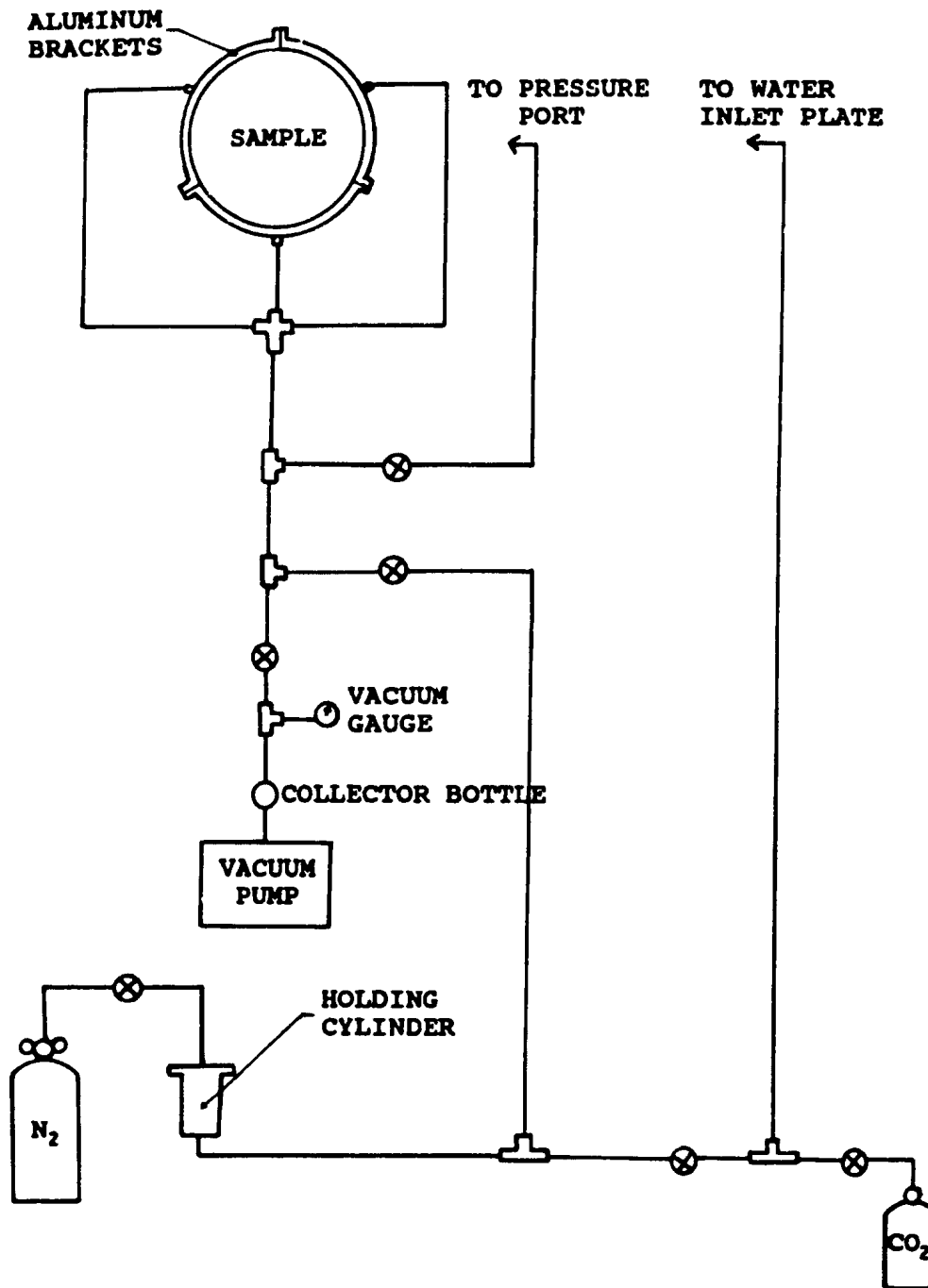


Figure 2.3 Schematic of the resin injection system.

cylinder connected to the water inlet plate at the base of the sample. The resin was drawn through the water inlet plate, up into the central borehole and into the fracture plane. The vacuum was held until the resin came out each of the three ports in the aluminum bracket confirming that the fracture plane was completely saturated with resin. The vacuum was then shut off and the resin allowed to cure overnight. The 1 MPa injection stress was maintained on the sample the whole time and load, fracture displacement, and air temperature were continuously monitored. Once the resin had completely hardened, the load was carefully removed. The resin injection cycle took about 3.5 days to complete.

2.4 Resin Analysis Method

After the resin in the fracture had fully cured, cross-sectional cuts were made through the fracture plane to create a series of resin-filled profiles of the fracture. The profiles were then photographed under a microscope so that they could be digitized and analyzed by computer. The process consisted of four steps: (1) cutting and grinding the fracture cross-sections (2) photographing the fracture profiles at an enlarged scale (3) constructing continuous fracture profiles from the photographs and (4) digitizing the photographic profiles using a computer and digitizing table.

The cross-sectional cuts were made through the fracture plane using a rock saw and the exposed surfaces were ground and polished using a K.O. Lee Surface Grinder. The sample was divided into four quadrants and successively cut back at

roughly 10 mm intervals in both the x and y directions to produce a total of forty eight fracture profiles. Each profile was clearly labelled indicating the top and bottom of the fracture and a 1:1 drawing of the fracture trace was made using mylar drafting film. The number and location of each profile is shown in Figure 2.4. Examples of 1:1 drawings of the fracture trace for several of the profiles are shown in Figure 2.5. The fracture profiles were each photographed at a 30:1 scale using a Wild Photomakroskop M400 photomicroscope. At this scale, approximately 5 mm of the fracture profile could be photographed at a time. Each fracture profile was then reconstructed from the photographs by carefully mounting the overlapping prints on a roll of paper to form a continuous photographic profile of the fracture.

The fracture profiles were digitized using a Mayline Futur-matic Digitizing Table connected to a computer complete with mouse and digital coordinate display. The mouse consisted of a small key pad and a window with a set of orthogonal cross-hairs for tracing the outline of the profile being digitized. The system was capable of measuring and recording x - y coordinates at intervals as small as 0.01 mm (10 μ m). The top and bottom fracture profiles were digitized separately. Points where the two surfaces contacted, or where a rock fragment bridged the gap between them, were flagged so that they could be analyzed individually. The digitized data was manipulated and statistically analyzed on a main frame computer using a series of FORTRAN, C and SPSSx programs.

SAMPLE 80-3

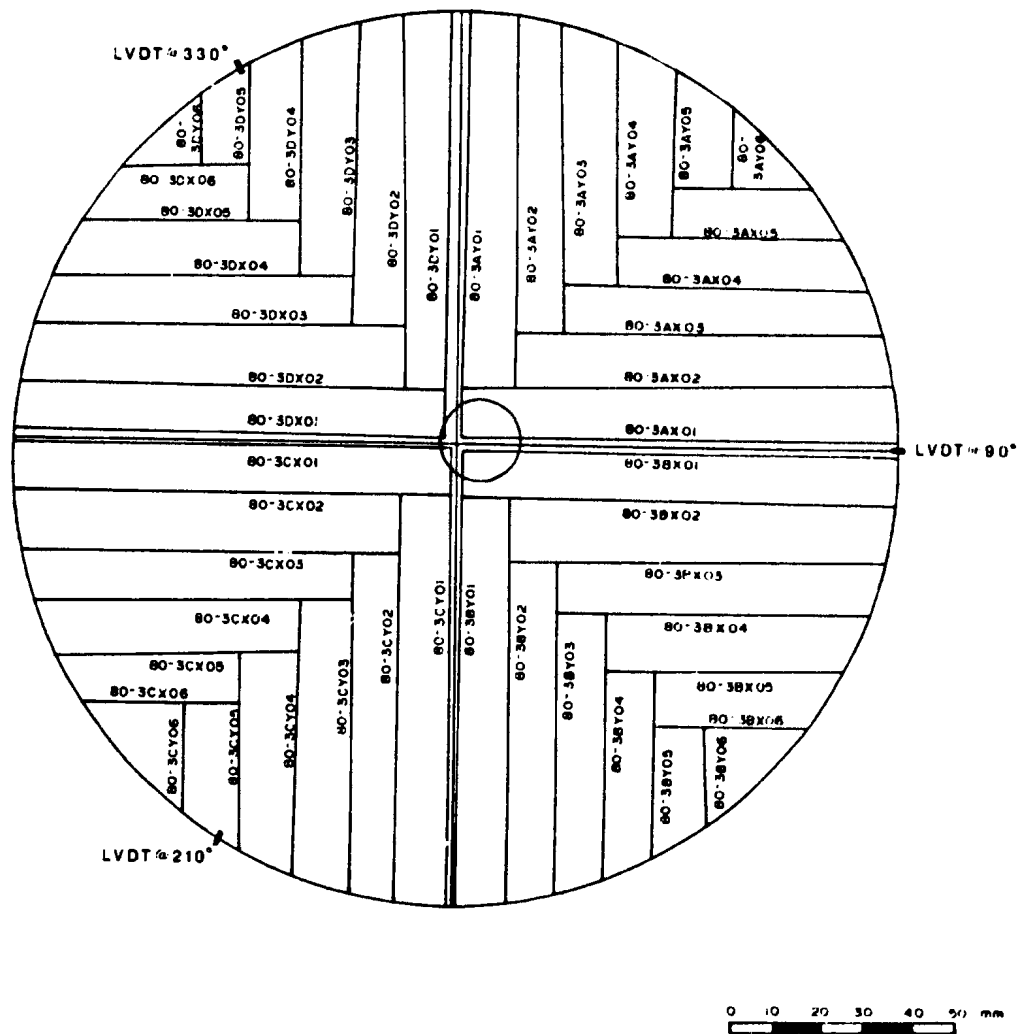


Figure 2.4 Plan drawing showing the number and location of fracture profiles obtained by cross-sectional cuts through the resin-filled fracture plane.

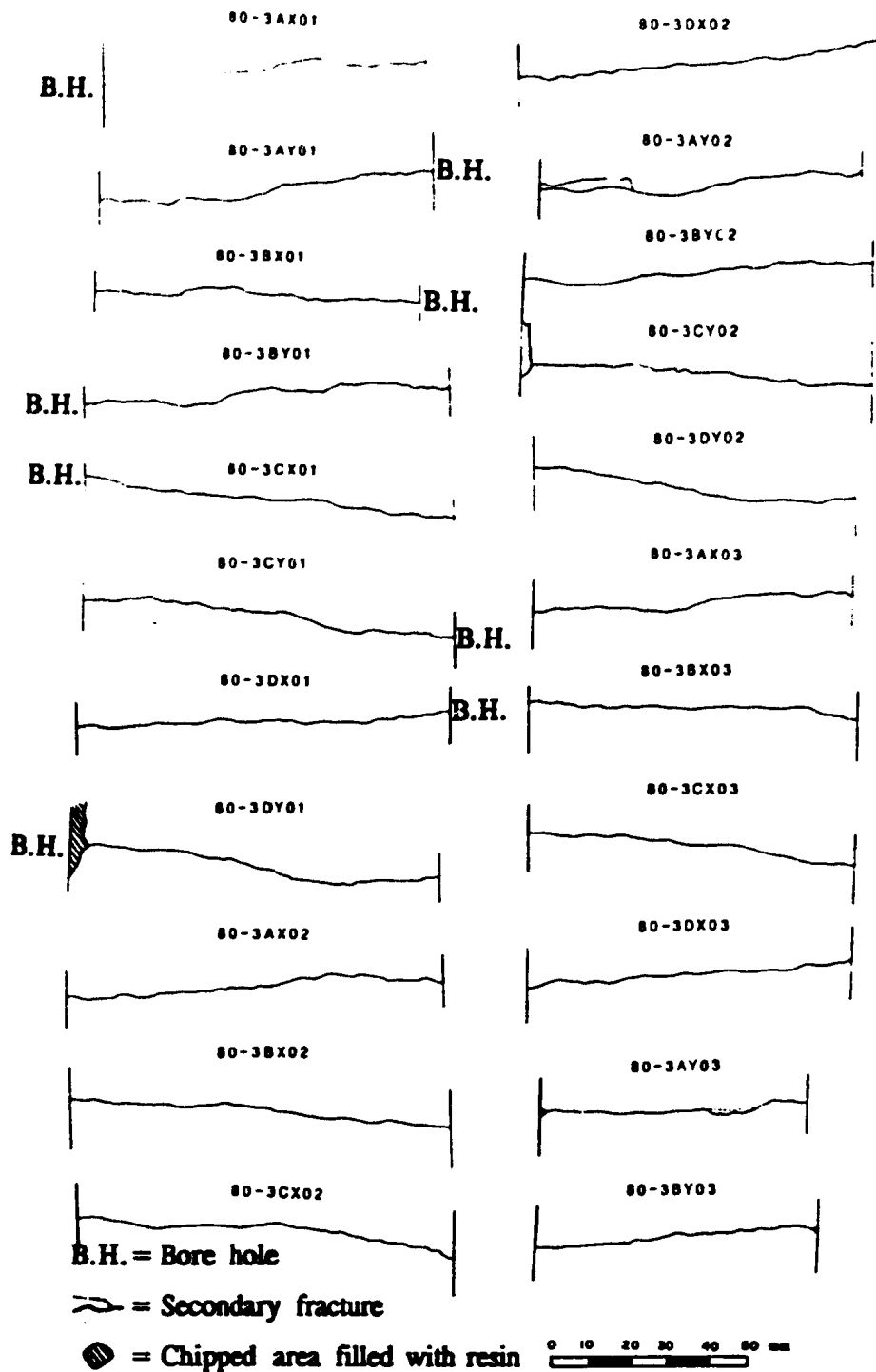


Figure 2.5 Examples of 1:1 line drawings of the fracture trace for selected profiles.

Chapter 3 EXPERIMENTAL RESULTS AND DATA ANALYSIS

3.1 Stress-Flow Results

Stress-flow tests were conducted on the fracture during a final loading-unloading cycle at normal stresses up to 30 MPa and also during the resin injection loading cycle. The purpose of these tests was to determine the mechanical and hydraulic behaviour of the fracture as a function of normal stress. The stress-flow tests during the resin injection cycle served to define the conditions under which the measurements of fracture roughness, contact area and aperture were to be made.

The mechanical behaviour of the fracture is summarized in Table 3.1 and Figure 3.1 which shows the normal stress - fracture closure curves for the three loading-unloading cycles described by Gale and Raven (1980) and for the final loading-unloading cycle and resin injection cycle carried out in these experiments. Fracture closure was determined by subtracting the rock deformation measured by the LVDT on the upper half of the sample (Figure 2.1) from the average combined deformation of the rock and the fracture measured by the three LVDT's straddling the fracture. The curves in Figure 3.1 exhibit the typical non-linear deformation behaviour of fractures with hysteresis between loading and unloading cycles and decreasing fracture closure with each successive loading-unloading cycle. The maximum fracture closure was about 200 μm for the first cycle decreasing to about 100 μm for the final cycle. The similarity of the resin injection loading curve to the unloading curve for the final cycle (see inset, Figure 3.1) indicates that most of the

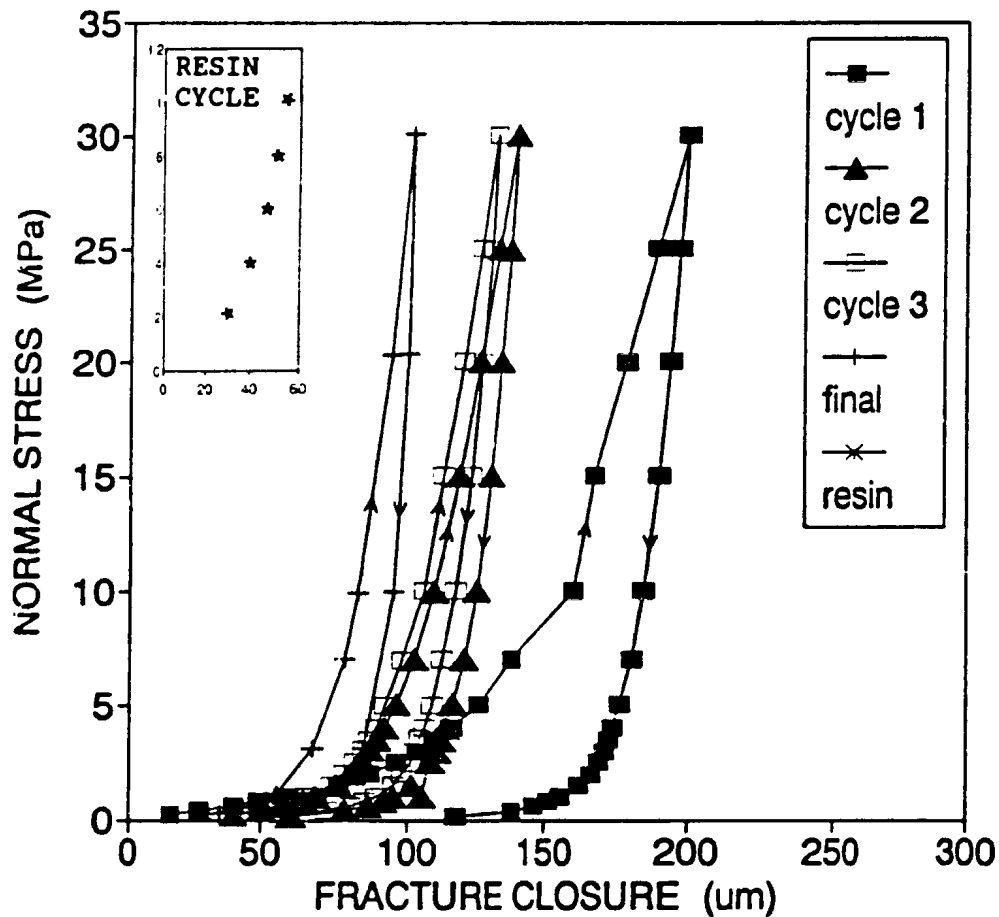


Figure 3.1 Fracture closure as a function of normal stress for the first, second, third, final and resin loading cycles (cycle 1, 2 and 3 data from Gale and Raven, 1980).

hysteresis in the sample had been removed and the fracture was approaching repeatable elastic behaviour.

The hydraulic behaviour of the fracture is shown in Figure 3.2 which is a semi-log plot of normalized flow rate versus normal stress for the three loading-unloading cycles of Gale and Raven (1980) and the final loading-unloading cycle and resin injection cycle conducted in the current experiments. These curves also exhibit strong non-linear behaviour with hysteresis between loading and unloading cycles and decreasing flow rate with each successive loading-unloading cycle. The amount of hysteresis and the reduction in flow rate decreased with each loading-unloading cycle, such that the resin injection curve matched the final unloading curve. The flow rate and fracture closure data are given in Table 3.1.

To determine the hydraulic conductivity of the fracture involves making the assumption that the cubic law can be used to calculate the hydraulic aperture. Using the method of Witherspoon et al. (1980), hydraulic apertures were calculated from the flow test results by assuming the cubic law to be valid at the maximum normal stress used in the tests. The effective hydraulic aperture, $2b$, therefore consists of an unknown residual aperture, $2b_{res}$ at the maximum normal stress and a measured aperture, $2b_m$ determined from the LVDT closure measurements, i.e.

$$2b = 2b_{res} + 2b_m \quad (3-1)$$

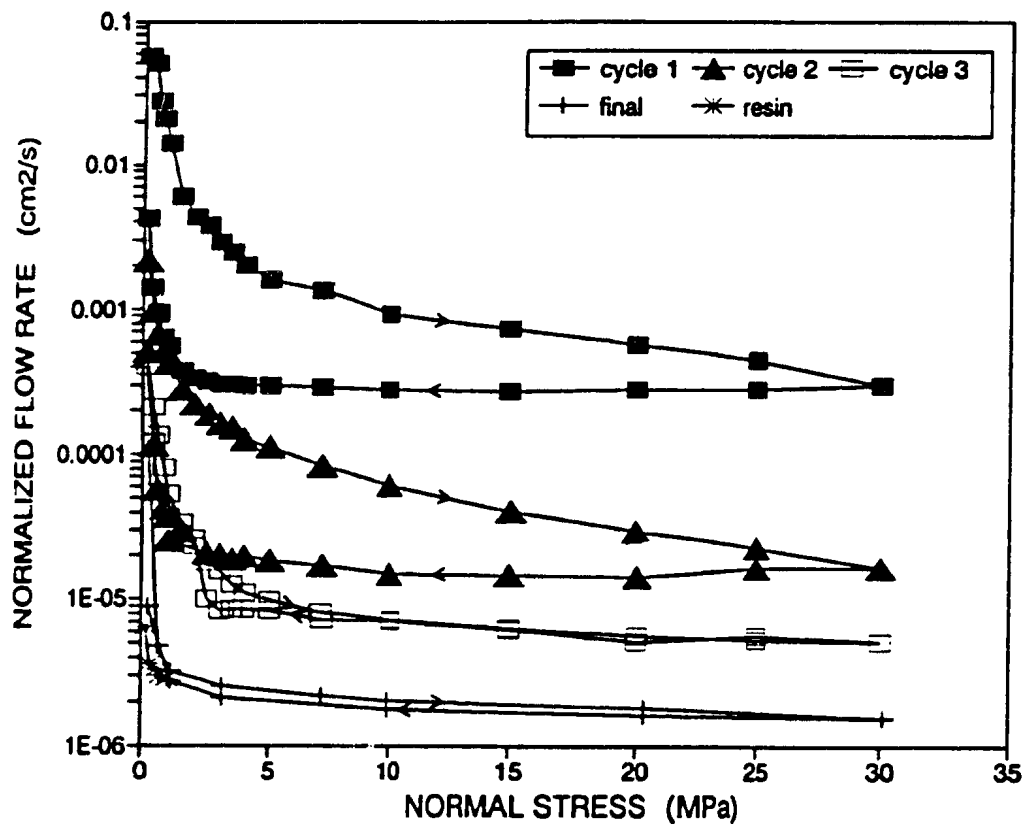


Figure 3.2 Normalized fracture flow rate as a function of normal stress for the first, second, third, final and resin loading cycles (cycle 1, 2 and 3 data from Gale and Raven, 1980).

Table 3.1 Stress-flow test results and computed hydraulic apertures for final loading - unloading cycle and resin injection cycle.

NORMAL STRESS σ_n (MPa)	HEAD ΔH (cm)	NORMALIZED FLOW RATE $Q/\Delta H$ (cm ² /s)	FRACTURE CLOSURE δ_f (μm)	SMOOTH APERTURE $2b_s$ (μm)	ROUGH APERTURE $2b_r$ (μm)
----- final cycle -----					
0.00			0.00	105.85	108.27
0.26	217.5	9.77E-5	35.70	70.15	72.57
0.66	255.5	4.82E-6	49.14	56.71	59.13
1.14	318.9	3.22E-6	55.61	50.24	52.66
3.10	410.6	2.54E-6	67.05	38.79	41.22
7.03	398.9	2.17E-6	77.99	27.85	30.28
9.91	389.7	2.04E-6	82.63	23.22	25.64
20.32	381.9	1.79E-6	94.49	11.36	13.78
30.09	373.9	1.54E-6	101.82	4.03*	6.45*
20.34	368.1	1.62E-6	100.37	5.48	7.90
9.95	361.5	1.78E-6	95.06	10.79	13.21
3.11	354.0	2.15E-6	84.45	21.40	23.82
1.13	315.8	2.77E-6	71.52	34.33	36.75
0.28	340.2	9.06E-6	47.66	58.15	60.61
----- resin cycle -----					
0.00			0.00	59.56	62.54
0.21	313.1	6.51E-6	30.04	29.52	32.50
0.40	309.1	3.61E-6	40.23	19.33	22.32
0.60	327.4	3.29E-6	46.85	12.71	15.69
0.80	317.4	2.99E-6	51.21	8.35	11.33
1.01	304.7	2.87E-6	54.61	4.95*	7.93*

* indicates residual apertures calculated at maximum stress using equations 1-2, 1-4 and 1-5; remaining apertures calculated using equation 3-1 (following method of Witherspoon et al., 1980).

Rearranging equation (1-2) and solving for $2b$ enables the hydraulic aperture to be calculated at the maximum normal stress. Once $2b_{max}$ is calculated, the hydraulic aperture at each normal stress level easily follows from equation (3-1). The cubic law assumes the fracture walls to be smooth and parallel. For rough fractures, a correction must be made to the cubic law to account for the roughness of the fracture surfaces. Following the approach of Louis (1969) and using the maximum relative roughness possible, i.e. of $k/D_h=0.5$ (contacting surfaces), the rough-walled aperture can be determined from equations (1-4) and (1-5). The smooth-walled aperture is just the special case where $k/D_h=0$. Smooth hydraulic apertures, $2b_s$, and rough hydraulic apertures, $2b_r$, calculated for the final loading-unloading cycle and the resin cycle are given in Table 3.1. The two apertures only differ by a factor of 1.6 at the maximum normal stress. It should be noted that the calculated apertures are sensitive to the stress level used to calculate the residual aperture. In Table 3.1, the residual aperture was calculated at 30 MPa for the final load cycle and at 1 MPa for the resin loading cycle. When comparing data from different cycles it is better to use the same reference stress where possible.

In Figure 3.3, the calculated rough hydraulic apertures have been plotted against normalized flow for all loading cycles. If the cubic law relationship between aperture and flow rate is valid, the data should plot on a straight line with a slope of one-third. The results for each cycle are nonlinear and show a marked deviation from the cubic law relation as indicated by the straight line in the diagram. The flow

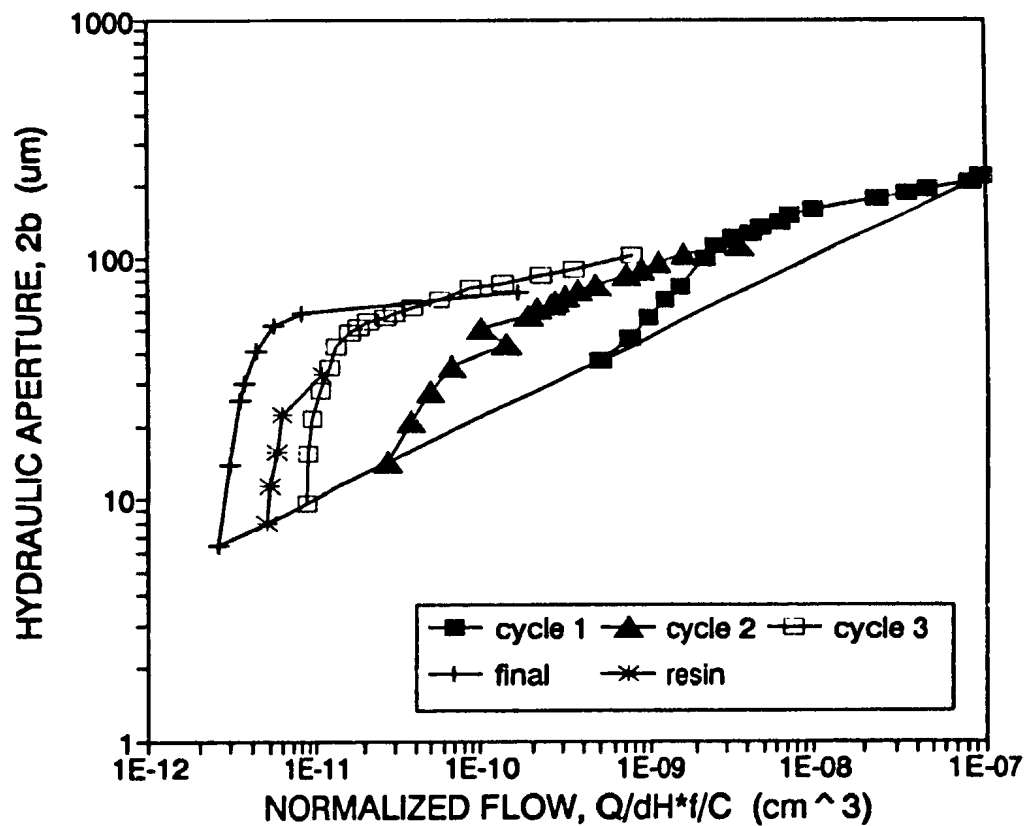


Figure 3.3 Computed hydraulic apertures plotted against normalized flow for the first, second, third, final and resin loading cycles (cycle 1, 2 and 3 data from Gale and Raven, 1980).

rate decreases at a much slower rate than does aperture as the normal stress is increased and this behaviour is more pronounced with increasing number of loading cycles. In other words, as the fracture continues to close under increasing stress, the flow rate tends towards some constant value that does not depend on fracture aperture alone. The results of these tests show that the parallel plate model does not apply to natural fracture surfaces that have undergone several loading-unloading cycles.

3.2 Characterization of a Rough Fracture

Impregnation of the fracture with epoxy resin enabled direct measurement of fracture surface roughness and the structure of the fracture plane. This was achieved through the analysis of fracture profiles generated from a series of cross-sections through the resin-filled fracture. The resin injection technique and method of analysis has been discussed in Chapter 2. Presented below are the results of the measurement and characterization of large- and small-scale fracture roughness, contact area, aperture and void space.

3.2.1 Large-scale roughness

One of the best ways to obtain quantitative measurements of surface roughness is through the use of fracture profiles. As part of this study, a total of forty eight profiles were produced from the resin-filled fracture to facilitate

measurement of the roughness and the relative position of both sides of the fracture under actual test conditions. The cross-sections were made in both the x- and y-directions to verify any possible anisotropic effects and give maximum coverage of the fracture plane. Examples of roughness profiles for two such cross-sections, one in the each of the x- and y-directions, are shown in Figure 3.4. Each of these profiles display a large-scale roughness with a superimposed small-scale roughness for both the top and bottom surfaces.

Large-scale roughness is a function of the overall shape of the profile, sometimes referred to as waviness, while small-scale roughness refers to the many tiny peaks and valleys that make up the profile giving it a jagged appearance. The waviness of these profiles is on the order of centimeters; the small-scale roughness is on the order of micrometers. Note that in order to bring out the small-scale roughness of the profile, the vertical scale in Figure 3.4 is double that of the horizontal scale and a small vertical separation has been added to distinguish between the top and bottom profiles, i.e the spacing between the top and bottom profiles in Figure 3.4 is not the real fracture opening.

Fracture roughness is commonly characterized in terms of an asperity height distribution. In this study, asperity heights were measured as the vertical distance between points on the profile and a reference line through the base of the profile. Referring to Figure 3.5, best-fit lines were determined for each of the top and bottom profiles using standard linear regression techniques. Reference lines were

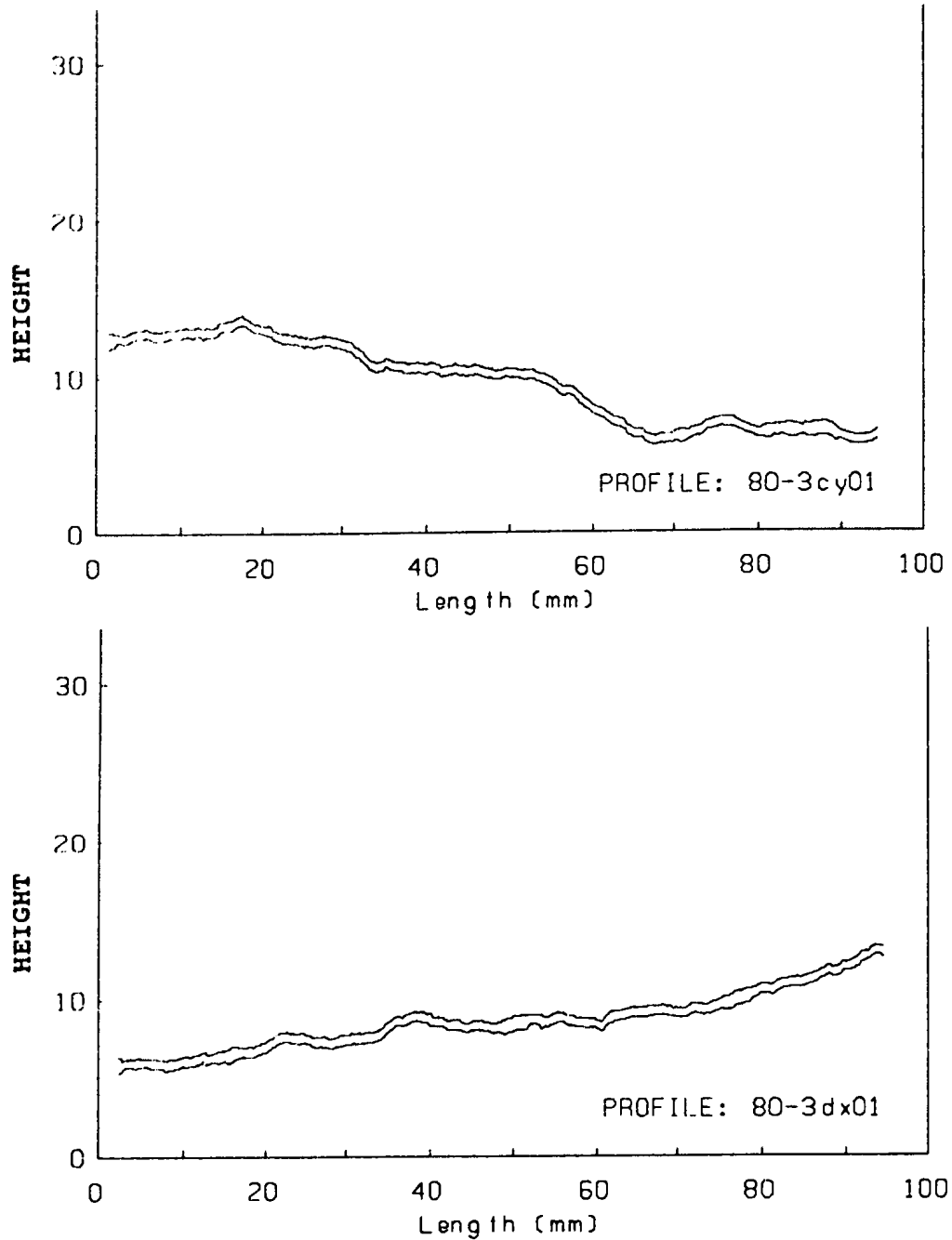


Figure 3.4 Roughness profiles for two selected cross-sections. The vertical scale is twice the horizontal scale and a small vertical separation has been added between the two surfaces.

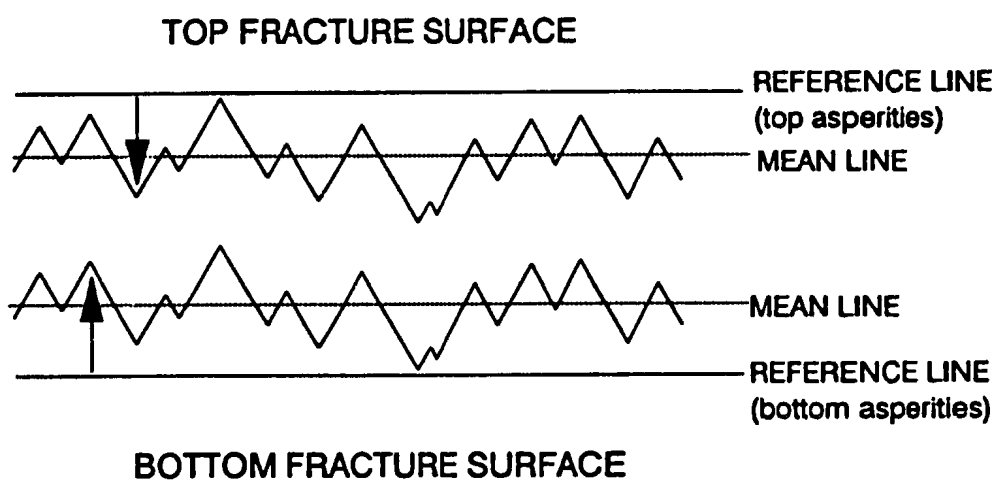


Figure 3.5 Schematic of the definition of asperity height used for determining asperity height distributions.

then drawn parallel to the best-fit lines, one passing through the highest point on the top profile and one passing through the lowest point on the bottom profile. The bottom asperity heights were measured upwards from the reference line while the top asperity heights were measured downward from the reference line. The resolution of the system allowed sampling intervals as small as 10 μm .

Frequency histograms of the asperity height distributions for the top and bottom surfaces of the two profiles in Figure 3.4 are given in Figure 3.6. The measured asperity heights include both large and small-scale roughness ranging from 0 to about 3 mm. The asperity height distributions reveal a noticeable difference in roughness characteristics between the top and bottom fracture surfaces. The distribution for the top surface of profile 80-3CY01 is skewed towards the left with a mean asperity height of about 1 mm while the distribution for the bottom surface is skewed towards the right with a mean asperity height of 2 mm. The two surfaces for profile 80-3DX01 show normally-distributed type distributions with distinct peaks in the 1 to 1.5 mm range. However, both sets of surfaces are not mirror images of each other as one might expect for well-mated fractures with identical roughness on both sides of the fracture.

The mean and standard deviation, also known as root mean square (RMS), of the asperity height distributions are good indicators of the average roughness of the fracture. Well-mated fractures should have similar average roughness parameters

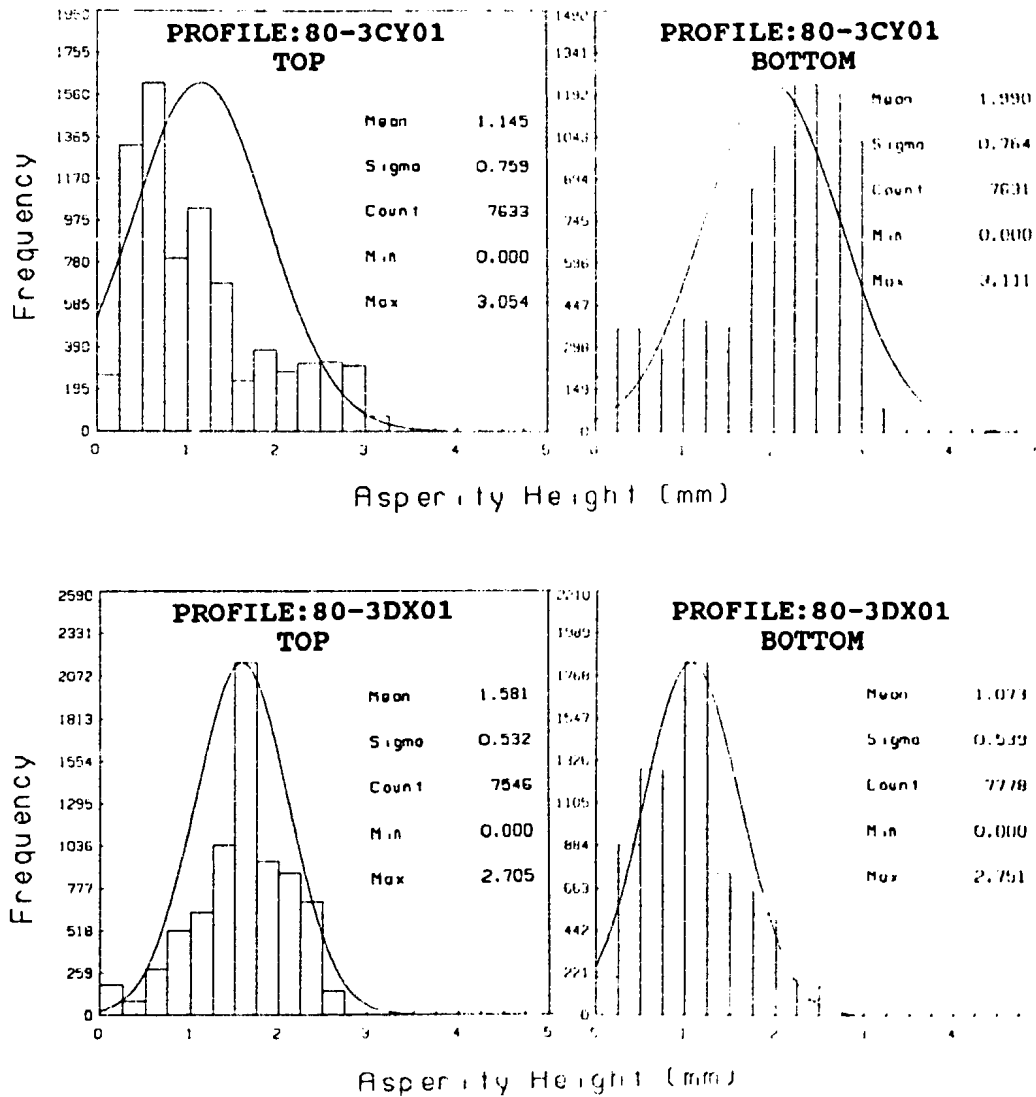


Figure 3.6 Frequency histograms of large-scale asperity heights for top and bottom surfaces of two selected profiles with superimposed normal distribution curves.

for both sides of the fracture. The standard deviations for the top and bottom surfaces of the above two profiles only differ by 5 to 7 μm yet there are very distinct differences between the asperity distributions. These discrepancies impart a variable aperture to the fracture which in turn controls the movement of fluids within the fracture plane. These results emphasize the importance of defining the roughness of both sides of the fracture and how the use of average roughness parameters can be misleading.

In an attempt to model the measured asperity height distributions, the histograms in Figure 3.6 have been fitted with a normal (or Gaussian) distribution curve using the same mean and standard deviation. Profile 80-3DX01 is closely approximated by a normal distribution whereas profile 80-3CY01 is not. However, as shown in the frequency histograms in Figure 3.7, if the natural logarithms of the measured asperity heights are taken a better fit is obtained with a normal curve indicating that a log-normal distribution may be a better approximation to the asperity height data. The combined results from measured asperity heights for all of the profiles are summarized in Table 3.2. Based on over 230,000 observations each, the mean asperity heights for the top and bottom surfaces were found to differ by only 0.1 mm with similar standard deviations. Despite these similarities, the differences in the individual histograms for both sides of the fracture indicate that the fracture is not completely mated. This mismatch gives rise to a variable fracture

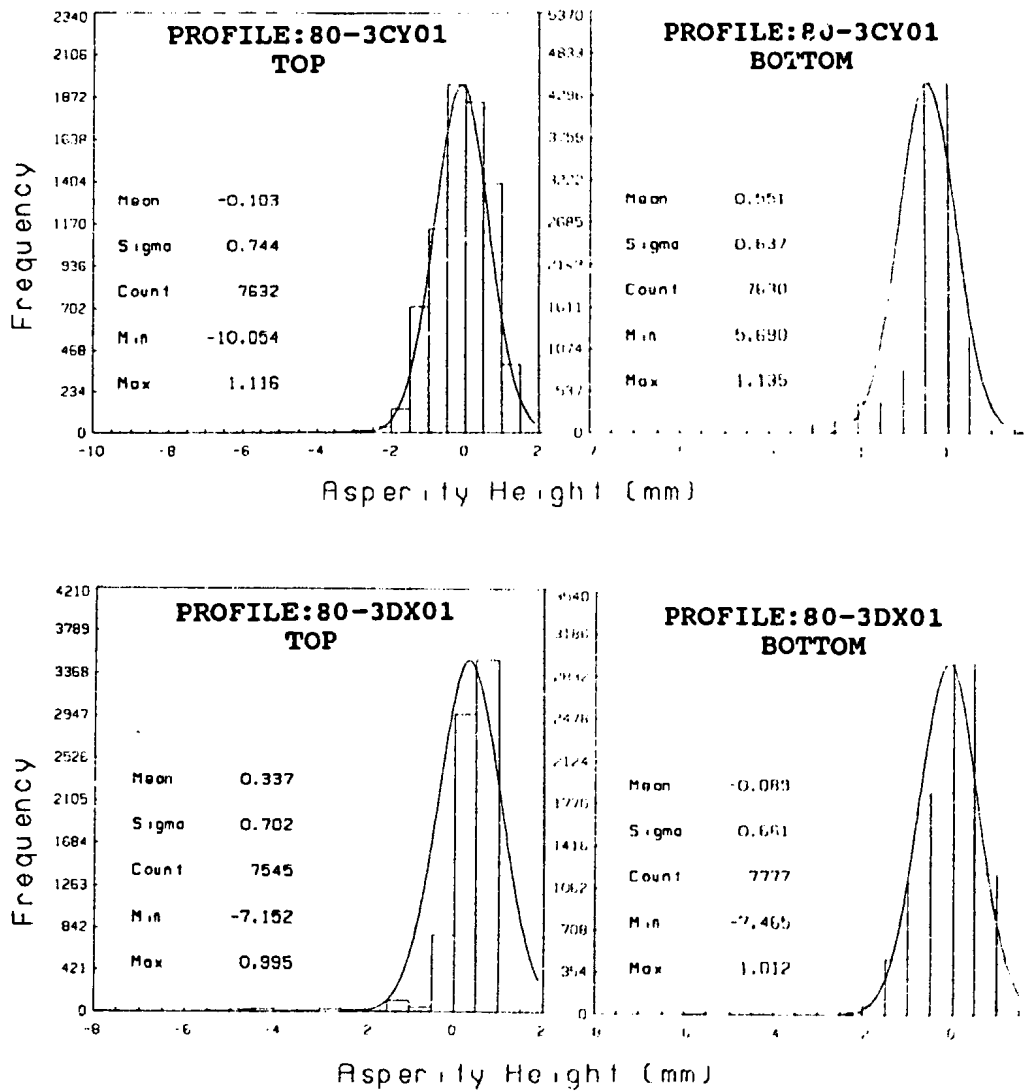


Figure 3.7 Frequency histograms of the natural logarithms of large-scale asperity heights for two selected profiles with superimposed log-normal distribution curves.

Table 3.2 Summary statistics on large-scale roughness measurements from all fracture profiles combined.

	TOP ASPERITY HEIGHTS	BOTTOM ASPERITY HEIGHTS
<u>MEASURED DISTRIBUTION</u>		
No. of Observations	234,415	233,492
Mean, μ (mm)	1.203	1.311
Std. Dev., σ (mm)	0.562	0.567
Maximum (mm)	5.926	5.524
<u>LOG-NORMAL DISTRIBUTION</u>		
μ_{LN}^*	-0.159	0.006
σ_{LN}^*	0.786	0.671
μ_o (mm)**	1.162	1.260
σ_o (mm)**	1.074	0.950

* μ_{LN} and σ_{LN} are the mean and standard deviation of the natural logarithm of asperity heights.

** μ_o and σ_o are estimates of the mean and standard deviation of the original measured distribution, from Bury (1975):

$$\mu_o = \exp[\mu_{LN} + (\sigma_{LN}^2/2)] \quad (3-2)$$

$$\sigma_o = [\exp(2\mu_{LN} + \sigma_{LN}^2) + \exp(\sigma_{LN}^2) - 1]^{1/2} \quad (3-3)$$

aperture. Table 3.2 shows that the log-normal model provides a good estimate of the mean asperity height but overestimates the standard deviation.

To get a visual indication of the large-scale roughness of the fracture, the data from all of the profiles was combined to create a 3-D perspective diagram of the bottom surface as shown in Figure 3.8. While some of the detail is lost in the

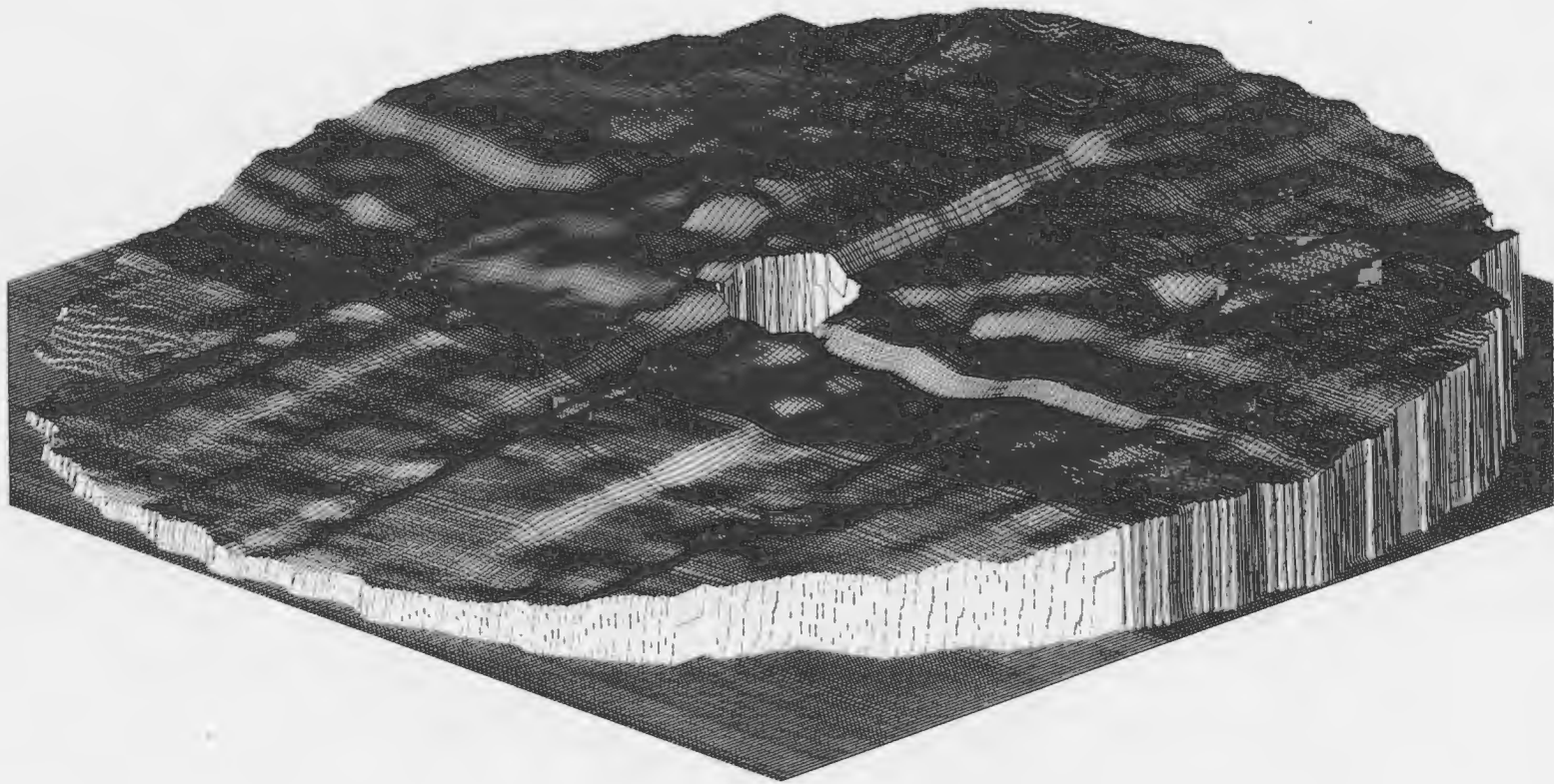


Figure 3.8 A 3-D perspective diagram of the large-scale roughness of the bottom fracture surface created by combining individual profile data.

mathematical smoothing process used to produce such a diagram, it is effective in giving an overall impression of the roughness of the fracture surface highlighting areas of topographic highs and lows and the presence of channels in the fracture plane. The borehole can be seen as a circular depression in the center of the diagram.

3.2.2 Small-scale roughness

Large-scale roughness features of the fracture are useful in classifying the type and condition of the fracture and may be important in terms of shear strength considerations. However, the movement of fluids within the fracture is also dependent on the small-scale roughness. These protrusions into the fracture plane not only increase resistance and drag by increasing the flow path length, but also break the fracture plane into a series of small, tortuous flow channels when they contact each other.

Because the small-scale roughness is masked by the waviness of the fracture, some means of filtering out the large-scale roughness is needed. One way in which this can be done is through graphical filtering (Thomas, 1982), a technique in which the fracture profile is divided into smaller segments and a reference line is fitted to each segment for measuring asperity heights. As the profile is broken down into smaller and smaller equal length segments, the large-scale roughness is removed so that only small-scale roughness is being measured (see Figure 3.9). Placing the tails

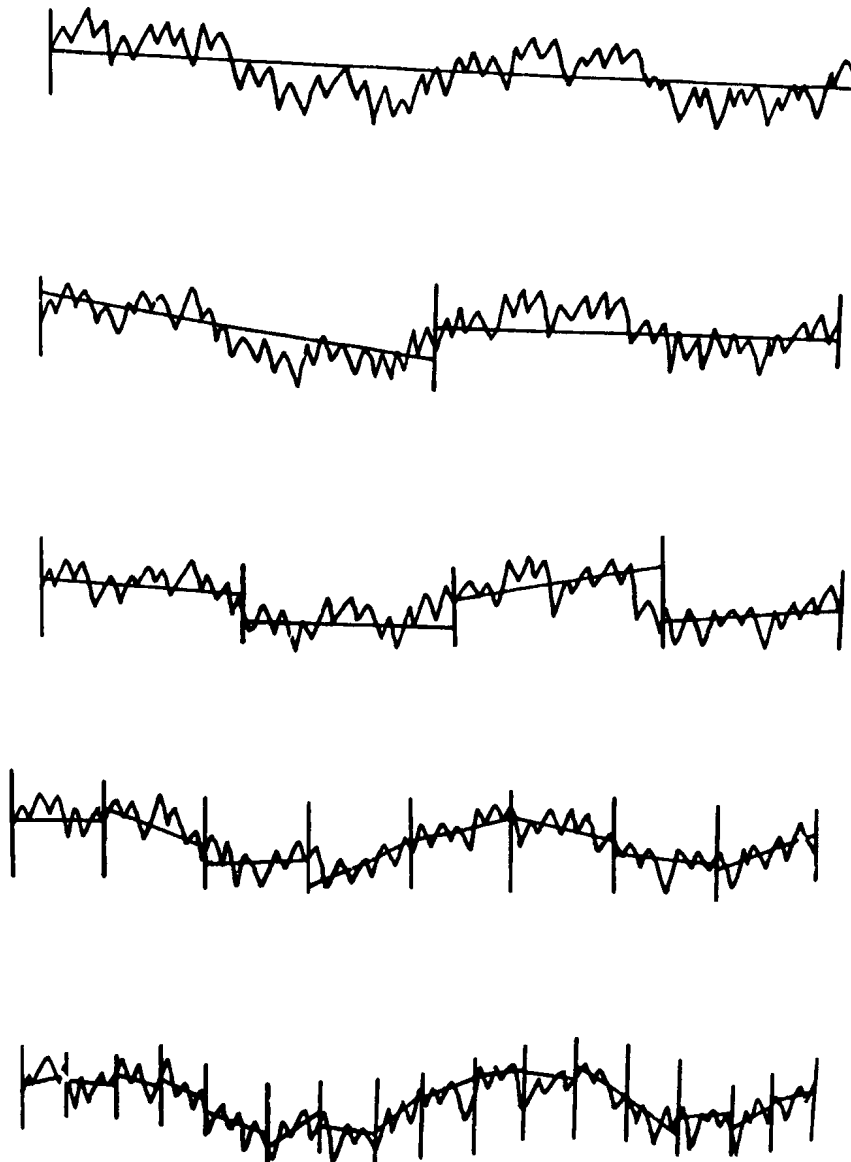


Figure 3.9 Schematic of the technique for graphical filtering in which reference lines are fitted to small segments of the fracture profile to remove large-scale roughness effects.

of the reference lines together to form a straight line produces a new profile that is independent of the shape (waviness) of the original profile.

The transition between large- and small-scale roughness is smooth and continual with no set division between the two. As a rule however, when the length of the straight line segment becomes smaller than the waviness of the profile, it can be assumed that the large-scale roughness has been filtered out. Figure 3.10 shows filtered roughness profiles for profile 80-3DX01 using segment lengths of approximately 30, 20, 10, 5 and 2 mm. The bottom asperity heights (lower profile) are plotted opposite the top asperity heights so that the two surfaces may be easily compared. The roughness profiles measured using segment lengths of 30 and 20 mm include large-scale roughness and are influenced by the shape of the profile. Those measured using segment lengths of 10 and 5 mm may still include some effects of the waviness of the profile. For the roughness profile measured with a 2 mm segment length, the large-scale roughness has been filtered out and only small-scale roughness is displayed.

Using an approach similar to the roughness angle envelope technique described by Rengers (1970) for asperity angles, mean asperity heights for profile 80-3DX01 for various segment lengths have been plotted in Figure 3.11(a). The top asperities are plotted as negative values and the bottom asperities as positive. The curves for both the top and bottom fracture surfaces show that the mean asperity height decreases towards some minimum value as the segment length is made smaller

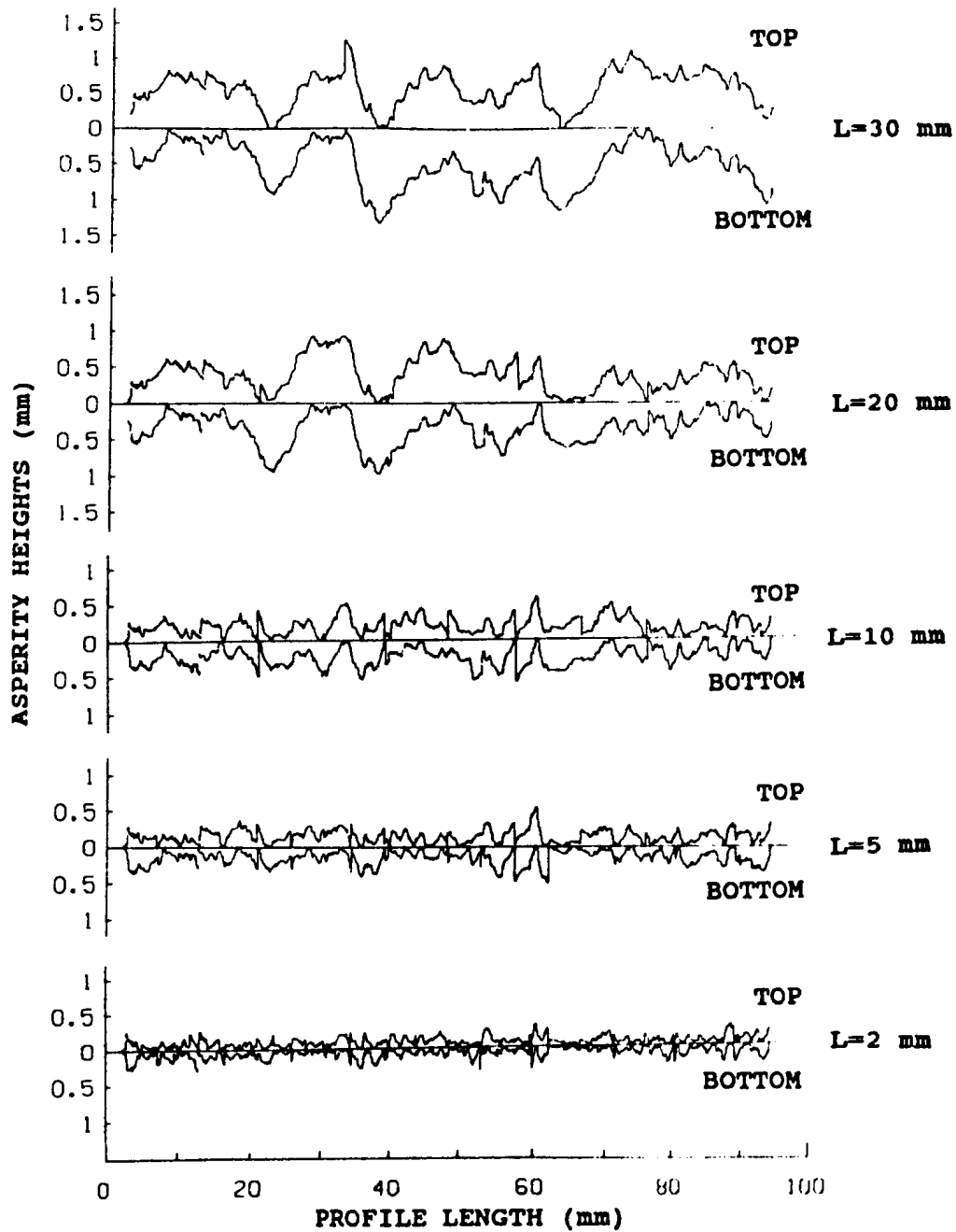
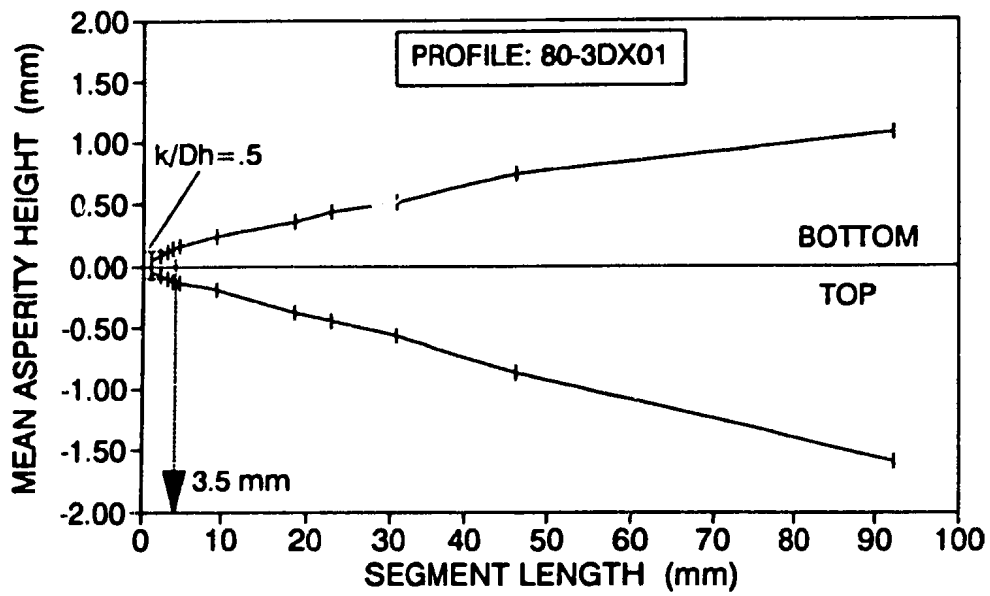
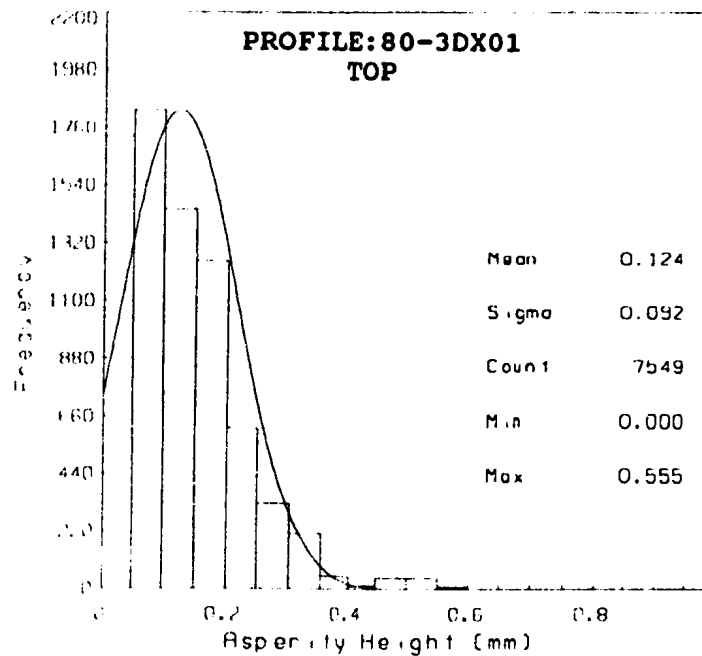


Figure 3.10 Filtered roughness profiles for both the top and bottom surfaces of profile 80-3DX01 using segment lengths of 30, 20, 10, 5 and 2 mm.



(a)



(b)

Figure 3.11 (a) Mean asperity height vs. segment length diagram for profile 80-3DX01 (b) Frequency histogram of small-scale asperity heights for profile 80-3DX01 using a segment length of 3.5 mm.

corresponding to the change from large-scale to small-scale roughness measurement. Since fluid flow is very much dependent on small-scale roughness, it remains to be determined what measuring length (segment length) best extracts the scale of roughness that is important for flow considerations. From the original roughness profiles one can qualitatively determine that the small-scale roughness for this fracture must be measured using measuring lengths less than about 10 mm.

The roughness - flow relationship is commonly described in terms of the size of the asperities on the fracture wall compared to the size of the fracture opening i.e. relative roughness. As described earlier, relative roughness, k/D_h , may be defined (Louis, 1969) as the average or mean height of the asperities, e_m , divided by twice the fracture aperture, $2b$. In the case of rough fractures in contact, k/D_h should equal 0.5, the maximum relative roughness theoretically possible. As will be shown later, the mean fracture aperture for profile 80-3DX01 was determined to be 0.125 mm. To satisfy the condition of $k/D_h = 0.5$ implies that the mean asperity height should also be 0.125 mm. The point representing $k/D_h = 0.5$ for both fracture surfaces has been indicated in Figure 3.11(a) and corresponds to a segment length of about 3.5 mm. Thus roughness measurements made by breaking the profile down into 3.5 mm segments should quantify the small-scale roughness characteristics of the fracture that are important for fluid flow. Figure 3.11(b) shows the frequency histogram of asperity height measurements made from the top surface of profile 80-3DX01 using

a measuring length of about 3.5 mm. The distribution is skewed to the left with a mean asperity height of 0.124 mm which is very close to the predicted value.

Figure 3.12 shows the mean asperity height versus segment length diagram for several profiles in both the x- and y-directions. All profiles show the same general trend of decreasing mean asperity height with decreasing segment length, a variable large-scale roughness as indicated by the "tails" of the curves and a rather constant small-scale roughness. The points representing a relative roughness of 0.5 correspond to measuring lengths of 2.5 - 3.5 mm. The asperity heights for all forty eight profiles were measured using segment lengths in the 2.5 - 3.5 mm range and have been combined in the histograms shown in Figure 3.13. From over 116,000 observations, the measured distributions for both the top and bottom surfaces were found to be highly skewed and very similar in appearance with mean asperity heights of 0.103 and 0.102 mm respectively. Complete overlap of the calculated confidence intervals for the two distributions suggests that there is no difference between the top and bottom small-scale asperity height distributions. It is anticipated that these asperity height distributions will be similar to the aperture distributions given the direct relationship between asperity height distribution and aperture for fracture surfaces in contact. The distribution of natural logarithms of small-scale asperity heights for both surfaces are shown in Figure 3.14. A normal curve has been superimposed to determine if the data is better approximated by log-normal distribution. However, the log-normal distribution does not appear to offer any better approximation to the data than the

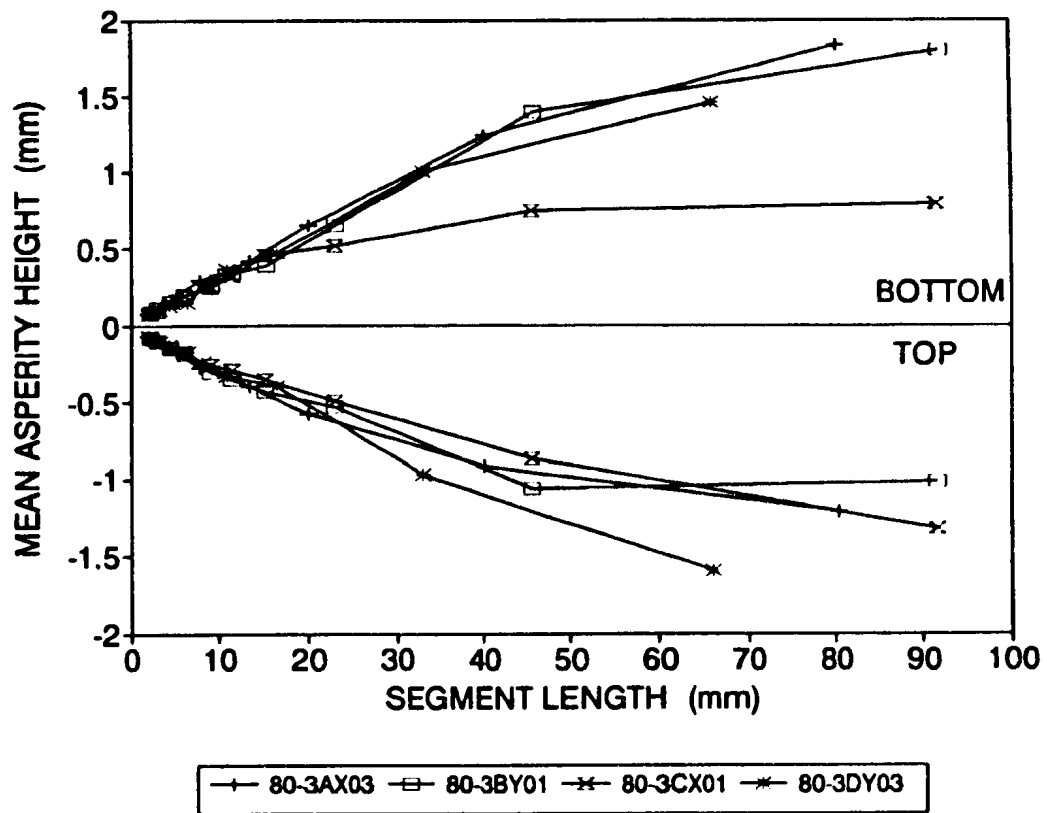


Figure 3.12 Mean asperity height vs. segment length diagram for selected profiles.

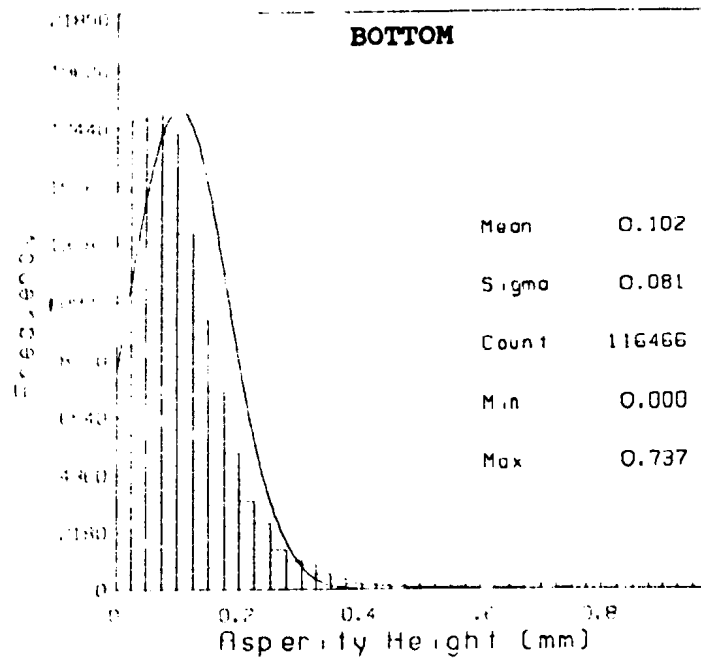
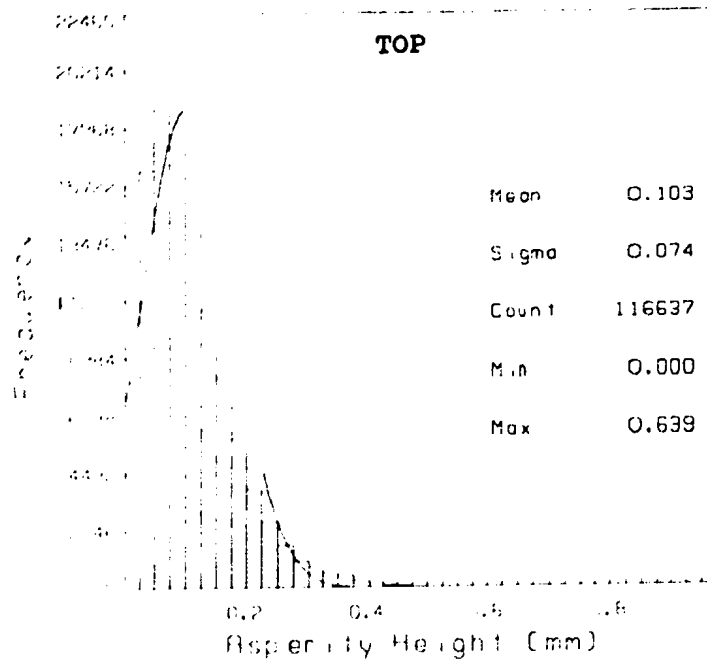


Figure 3.13 Frequency histograms of small-scale asperity heights for top and bottom surfaces of all combined profiles with superimposed normal distribution curves.

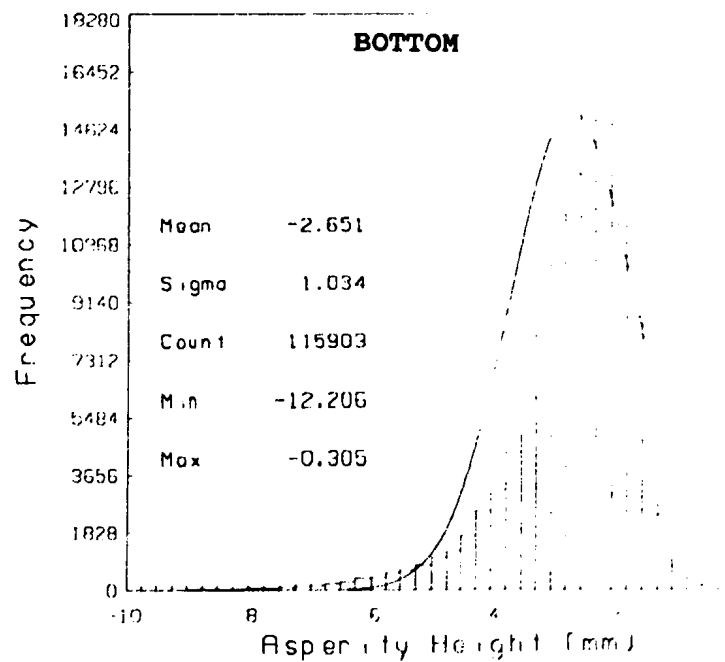
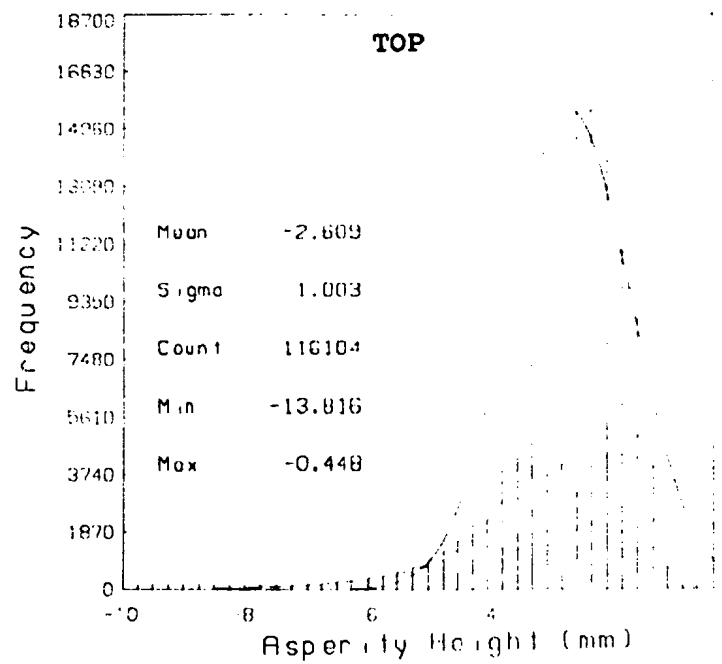


Figure 3.14 Frequency histograms of the natural logarithms of small-scale asperity heights for top and bottom surfaces of all combined profiles with superimposed log-normal distribution curves.

normal distribution in Figure 3.13. The statistics on the small-scale roughness measurements are given in Table 3.3.

Table 3.3 Summary statistics on small-scale roughness measurements from all fracture profiles combined.

	TOP ASPERITY HEIGHTS	BOTTOM ASPERITY HEIGHTS
<u>MEASURED DISTRIBUTION</u>		
No. of observations	116,637	116,466
Mean, μ (mm)	0.103	0.102
Std. Dev., σ (mm)	0.074	0.081
Maximum (mm)	0.639	0.737
<u>LOG-NORMAL DISTRIBUTION</u>		
μ_{LN}^*	-2.609	-2.651
σ_{LN}^*	1.003	1.034
μ_o (mm)**	0.122	0.120
σ_o (mm)**	0.160	0.167

* μ_{LN} and σ_{LN} are the mean and standard deviation of the natural logarithm of asperity heights.

** μ_o and σ_o are estimates of the mean and standard deviation of the original measured distribution (see equations (3-2) and (3-3) in Table 3.2).

3.2.3 Contact area

Since the resin was injected into the fracture plane while both surfaces of the fracture were in contact, the resin injection technique provides a means for measuring the contact area under given normal stress conditions. For this study, the

normal stress on the sample during resin injection was 1.0 MPa. Areas of contact are recognized in cross section as (1) areas where the top and bottom profiles are in mutual contact with each other and hence do not show any resin between them and (2) rock fragments wedged in the fracture plane that block the passage of resin and create a rock bridge between the top and bottom surfaces.

For all forty eight profiles from the sample, areas of contact were flagged during the digitizing process so that individual contact lengths could be measured. The sum of the individual contact lengths was calculated as a percentage of the total length of the profile to provide an estimate of the contact area for each profile. To obtain a reasonable estimate of the contact area for the entire sample, the sum of all the contact lengths measured from each profile was compared to the sum of all the total profile lengths. This yielded a value of 5.3% which is assumed to approximate the total fracture contact area at a normal stress of 1.0 MPa.

Figure 3.15(a) is a frequency histogram of the distribution of individual contact lengths measured from all of the profiles. Almost all of the contact lengths are less than 3 mm with a mean of 0.99 mm and a standard deviation of 1.67 mm. The skewness of the data suggests that the distribution may be better approximated by a log-normal model. In Figure 3.15(b), natural logarithms of the contact lengths have been taken and the resulting frequency histogram does indeed approximate a log-normal distribution. The statistics of the distribution of individual contact lengths, including the log-normal approximations, are summarized in Table 3.4.

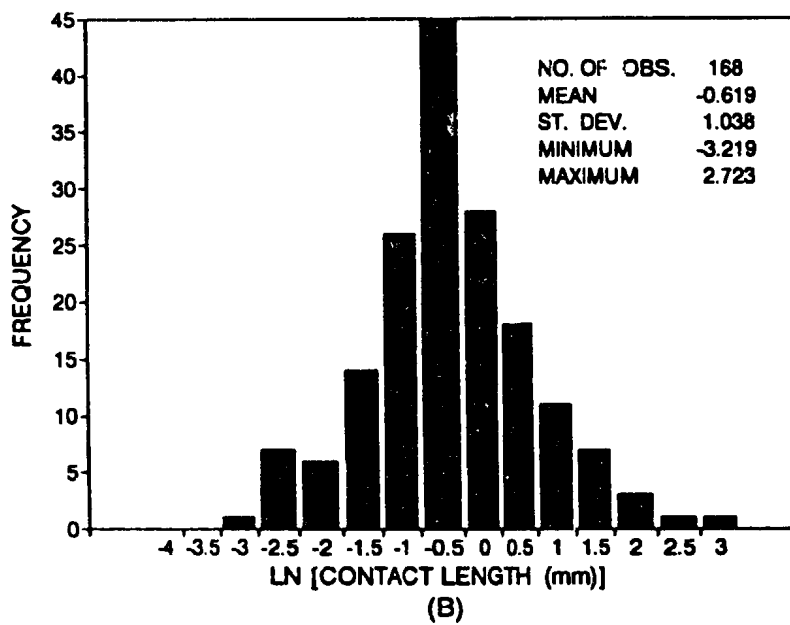
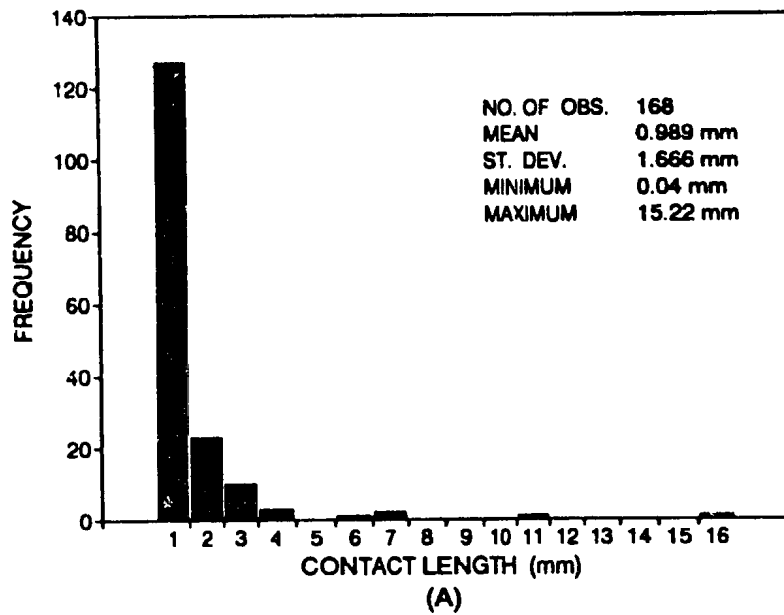


Figure 3.15 (a) Frequency histogram of individual contact lengths from all combined profiles (b) log-normal distribution of contact lengths.

Table 3.4 Summary statistics on individual contact length measurements from all fracture profiles combined.

<u>MEASURED DISTRIBUTION</u>		CONTACT LENGTHS
No. of Observations		168
Mean, μ (mm)		0.989
Std. Dev., σ (mm)		1.666
Minimum (mm)		0.04
Maximum (mm)		15.22
<u>LOG-NORMAL DISTRIBUTION</u>		
μ_{LN}^*		-0.619
σ_{LN}^*		1.038
μ_o (mm)**		0.923
σ_o (mm)**		1.284

* μ_{LN} and σ_{LN} are the mean and standard deviation of the natural logarithm of contact lengths.

** μ_o and σ_o are estimates of the mean and standard deviation of the original measured distribution (see equations (3-2) and (3-3) in Table 3.2).

The spatial distribution of contact points across the sample is shown in Figure 3.16. The different lengths of contact have been represented by circles of proportionate size to give an indication of the relative size and location of individual contact areas measured from the profiles. Although the diagram was constructed from a series of cross-sections through the sample, and hence does not show all the areas of contact in the fracture plane, it does allow certain generalizations to be made. For example, it is observed that the contact areas are fewer in number and

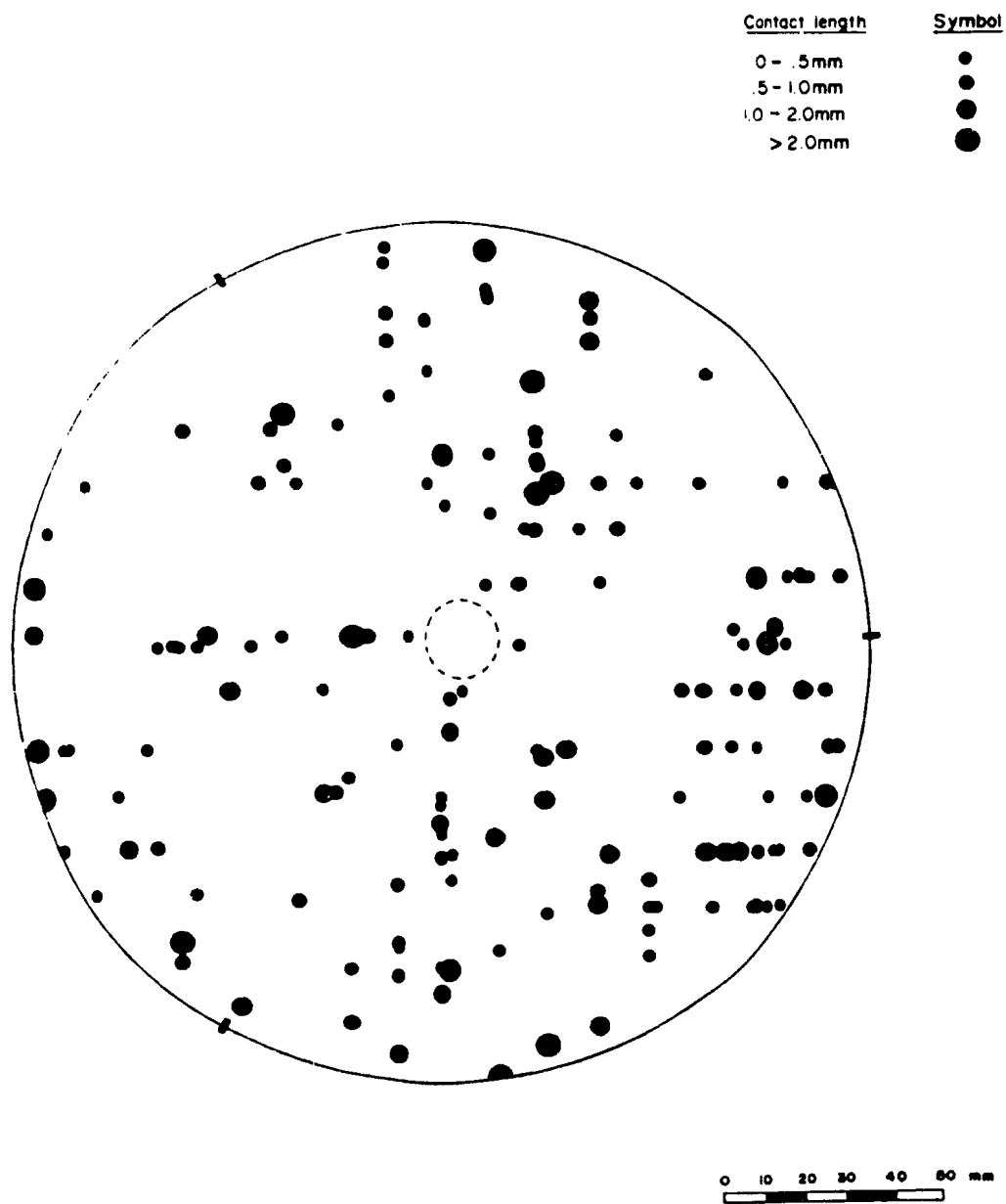


Figure 3.16 Spatial distribution of contact points across the fracture plane.

size in the upper left portion of the diagram than in the lower right portion. Therefore flow may be greater in that area since the flow channels are more open and there is less obstruction to fluid movement.

3.2.4 Aperture and void space

The resin injection technique is well-suited for characterizing fracture aperture and void space for given normal stress and flow rate conditions. In cross section, the resin is effective in highlighting the relative position of the top and bottom surfaces of the fracture for measuring local apertures while the distribution of resin in the fracture plane gives an indication of the size and shape of the voids. Measurements of fracture aperture and resin thickness were made from the digitized data for each of the profiles at regular intervals of 0.05 mm. Apertures and resin thicknesses as small as 1 μm were capable of being measured at the magnification used in these studies. Any apertures smaller than this were assumed to be hairline fractures and to contribute very little to fluid flow. Figure 3.17 shows plots of aperture and resin thickness against profile length for the two profiles shown in Figure 3.4. Aperture and resin thickness are plotted opposite each other so that the aperture distribution and the distribution of resin in the fracture can be compared. While the vertical scale has been exaggerated in order to bring out the details of the measurements, the diagrams do give a good indication of the aperture variation along the profile. Note that all apertures in both profiles are less than 0.5 mm. For the most part, the resin

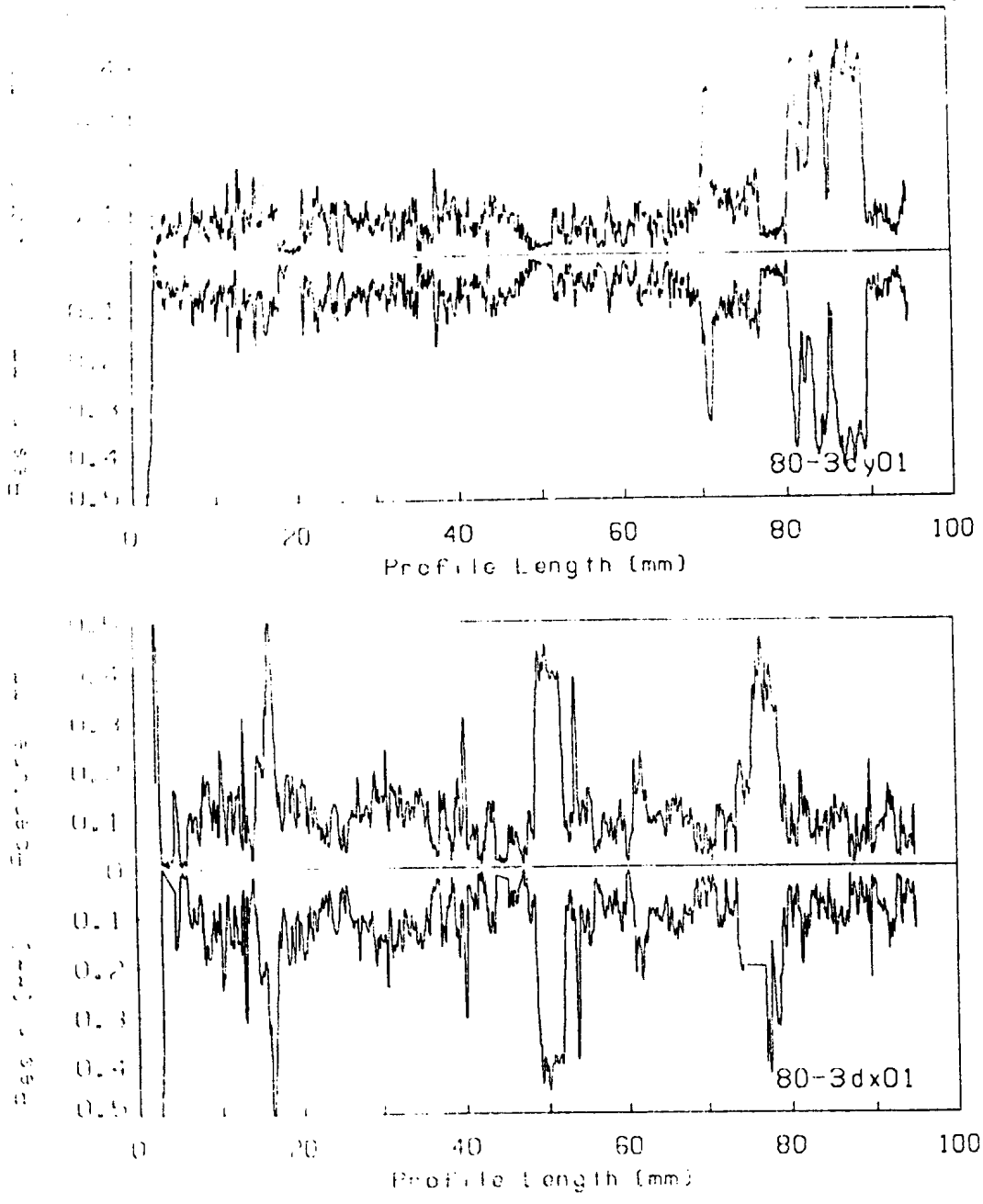


Figure 3.17 Plots of aperture and resin thickness against profile length for two selected profiles. The vertical scale has been exaggerated to bring out the details.

thickness plots are mirror images of the aperture distribution. This indicates excellent impregnation of the fracture with resin and no dead end pore space that could not be penetrated by the resin. Areas of the fracture that were not filled with resin, due to obstruction by a rock fragment for example, are marked by more or less horizontal straight line segments in the resin thickness profile. Several such lines are easily recognizable in profile 80-3DX01.

The aperture and resin thickness data from all forty eight profiles are combined in the frequency histograms shown in Figure 3.18. The distributions of measured apertures and resin thickness are bounded by zero on the left and highly skewed with a mean aperture of 0.103 mm and a mean resin thickness of 0.099 mm. The maximum aperture was 1.5 mm. The similarity between the two distributions indicates that most of the open pore space in the fracture plane was impregnated with resin. The skewness of these distributions suggests that a log-normal model may provide a good approximation to the data. In Figure 3.19, the frequency histograms of the natural logarithms of aperture and resin thickness do indeed show a good fit with a superimposed normal distribution curve based on the measured mean and standard deviation. As predicted, the aperture distribution is very similar to the small-scale roughness distribution shown in Figure 3.13 emphasizing the interrelationship between small-scale roughness and aperture.

Another way of representing the distribution of apertures is through the use of box plots (modified after Chambers et al., 1983). as shown for several selected

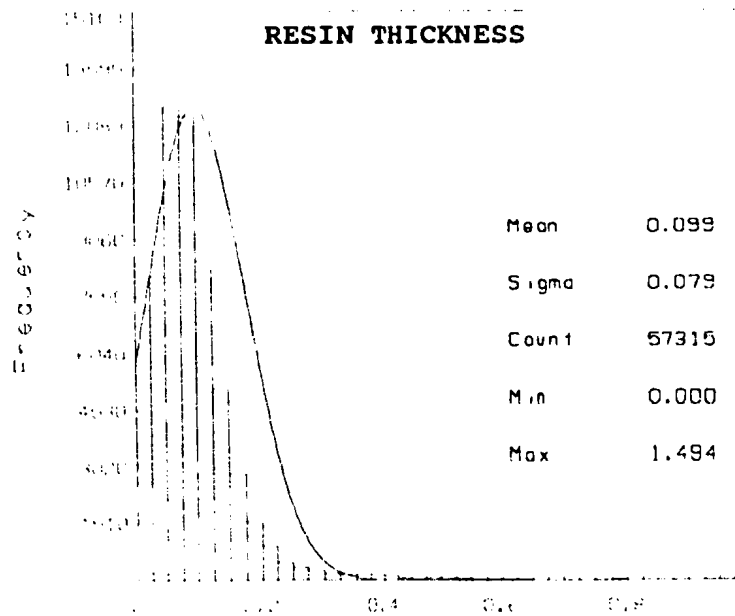
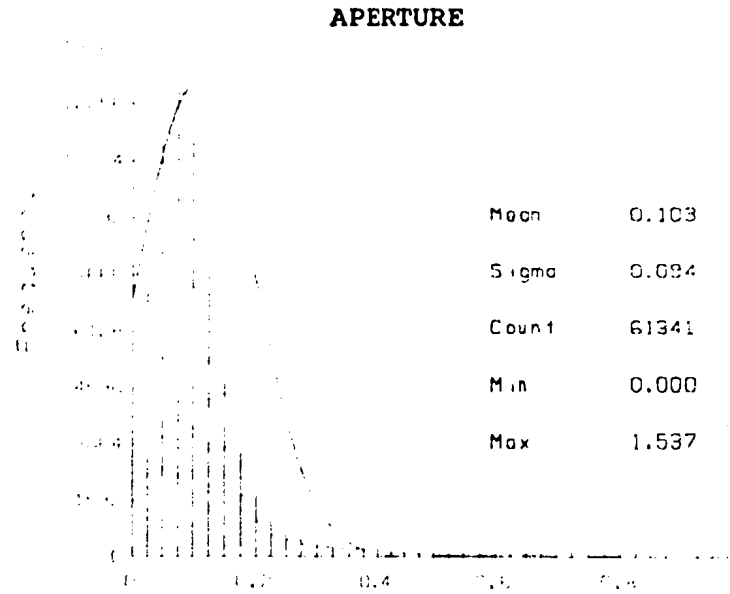


Figure 3.18 Frequency histograms of aperture and resin thickness from all profiles combined.

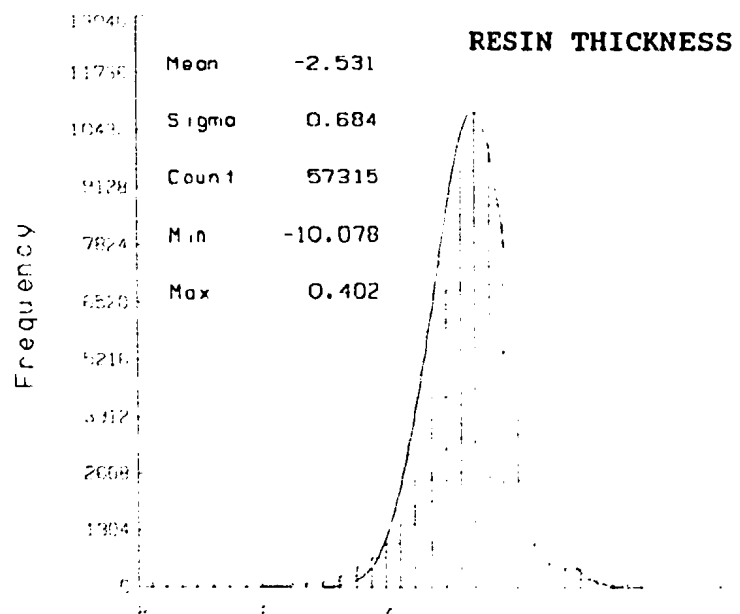
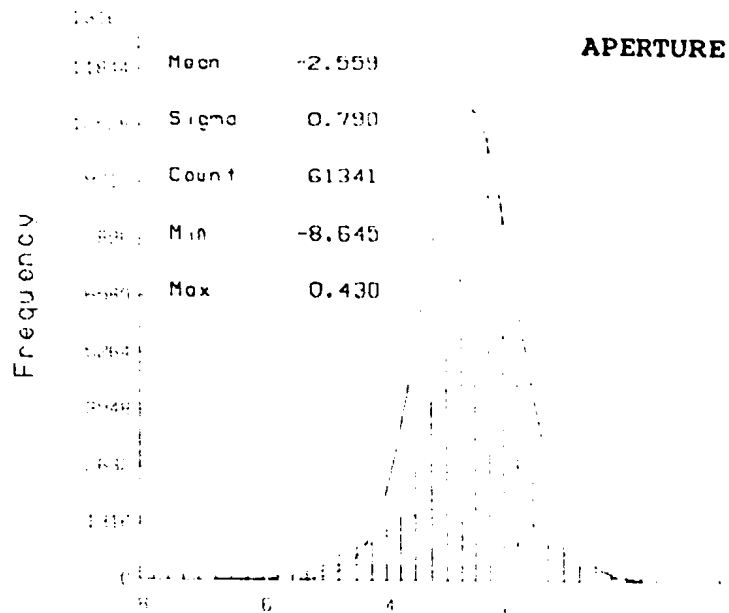


Figure 3.19 Frequency histograms of the natural logarithms of aperture and resin thickness from all profiles combined.

profiles in Figure 3.20. For each profile, the box plots show where the middle portion of the apertures fall as indicated by the bottom (25% quartile) and top (75% quartile) edges of the box, the median value (50% quartile), the mean value and the maximum and minimum values. The relative lengths of the upper and lower "tails" give an indication of the skewness of the data. The apertures for the profiles in Figure 3.20 are clustered about the 0.1 mm aperture value with short lower tails, due to the zero lower limit, and long upper tails of varying length depending on the maximum measured aperture. The median values may represent a better estimate of the fracture aperture since the mean values are strongly influenced by the maximum values. The box plots are very helpful in comparing the aperture distributions from profile to profile.

The basic statistics on aperture and resin thickness distributions for all of the profiles combined, profiles in the x-direction only, and profiles in the y-direction only, are given in Table 3.5. The parameters of the log-normal distribution and estimates of the mean and standard deviation are also given in Table 3.5. It is important to note that the mean measured fracture aperture of 103 μm at 1 MPa is greater than the equivalent hydraulic aperture of 8 μm computed from the flow test data using the cubic law (see Table 3.1). The estimates of the original distribution from the log-normal distribution parameters suggest that the log-normal model provides a good approximation to the aperture data. The profiles have been separated into x- and y-directions to determine if there is any anisotropy in the fracture plane as far as

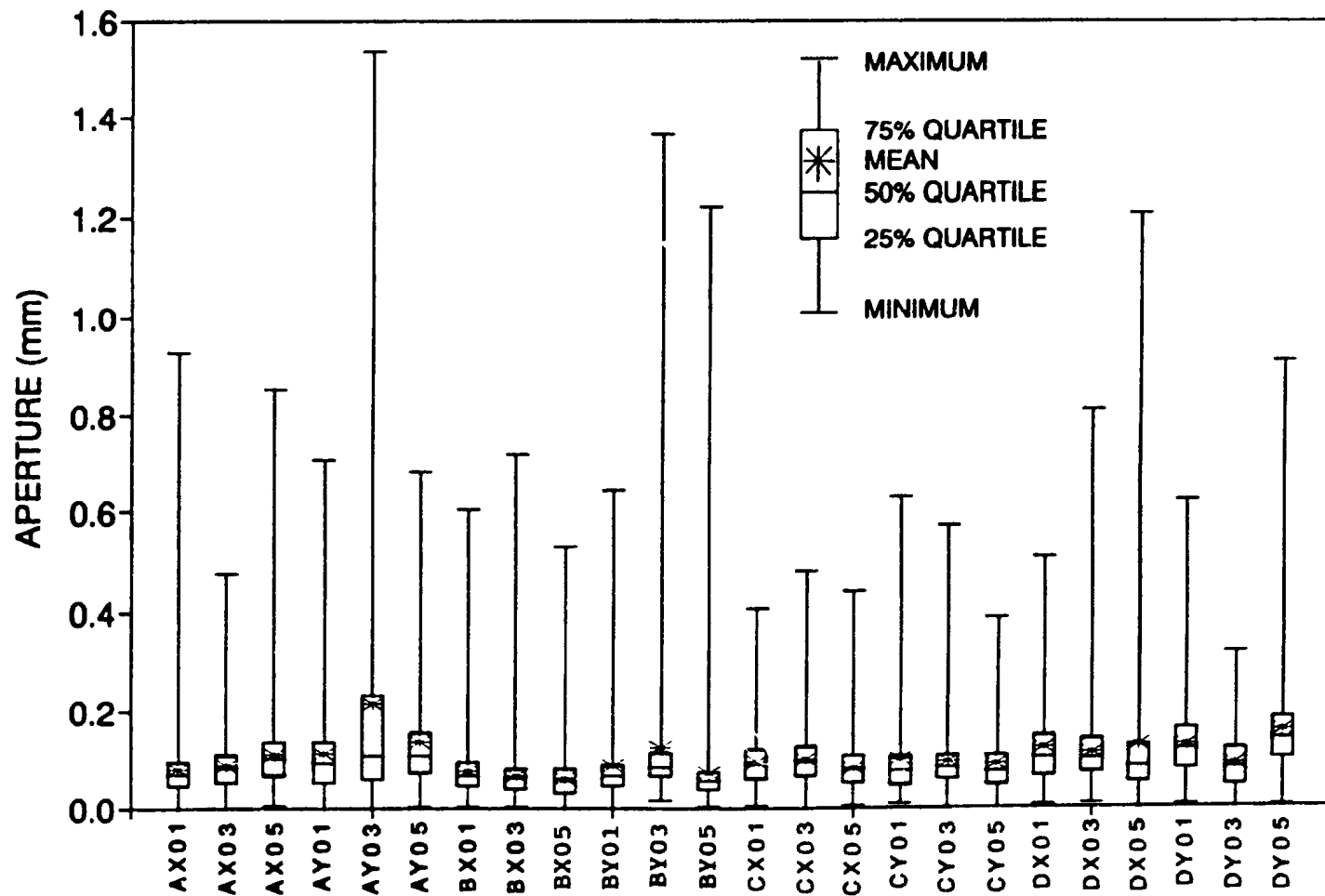


Figure 3.20 Modified box plots of aperture distributions for selected fracture profiles.

Table 3.5 Summary statistics on aperture and resin thickness measurements from all fracture profiles combined.

	TOTAL APERTURE			RESIN THICKNESS		
	all	x-dir	y-dir	all	x-dir	y-dir
MEASURED DISTRIBUTION						
No. of Obs.	61341	32938	28403	57315	31159	26156
Mean, μ (mm)	0.103	0.097	0.109	0.099	0.097	0.101
Std. Dev., σ (mm)	0.094	0.082	0.106	0.079	0.076	0.082
Maximum (mm)	1.537	1.209	1.537	1.494	1.221	1.494
LOG-NORMAL DISTRIBUTION						
μ_{LN}^*	-2.559	-2.596	-2.516	-2.531	-2.545	-2.513
σ_{LN}^*	0.790	0.779	0.801	0.684	0.682	0.687
μ_o (mm)**	0.106	0.101	0.111	0.101	0.099	0.103
σ_o (mm)**	0.098	0.092	0.106	0.078	0.076	0.080

* μ_{LN} and σ_{LN} are the mean and standard deviation of the natural logarithm of aperture and resin thickness.

** μ_o and σ_o are estimates of the mean and standard deviation of the original measured distribution (see equations (3-2) and (3-3) in Table 3.2).

apertures are concerned. Judging by the complete overlap of confidence intervals for the two distributions, it is inferred that the x-direction and y-direction apertures are not statistically different. Thus it would not appear that there is any preferred direction for fluid flow in the fracture.

In addition to measuring aperture and resin thickness, the geometry of the void space was characterized by measuring cross-sectional areas and aspect ratios of

the individual voids making up the fracture plane. The size of an individual void may be described by its cross-sectional area. The shape of the void in cross-section is best described by its aspect ratio, x/z or y/z . The combined data on cross-sectional areas of voids and void aspect ratios are summarized in the frequency histograms presented in Figure 3.21 and Figure 3.22 respectively. In Figure 3.21(a), the distribution of cross-sectional areas of voids is highly skewed to the left ranging from 6.4 mm^2 down to 0.002 mm^2 . The mean void size is about 1.2 mm^2 with most of the voids being less than 2 mm^2 in area. A normal curve has been drawn in representing a normal distribution. The log-normal distribution of void areas is shown in Figure 3.21(b) and shows a little better approximation to the data. The normal and log-normal distributions of void aspect ratios are shown in Figure 3.22(a) and (b). The mean aspect ratio of about 7 indicates that the voids are flattened ellipses in the x- or y-directions. An aspect ratio of 1 indicates a circle, while an aspect ratio of less than 1 indicates a flattened ellipse in the z-direction i.e. orthogonal to the plane of the fracture.

The basic statistics on the size and shape of the individual voids are given in Table 3.6 which also includes the log-normal distribution statistics. Judging from the estimates of the measured distributions from the log-normal distribution parameters, the log-normal model only gives a semi-quantitative characterization of the data. However, the histograms seem to indicate a better fit than the estimates suggest. The data has also been analyzed in terms of x- and y-directions to determine if there

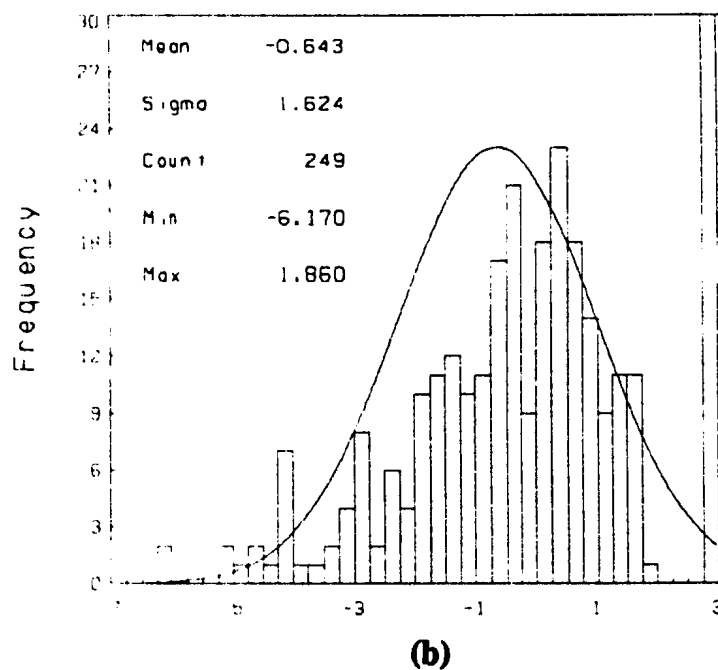
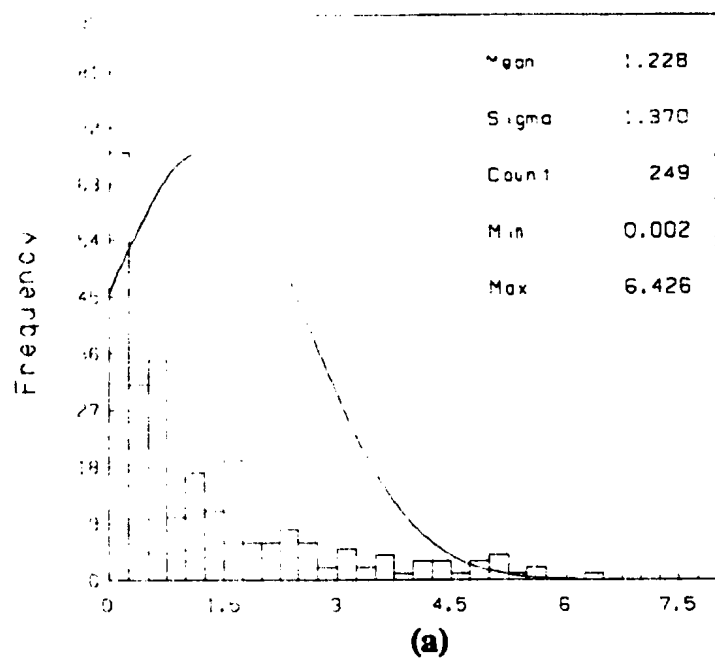


Figure 3.21 Frequency histograms of (a) void areas and (b) natural logarithm of void areas from all profiles combined. Normal and log-normal distribution curves are shown.

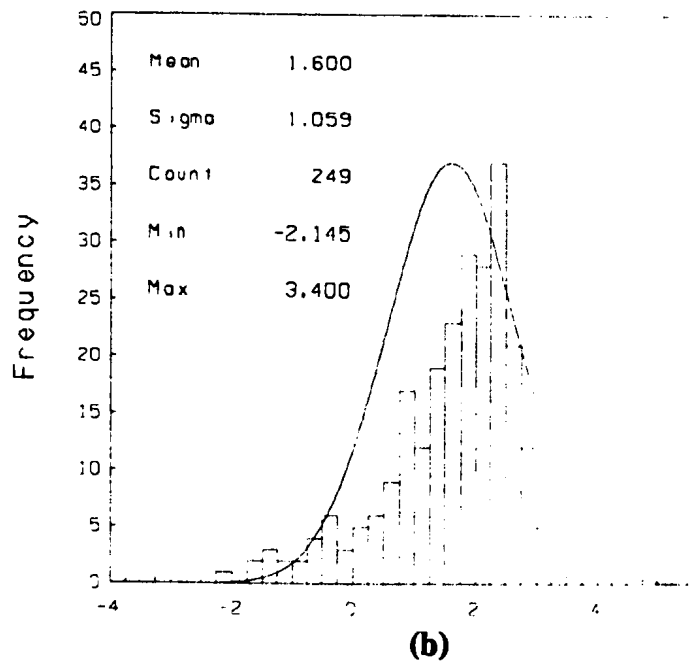
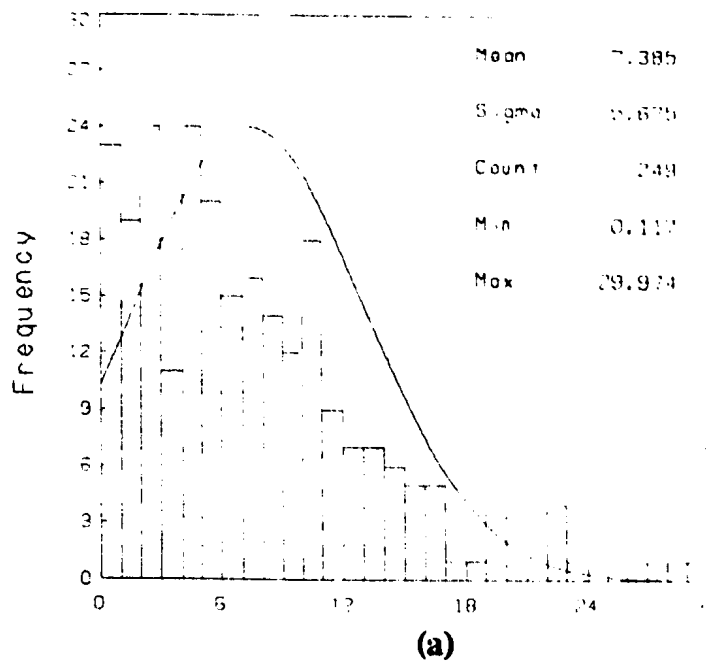


Figure 3.22 Frequency histograms of (a) aspect ratios and (b) natural logarithms of aspect ratios from all profiles combined. Normal and log-normal distribution curves are shown.

Table 3.6 Summary statistics on void area and aspect ratio measurements from all fracture profiles combined.

	VOID AREA (mm ²)			ASPECT RATIO		
	all	x-dir	y-dir	all	x-dir	y-dir
MEASURED DISTRIBUTION						
No. of Obs.	249	141	108	249	141	108
Mean, μ	1.228	1.146	1.335	7.385	7.489	7.250
Std. Dev., σ	1.370	1.417	1.304	5.675	5.512	5.905
Minimum	0.002	0.002	0.010	0.117	0.117	0.191
Maximum	6.426	6.426	5.637	29.974	28.922	29.974
LOG-NORMAL DISTRIBUTION						
μ_{LN}^*	-0.643	-0.832	-0.397	1.600	1.607	1.592
σ_{LN}^*	1.624	1.738	1.433	1.059	1.109	0.994
μ_o^{**}	1.965	1.971	1.877	8.678	9.225	8.053
σ_o^{**}	7.080	8.703	4.893	12.483	14.354	10.456

* μ_{LN} and σ_{LN} are the mean and standard deviation of the natural logarithm of void area and aspect ratio.

** μ_o and σ_o are estimates of the mean and standard deviation of the original measured distributions (see equations (3-2) and (3-3) in Table 3.2).

are any directional tendencies. The data in Table 3.6 does not suggest that there is any appreciable differences in void areas and aspect ratios between the x- and y-directions, although more complete statistical testing could be carried out to confirm this. Thus it cannot be concluded that there is a greater tendency for flow in one direction than the other.

In order to show the spatial distribution of aperture and pore space throughout the fracture plane, the data from each profile has been combined to produce the contour diagrams shown in Figure 3.23 and Figure 3.24. The space between the profiles has been interpolated from the measured data points to produce contoured plots of aperture and resin thickness. Both plots are very similar, once again indicating excellent impregnation of the fracture with resin, with the majority of the measured apertures and resin thicknesses in the 60 to 120 μm range. The upper and left portion of the diagrams are marked by several pockets of larger apertures as indicated by a high density of concentric contour lines; the apertures in the lower and right portion of the diagrams tend to be smaller and more evenly distributed. Note that the contour interval is 0.02 mm (20 μm). While using such a small contour interval may impart a bulls-eye pattern in the large aperture regions, a small interval is warranted to highlight the many small individual flow paths and constrictions that exist across the fracture plane. The hydraulic aperture calculated in Table 3.1 for the resin cycle at 1 MPa was only 5 to 8 μm .

The same data used to produce the contoured aperture plot in Figure 3.23 was used to create a 3-D mesh plot of apertures within the fracture plane as shown in Figure 3.25. A vertical exaggeration has been added to the diagram to highlight the aperture differences. The high points in the diagram are equivalent to the areas with concentric circles in Figure 3.23 and indicate areas with larger apertures. The flatter regions in Figure 3.25 indicate areas with small apertures.

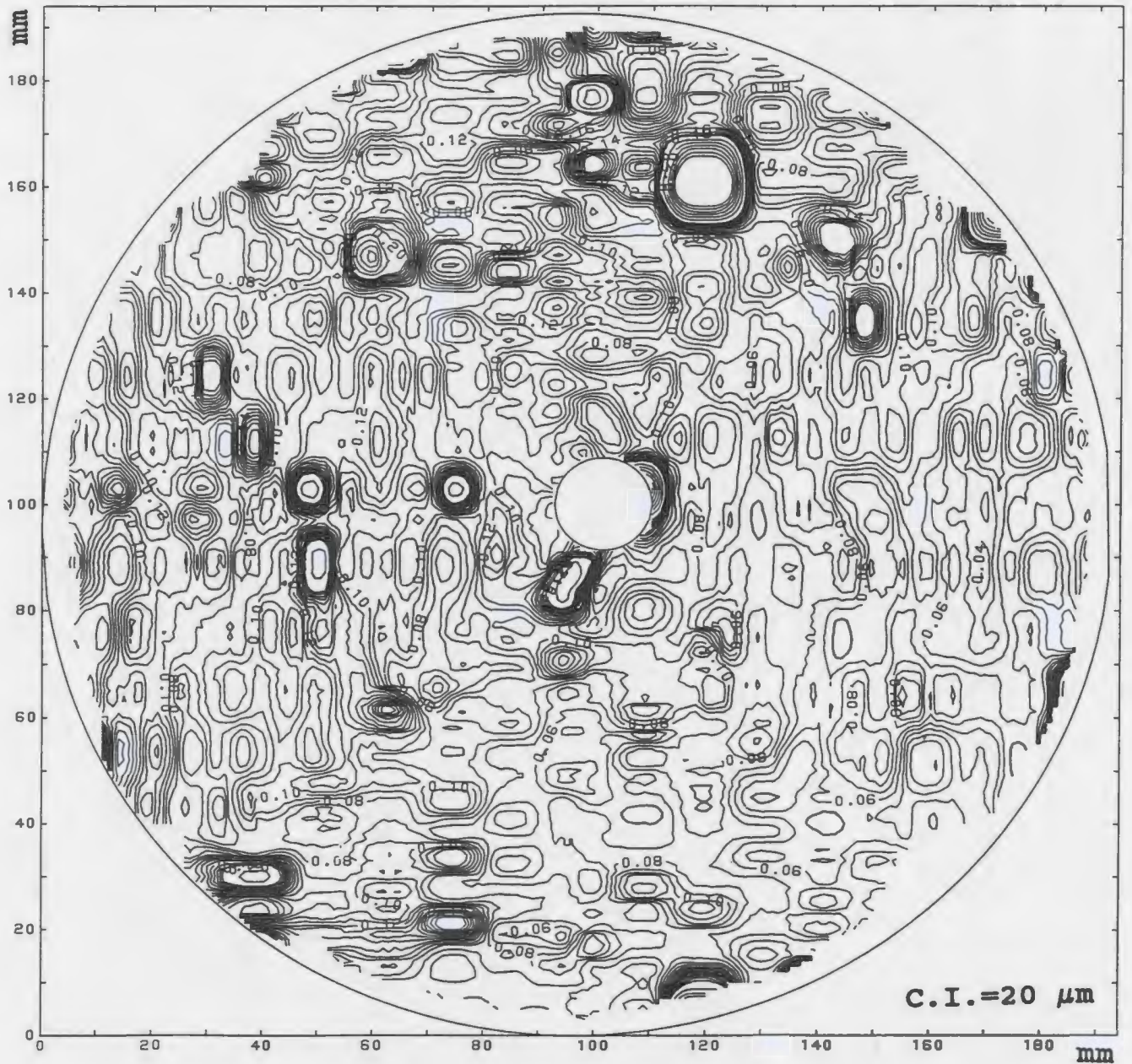


Figure 3.23 Aperture contour diagram showing the spatial distribution of apertures within the fracture plane. The contour interval is 20 μm .

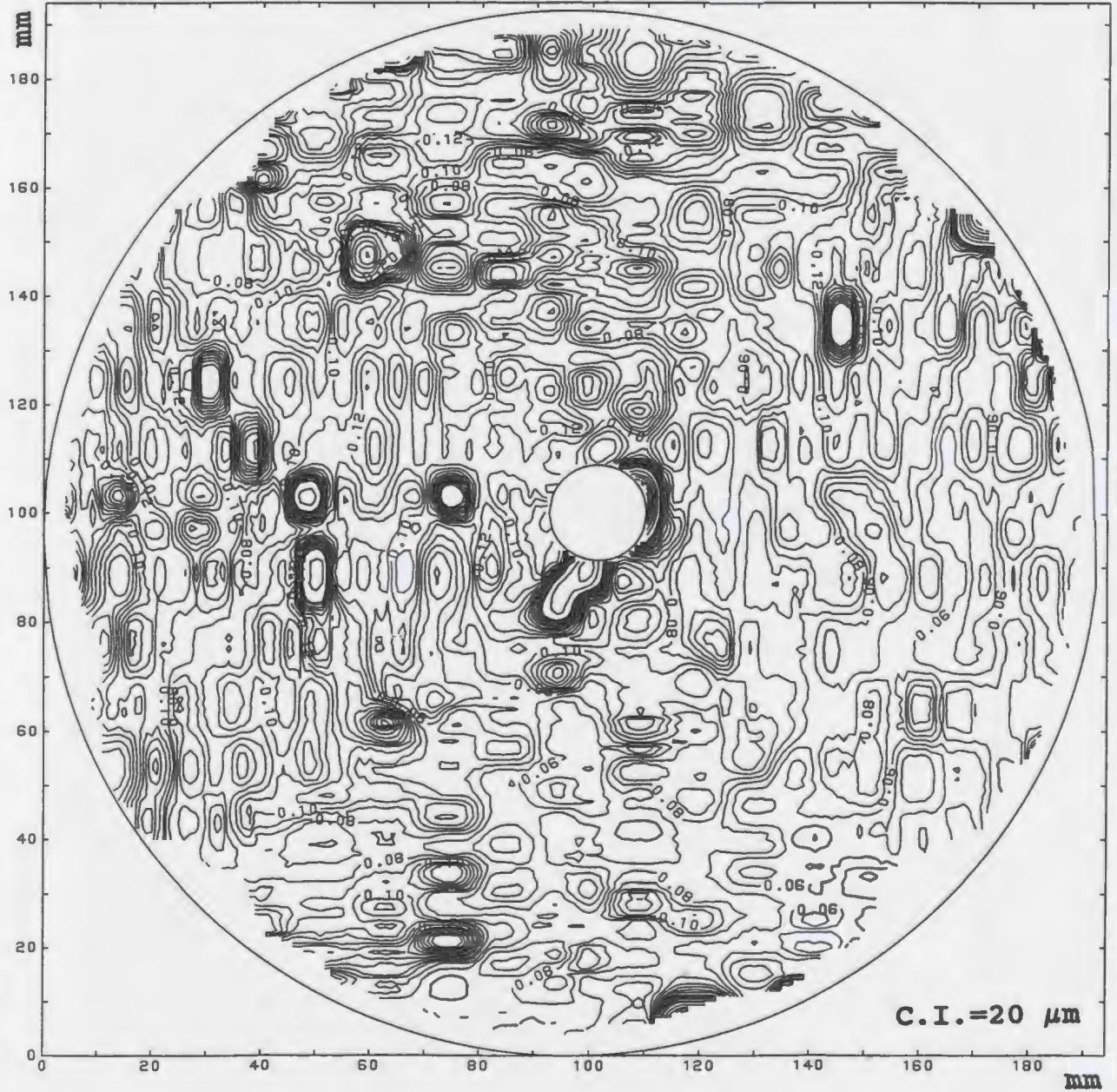


Figure 3.24 Resin thickness contour diagram showing the spatial distribution of resin within the fracture plane. The contour interval is 20 μm.

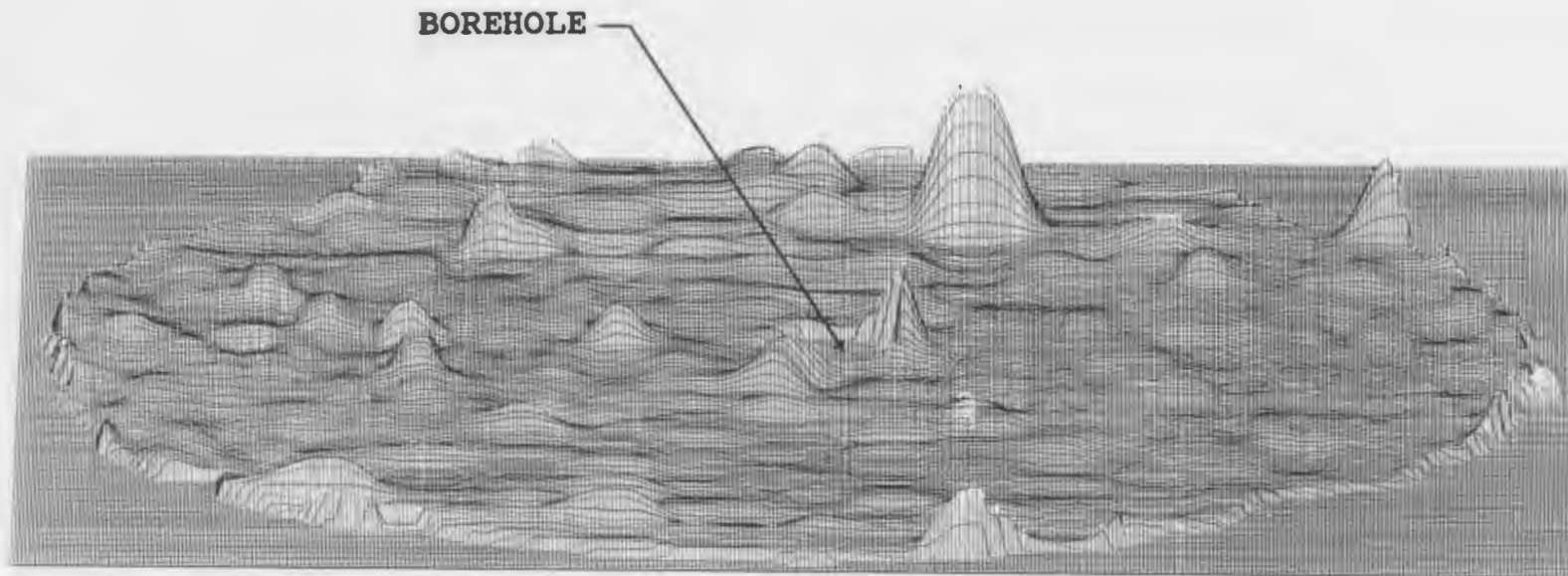


Figure 3.25 A 3-D mesh plot of apertures within the fracture plane. A vertical exaggeration has been added to highlight the aperture differences.

Chapter 4 EVALUATION AND COMPARISON OF STRESS-FLOW MODELS

One of the primary objectives in characterizing and flow-testing individual fractures under controlled laboratory conditions is to develop a means for modelling the hydraulic behaviour from a minimum knowledge of the fracture or fractures in question. In this chapter, the data obtained from the flow tests and resin injection experiment is used to evaluate several theoretical and empirical models relating fracture permeability to normal stress.

4.1 The Gangi Bed of Nails Model

The theoretical approach presented by Gangi (1978, 1981) was one of the first efforts at modelling the physical processes involved in the stress-flow relationship observed for fractured rock. In his model, the asperities on the fracture surfaces were represented by pencil-shaped rods or nails of different heights and diameters. Fracture closure under increasing normal stress was considered to be the result of elastic deformation of a few tall "asperities" which propped the fracture open. By assuming a power law distribution of asperity heights, he derived an expression relating fracture permeability, k , to effective pressure, P , as follows:

$$k = k_0 [1 - (P/P_1)^m]^3 \quad (4-1)$$

where k_0 is the zero-pressure permeability of the fracture, P_1 is the effective modulus of the asperities (determined by multiplying the Young's modulus, E , of the material by the fraction of the fracture face covered with rods, A/A_0) and m is the reciprocal of the power n in the power law distribution. Gangi states that the contact area ratio, A/A_0 , is generally small ranging between 1% and 10%.

Gangi suggested that the magnitude of n in the power law distribution function gives an indication of the roughness characteristics of the fracture surface. For example, a well-polished surface with asperity peaks that are all about the same height would have a small n value close to 1 whereas a fresh, rough surface with a few tall asperities that stick out into the fracture plane would be characterized by a large n value. Gangi found that his theoretical curves produced a good fit to the experimental data of Nelson and Handin (1977) and Jones (1975) for artificial fractures in sandstone and carbonate rocks respectively. The n values for these curves ranged from 4.5 to 9.

Results of replacing k in equation (4-1) with normalized flow rate are shown in Figure 4.1 which compares theoretical curves generated from the Gangi model with data from the first loading cycle for the fracture used in this study. Although the curves show the same general shape, a good fit of the data could not be obtained. With a Young's modulus for this particular granite of 75 GPa, the effective modulus, P_1 , was made to vary between 750 MPa and 7500 MPa corresponding to contact area ratios between 1 and 10%. The exponent m was treated as an adjustable parameter

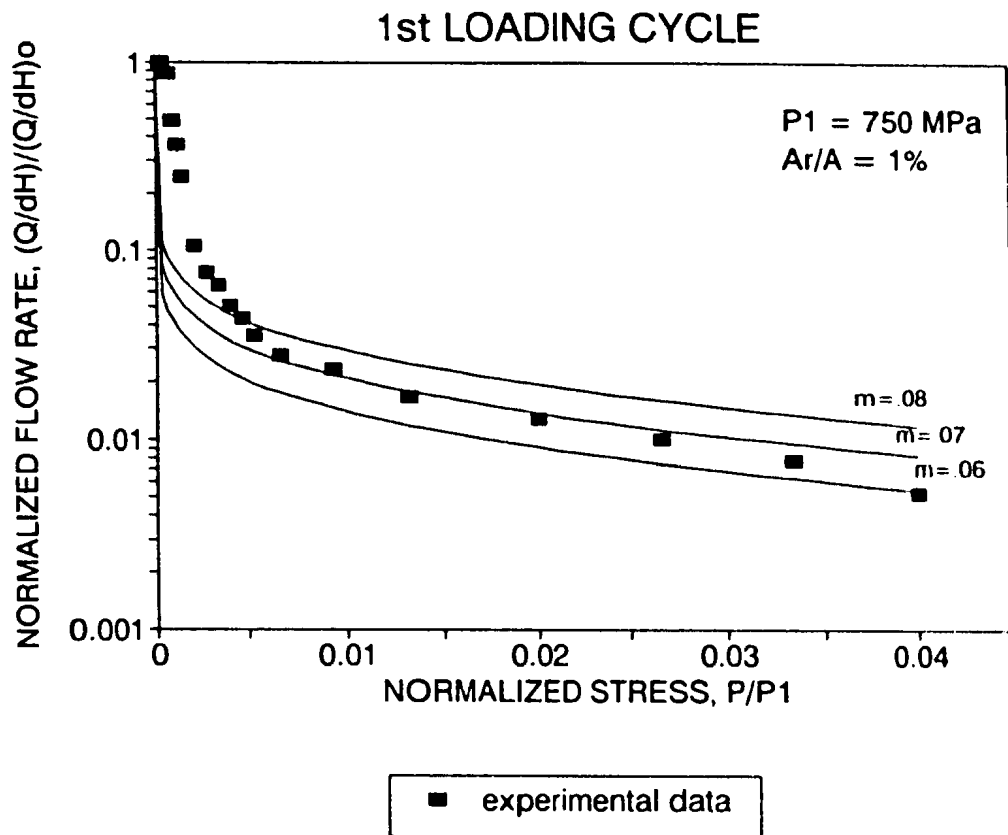


Figure 4.1 Comparison of Gangi (1978) model curves with stress-flow data from the first loading cycle ($P_1 = 750 \text{ MPa}$, $m = .06, .07, .08$).

fitting curve possible. Since the fracture was always under a seating load, a zero pressure flow rate was never measured and thus the flow rate measured at the lowest normal stress was used instead. This had no effect on the shape of the model curves but only on the magnitude of the value of m . For the first loading cycle, the closest fit occurred with P_1 equal to 750 MPa ($A_1/A = 1\%$) and m in the .06 to .08 range ($n = 12.5$ to 16.7). The model curve fits the experimental data at the high stress range reasonably well but underestimates the flow rate at low normal stresses. A slightly better fit was obtained using a lower P_1 value but this would require using an unreasonably low A_1/A ratio or a much lower Young's modulus.

Theoretical curves were also compared with data from the second, third and fourth (final) loading cycles to determine if an improved fit could be obtained with increasing number of loading cycles. A wide range of P_1 and m values were used in equation (4-1), but a good agreement with the experimental data could not be obtained. The comparison with data for the final loading cycle is shown in Figure 4.2. In this case, the best possible fit occurred with P_1 equal to 7500 MPa ($A_1/A = 10\%$) and m between .04 and .06 ($n = 16.7$ to 25). In this sense the model is correct in requiring a higher contact area ratio with increased number of loading cycles as some of the taller asperities would be broken off and more asperities would contact each other as mating of the two surfaces is improved. Increasing the value of P_1 has the effect of flattening out the model curves which is the same behaviour observed for the measured flow rates with each successive load cycle (see Figure 3.2).

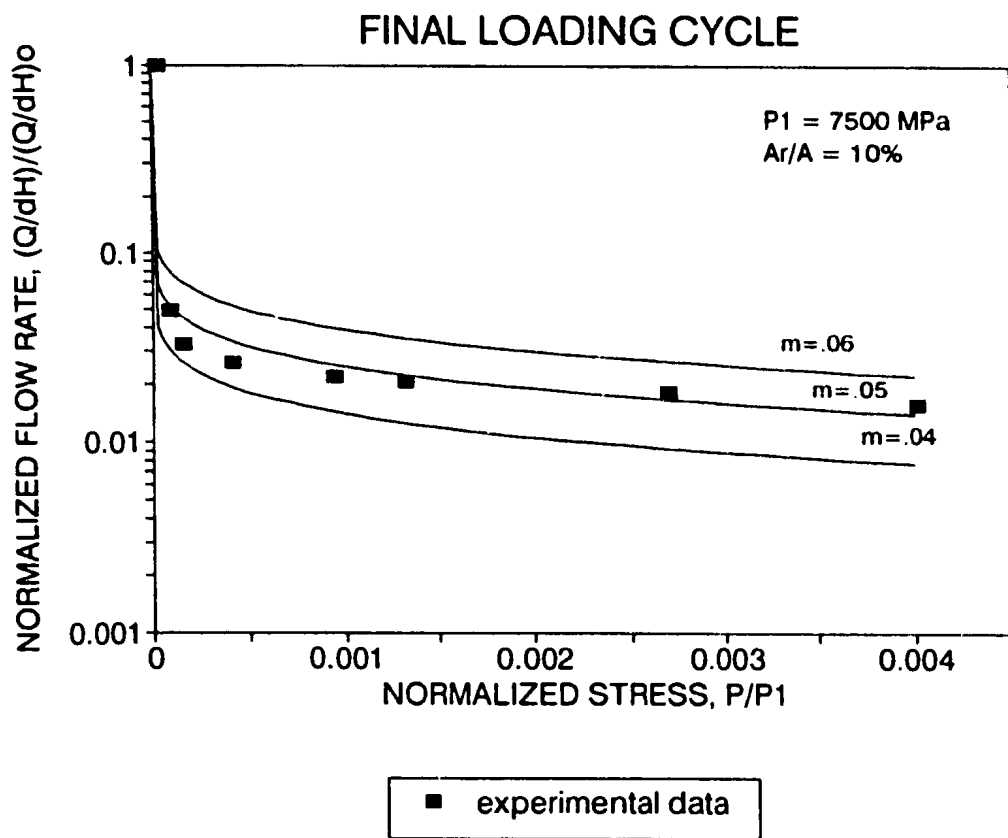


Figure 4.2 Comparison of Gangi (1978) model curves with stress-flow data from the final loading cycle ($P_1 = 7500 \text{ MPa}$, $m = .04, .05, .06$).

To summarize, input for the Gangi model includes a measurement of the fracture permeability at zero normal stress, the Young's modulus for the rock, an estimate of the contact area and a power law distribution of asperity heights. Forward application of the model is difficult and in fact the exponent m , and to a certain extent P_1 , are treated as adjustable parameters until a reasonable fit is found for the experimental data. For the natural granite fracture tested in this study, a good agreement could not be obtained. Other workers attempting to apply the Gangi model (Brar and Stesky, 1980; Tsang and Witherspoon, 1981; Elliott et al., 1985) have also had difficulty with its use.

A fundamental problem with the model appears to be that it fails to account for increasing contact area with increasing stress. It assumes that only a few tall asperities make contact and that these deform when the fracture is closed without changing the contact area ratio. Thus if the contact area remains the same, the effective modulus P_1 is constant and is only a small percentage of the Young's modulus for the intact rock. However, if the contact area increases significantly with increasing stress, P_1 should also increase and approach the Young's modulus at high normal stresses. This and other studies (Gale, 1987; Pyrak-Nolte et al., 1987) have shown that contact areas for granite fractures increase from about 5% at 1 MPa to 17% at 10 MPa and as high as 42% at 33 MPa. An attempt was made to improve the fit of the model by including a variable P_1 which assumes that the contact area

changes in proportion to the change in fracture stiffness. The resulting curves did not show any agreement with the experimental data however.

4.2 The Walsh Normal Closure - Conductivity Model

A theoretical model for the normal closure behaviour of rock fractures was presented by Walsh and Grosenbaugh (1979) that combined compressibility theory for fractured rock with elastic deformation theory used in mechanics for contacting surfaces. Using the elastic contact model of Greenwood and Williamson (1966) for the contact of rough surfaces, the relationship between normal closure and applied stress was shown to be strongly dependent on the topography of the fracture surfaces. The tips of the asperities were modelled as spheres with the same radius of curvature and heights that varied according to a specified distribution function. They showed that using an exponential distribution of asperity heights enabled the relationship between applied stress, P , and the deformation, δ , of each fracture surface to be expressed simply as

$$\frac{dP}{d\delta} = \frac{P}{h} \quad (4-2)$$

where h is the standard deviation of the asperity heights. A similar empirical relationship was found by Goodman (1976) from tests on mated and unmated artificial fractures but no physical meaning of the two constants in his equation was

given. Walsh and Grosenbaugh suggest that h not only gives an indication of roughness of the fracture surface but is also related to the local separation between the two surfaces. In this context, h is in fact one-half the standard deviation of the aperture distribution.

According to the theory, fracture stiffness, $dP/d\delta$, should be a linear function of normal stress with a slope equal to $1/h$. Walsh and Grosenbaugh showed that fracture stiffness measurements for an in-situ experiment by Pratt et al. (1977) did follow a linear relationship with applied stress. The slope of the curve suggested that h for that fracture was approximately $80\ \mu\text{m}$. Normal stiffnesses for this study were obtained from the slope of the fracture closure curves in Figure 3.1 and have been plotted against normal stress in Figure 4.3. The resulting curves are approximately linear over the lower stress range but tend to level off at stresses greater than 15 - 20 MPa. Stiffness is also observed to increase with each subsequent loading cycle as more and more asperities come into contact and permanent deformation takes place. The decline in the rate at which stiffness increases with stress after 15 - 20 MPa suggests that fracture stiffness is not linear over a higher stress range. Other studies of natural fractures (Bandis et al., 1983; Pyrak-Nolte et al., 1987) have also determined that the normal stiffness to normal stress relationship is nonlinear.

The solid line in Figure 4.3 represents the predicted stiffness of the fracture using the measured standard deviation of $74\ \mu\text{m}$ for small-scale roughness asperity heights in Table 3.3 (top surface). The theory predicts stiffnesses that are lower than

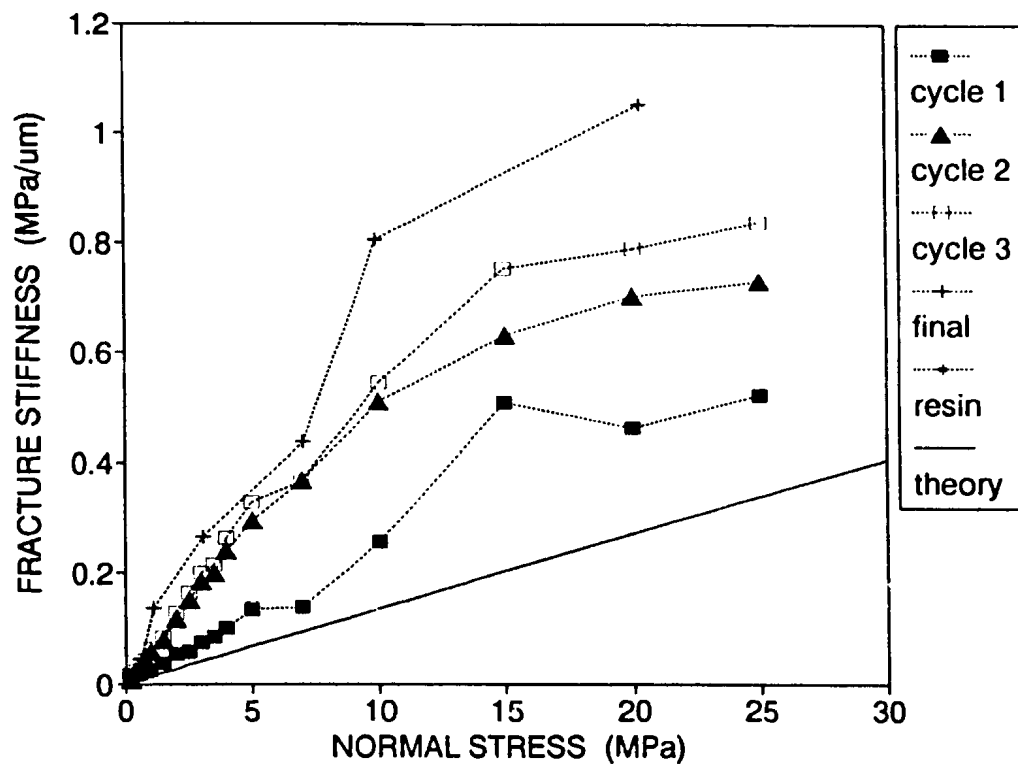


Figure 4.3 Normal fracture stiffness as a function of normal stress following the Walsh and Grosenbaugh (1979) model (cycle 1, 2 and 3 data from Gale & Raven, 1980).

the actual values. If the stiffness curves in Figure 4.3 are assumed to be roughly linear over the entire 0 - 30 MPa stress range, the slopes of best-fit lines to the measured data using linear regression analysis indicate h values in the range of 14 μm to 43 μm as given in Table 4.1. The correlation coefficient, R^2 , provides a relative comparison of how well the straight lines fit the data with a value of 1.0 indicating a perfect fit. If we consider stiffness to be linear only over the 0 - 15 MPa

Table 4.1 Predicted standard deviation of asperity heights, h , from normal stiffness vs. normal stress curve (after Walsh and Grosenbaugh, 1979).

Cycle	0 - 30 MPa		0 - 15 MPa	
	R^2	$h(\mu\text{m})$	R^2	$h(\mu\text{m})$
1st	.942	43	.955	33
2nd	.927	31	.972	23
3rd	.936	27	.987	20
Final	.934	19	.965	13
Resin	.998	14	--	--

stress range we obtain a better fit to the data but lower values of h ranging from 13 μm to 33 μm . The h values in Table 4.1 are lower than the measured standard deviation of asperity heights (small-scale roughness) by a factor of 2 to 6. If the standard deviation of large-scale roughness (Table 3.2) is considered, the estimation

is more than an order of magnitude lower. Standard deviations of asperity heights for granitic fractures reported elsewhere in the literature (Swan, 1981; Brown, 1984; Thorpe, 1986; Gale, 1987; Gentier, 1990a) are in the 200 - 3000 μm range.

Judging from these results we see that the theory underestimates the roughness and apertures of natural fractures. Obviously, there are bound to be some problems with using a theoretical asperity height distribution for real surfaces that each have a unique distribution of their own. Walsh and Grosenbaugh have suggested that the exponential model is a good approximation for most fracture surfaces but our results and those of others (Swan, 1983; Brown, 1984; Wong et al., 1989) indicate that this is probably a poor assumption to make.

Walsh (1981) found that the Walsh and Grosenbaugh normal closure model was suited for studying fluid flow in fractures since it modelled the changes in both aperture and contact area. He used an analogy between heat flow in a sheet containing cylindrical inclusions of zero conductivity and fluid flow in a planar fracture with points of contact to show how contact area affects the conductivity of a fracture with an otherwise unhindered flow path. He then combined aperture and contact area relations deduced from the Walsh and Grosenbaugh model to derive an expression relating fracture conductivity, K , to applied stress, P , of the form

$$K/K_0 = [1 - \sqrt{2}(h/a_0)\ln(P/P_0)]^3 \quad (4-3)$$

where K_0 and a_0 are the fracture conductivity and half-aperture at some reference stress P_0 , and h is the standard deviation of the asperity height distribution.

Equation (4-3) implies that the cube-root of fracture conductivity should be linearly related to the logarithm of applied stress. The slope of the line, h/a_0 , can be used to infer the roughness of the fracture surface or be used to predict fracture conductivity if roughness measurements have been made. Walsh compared the results from experiments on artificial fractures by other workers (Jones, 1975; Kranz et al., 1979; Brar and Stesky, 1980) and found good agreement with his theoretical relationship for normal stresses up to 200 MPa.

The hydraulic conductivities for each of the loading cycles in this study have been calculated using equation (1-1) and their cube-roots plotted against the logarithm of normal stress in Figure 4.4. This involved making the assumption that the cubic law could be used to determine the hydraulic apertures. The resulting curves show a linear decrease at lower stresses but then they decrease at a faster rate after about 10 MPa. This indicates that Walsh's theoretical relationship does not seem to hold at higher normal stresses which was the same observation made for the stiffness behaviour in Figure 4.3. This finding is consistent with the shortcomings of the cubic law which has also been proven not to be applicable at high normal stresses. The slope, h/a_0 , of the resin loading curve in Figure 4.4 is equal to 0.80. Using a calculated hydraulic aperture of about 10 μm at a reference stress of 1 MPa infers a r.m.s. asperity height, h , equal to 8 μm . This is similar to the h value of

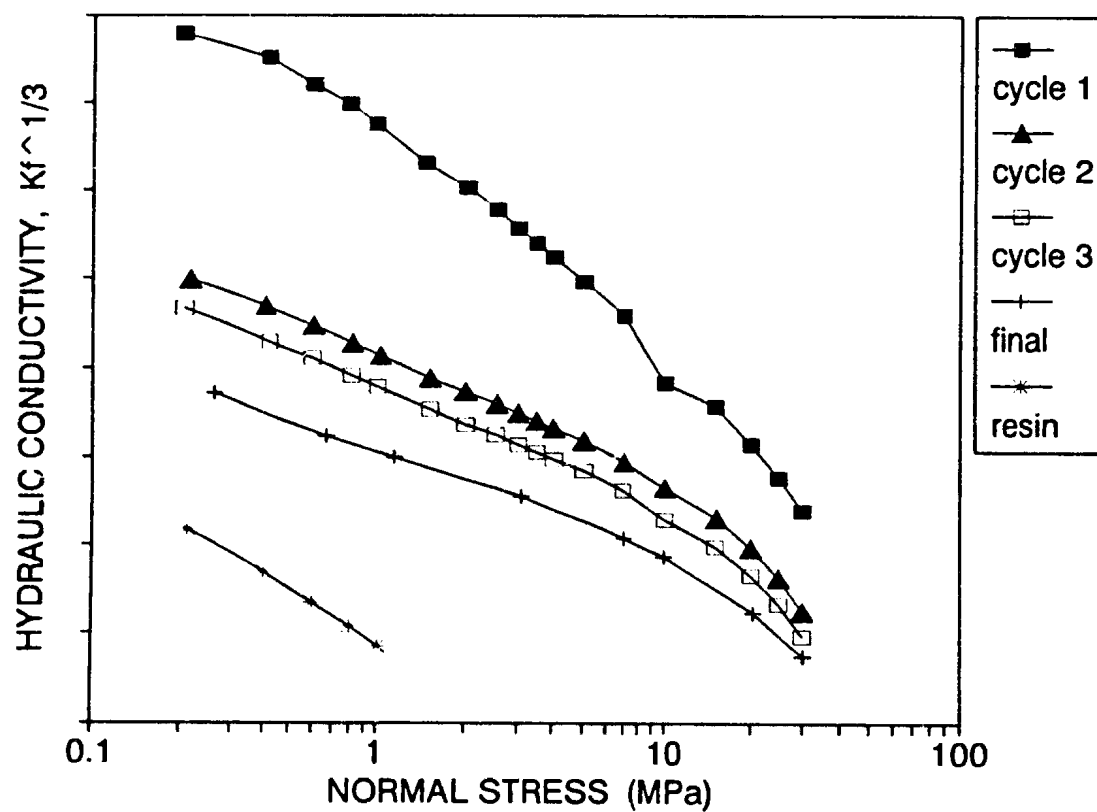


Figure 4.4 Plot of cube-root of hydraulic conductivity vs. logarithm of normal stress following the Walsh (1981) model (cycle 1, 2 and 3 data from Gale and Raven, 1980).

13 μm obtained from the normal stiffness curve for the resin cycle but is much lower than the measured standard deviation of asperity heights and clearly unrealistic for a natural fracture in granite.

A more general evaluation of usefulness of the Walsh model for predicting fracture flow as a function of normal stress was made by comparing model generated curves with measured flow rates expressed in terms of flow per unit head. Hydraulic conductivity in equation (4-3) was replaced by normalized flow rate, $Q/\Delta H$, and h/a_0 was treated as an adjustable parameter to give the best possible fit to the measured data. The model was compared with flow rate data for the first, second, third, final and resin loading cycles using reference stresses of 1 MPa, 10 MPa and 30 MPa. In general, the model had difficulty in predicting flow rates at the lowest normal stresses but a reasonably good fit was obtained for the rest of the data for each load cycle.

Examples of model comparisons for the second and final loading cycles are given in Figure 4.5(a) and (b) for reference stresses of 30 MPa and 10 MPa respectively. For these two cases we see that the Walsh model provides a good fit to the measured data except at very low stress. A summary of the h/a_0 values used in fitting the Walsh model to measured flow rates is provided in Table 4.2. The h/a_0 parameter was found to decrease with each loading cycle and approach a constant value for the final and resin cycles. For the first two cycles h/a_0 increased with increasing reference stress but thereafter remained constant for each stress level. Physically, to obtain the low h/a_0 values observed for the final and resin loading

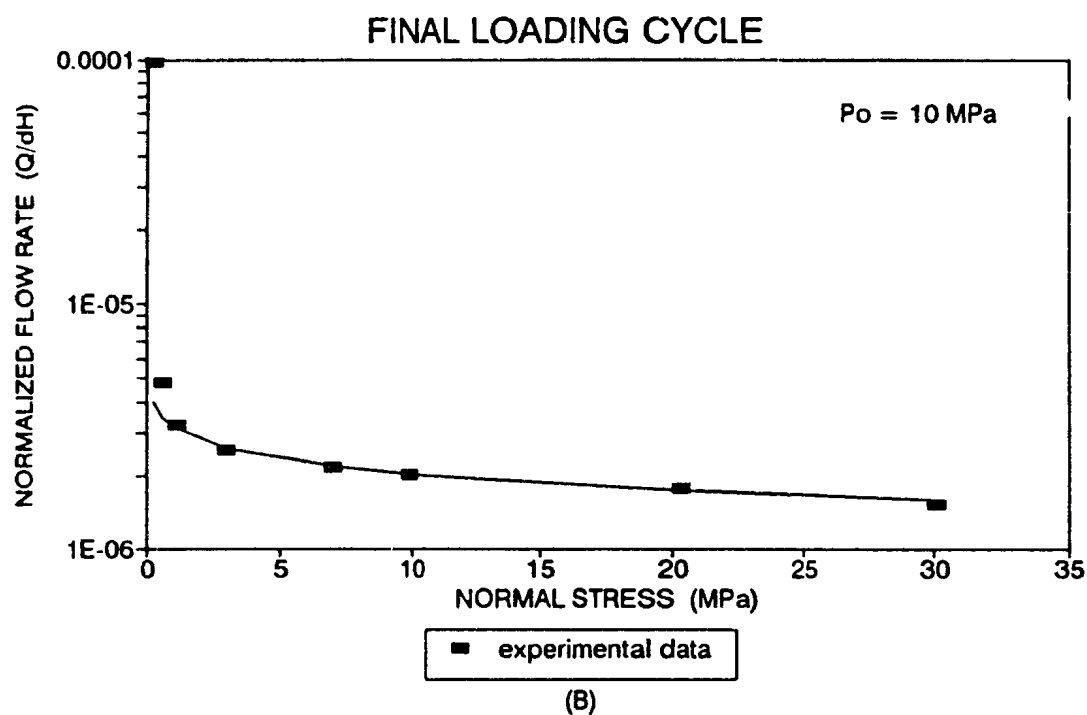
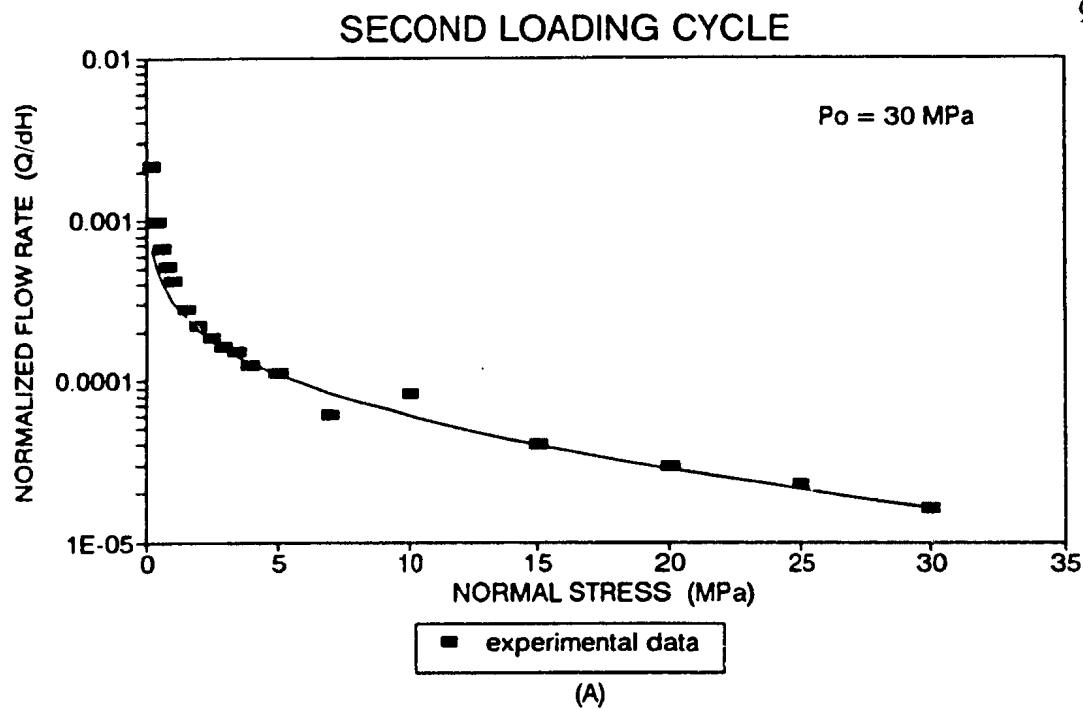


Figure 4.5 Comparison of the Walsh (1981) model curve with stress-flow data from (a) the second loading cycle, $P_o = 30 \text{ MPa}$ and (b) the final loading cycle, $P_o = 10 \text{ MPa}$.

Table 4.2 Values of h/a_0 used in fitting the Walsh (1981) model to measured stress-flow data.

Cycle	h/a_0		
	1 MPa	10 MPa	30 MPa
1st	.15	.18	.30
2nd	.14	.28	.35
3rd	.12	.12	.12
Final	.05	.05	.05
Resin	.05	--	--

cycles would require apertures that are more than an order of magnitude greater than the r.m.s. asperity height. This is not likely for tight fractures that have undergone repeated loading where the r.m.s. asperity height is roughly the same or greater than the aperture. When h/a_0 measured from the resin work (.75) was used in the model, no agreement whatsoever could be found with the measured flow rates.

4.3 The Swan Normal Closure - Conductivity Model

Swan (1980, 1981) made one of the first attempts to evaluate normal deformation theory for rock fractures using actual surface roughness measurements. He took the elastic contact theory developed by Greenwood and Williamson (1966), Greenwood and Tripp (1971) and Walsh and Grosenbaugh (1979) and compared it with normal stiffness data from tests on induced fractures (mated and unmated) for

which he also made quantitative measurements of surface topography. He found that the analytical models showed qualitative agreement with the experimental data but consistently predicted stiffness behaviour that was up to an order of magnitude too low. This observation was attributed to the use of theoretical asperity height distributions and failure of the theory to model aperture effects.

For this reason he favoured the use of a discrete approach in which he used digitized roughness profiles obtained from the fractures he was testing to numerically simulate fracture closure. He also showed how stiffness behaviour depends on the initial aperture and thus the "matedness" of the fracture. The predictions from the discrete approach gave good approximations to his experimental results and led him to the conclusion that a simple linear relationship between fracture stiffness and applied stress was appropriate. He does caution however that for Hertzian contact theory to apply to fracture deformation studies in rock requires low nominal pressures. The normal stresses in his tests did not exceed 15 MPa.

From roughness measurements of numerous fractures in several different rock types, Swan (1983) showed how surface roughness characteristics could be used to predict fracture stiffness behaviour. He also extended this application to include changes in contact area and hydraulic conductivity with stress. For a series of ten slate fractures that were tested, he found that normal stiffness, true contact area and hydraulic conductivity were all simple functions of normal stress and initial aperture.

The proportionality suggested by Walsh and Grosenbaugh (1979) between normal stiffness and normal stress (equation 4-2), in which the slope of the stress-stiffness curve, σ_a is the estimated standard deviation of asperity heights, was verified. Furthermore, he found that there was an empirical relationship between σ_a and the initial aperture, e_0 such that

$$e_0 = 8.62 \sigma_a \quad (4-4)$$

Swan also showed that the theory predicts a linear relationship between normal stress and true contact area. He did not measure contact area in his experiments but found that it agreed qualitatively with the results reported by Iwai (1976). He suggested that the proportionality is valid provided that contact only occurs at a few of the higher asperities. This turns out to be a rather limiting assumption, as was the case with Gangi (1978), and is expected to hold only if the fracture is unmated and the normal stresses are low. Results from some recent studies (Pyrak-Nolte et al., 1987; Gentier, 1990a) have shown that contact area changes are nonlinear.

As far as hydraulic behaviour is concerned, Swan recognized that the normal deformation theory could be used to calculate apertures at different stress levels provided the initial aperture is known. Given the relationship between hydraulic conductivity and aperture, according to the parallel plate model, he predicted the dependency of hydraulic conductivity, K , on normal stress, P , to take the following log-linear form:

$$\sqrt{\alpha' K} - c - m(\ln P) \quad (4-5)$$

where K_0 is the initial hydraulic conductivity and c and m are constants. Swan presented some normalized hydraulic conductivity curves predicted from fracture surface roughness measurements that were approximately linear functions of normal stress. He did not make any flow measurements during his experiments and thus was not able to confirm these predictions with measured results.

In terms of the normal deformation theory presented by Walsh and Grosenbaugh (1979), equation (4-5) can be written as

$$\sqrt{K/K_0} - (1 - a/e_0) - (\sigma / e_0) \ln P \quad (4-6)$$

where a and σ_0 are obtained from the load-deformation curve and e_0 is the initial aperture. The fracture closure measurements for all five loading cycles from the stress-flow experiments are shown in the semi-log plot in Figure 4.6. As predicted by the theory, the results are highly linear over the complete stress range from 0 to 30 MPa. The data from the first loading cycle exhibits some anomalous behaviour as closure increases with increasing stress at a greater rate than the other loading cycles. This can probably be attributed to initial seating or mating of the two surfaces with applied load which would not occur with subsequent loading since the load was never completely removed. The slope and intercept data obtained by straight line fits to each curve is given in Table 4.3. The correlation coefficients are

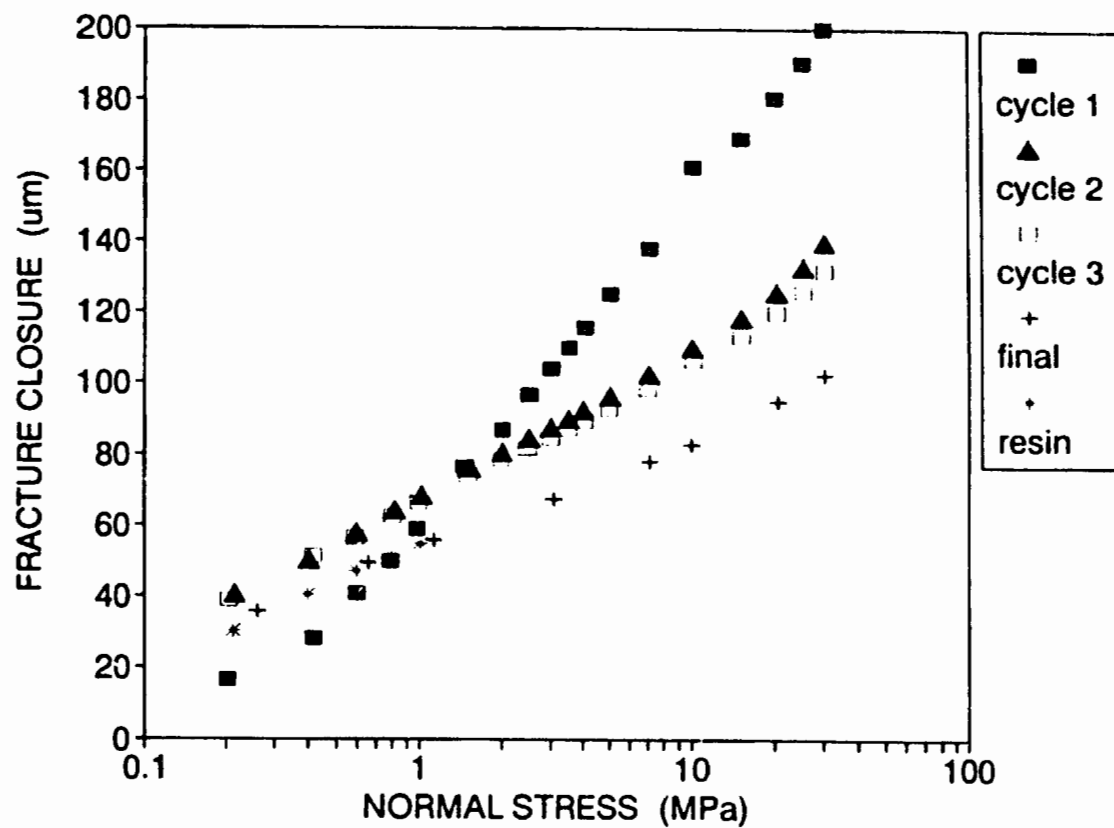


Figure 4.6 Fracture closure vs. logarithm of normal stress following the Swan (1983) model (cycle 1, 2 and 3 data from Gale and Raven, 1980).

all greater than 0.990 thus indicating strong linearity. According to the theory, the slope values, σ_e , should also give an estimate of the standard deviation of asperity heights. As discussed in the previous section, the estimated values are consistently lower than the measured values by at least half in the case of small-scale roughness and considerably more than that for large-scale roughness. Note that the σ_e values in Table 4.3 are very similar to the h values in Table 4.1.

Table 4.3 Parameters for the Swan (1983) model derived from linear regression analysis of stress-closure and stress-hydraulic conductivity curves.

Cycle	σ_e	δ_f vs. $\ln P$		\sqrt{K}/K_o vs. $\ln P$		R^2
		a	R^2	c	m	
1st	38.95	63.20	.992	.73	.16	.992
2nd	19.36	67.29	.994	.56	.13	.994
3rd	17.93	65.67	.996	.53	.13	.996
Final	13.46	53.46	.995	.51	.12	.995
Resin	15.72	54.65	.999	.12	.25	.999

Following the approach of Swan (1983), measured flow rates from our tests were converted to hydraulic conductivities using the parallel plate model and plotted in Figure 4.7 as normalized hydraulic conductivity versus the logarithm of normal stress. The results are linear as predicted by Swan with conductivity exhibiting a relatively constant decrease with increasing stress. Again, the first loading cycle displays slightly different behaviour than the others for the reasons described above.

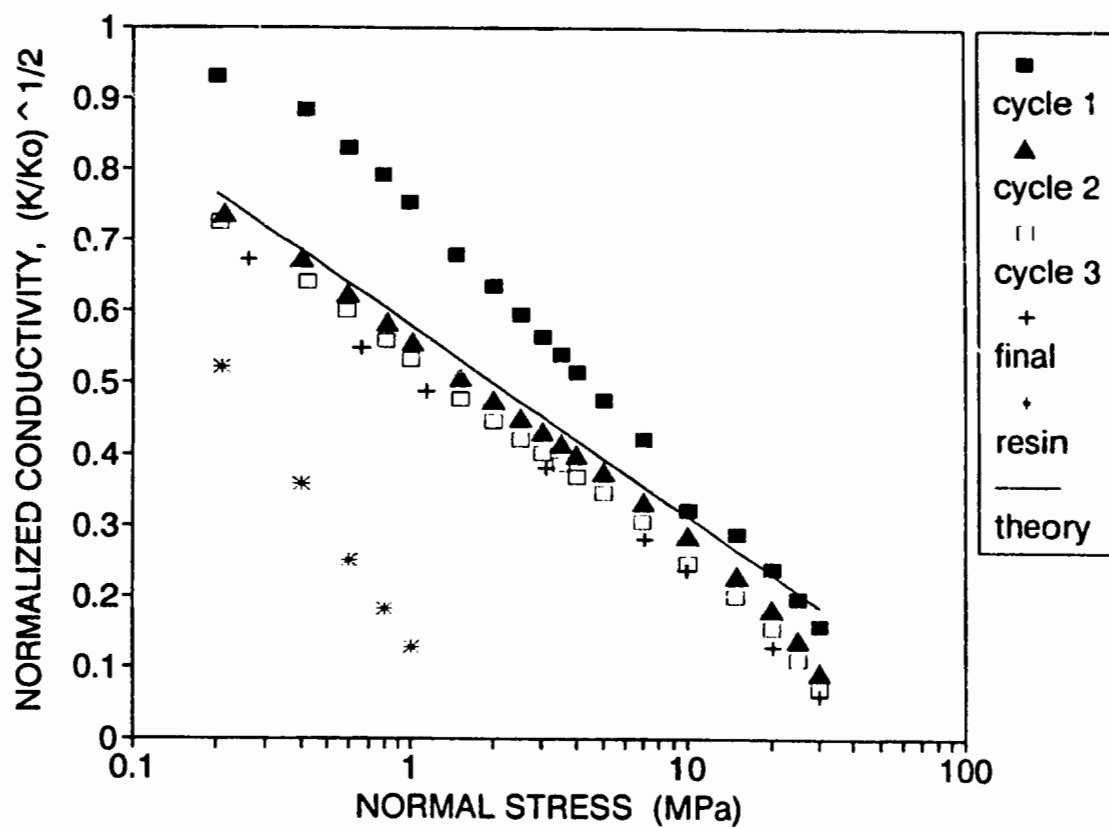


Figure 4.7 Normalized conductivity vs. logarithm of normal stress following the Swan (1983) model (cycle 1, 2 and 3 data from Gale and Raven, 1980).

The resin curve also shows anomalous behaviour but this is due to the method used to calculate the residual apertures for use in the parallel plate model (see Chapter 3). The residual apertures were calculated at 30 MPa for the first four load cycles but only at 1 MPa for the resin cycle thus causing the observed discrepancy.

Straight lines were fitted to each curve using linear regression and the slopes and intercepts, which are the m and c constants in equation (4-5), were computed. These values along with the correlation coefficients are given in Table 4.3. Also shown in Figure 4.7 is the predicted curve using equations (4-4) and (4-6) and the average a and σ_e values from the second, third and final loading cycles in Table 4.3. The predicted curve gives a good approximation of the calculated hydraulic conductivities and was derived from fracture closure measurements and an estimate of the initial aperture. The initial aperture estimated from equation (4-4) is 143 μm while the average calculated initial aperture from the parallel plate model was 159 μm .

To avoid using the parallel plate model, hydraulic conductivity in equation (4-6) was replaced by normalized flow rate, $Q/\Delta H$. The resulting comparisons of predicted flow rates with measured flow rates showed some qualitative agreement but in general equation (4-6) did not prove to be a good modelling tool. Some improvements to the fit with experimental data could be made by treating σ_e and e_o as adjustable parameters. For example, Figure 4.8 shows the predicted and measured flow rates for the second loading cycle. The predicted curve modelled the actual

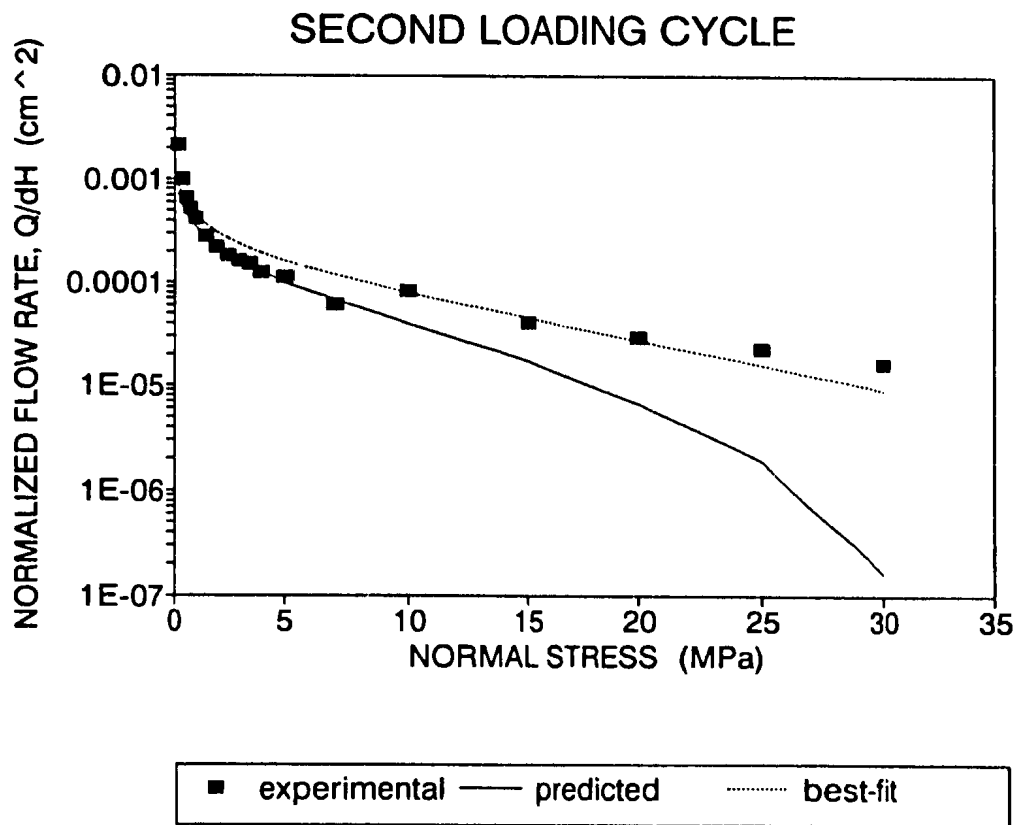


Figure 4.8 Comparison of the Swan (1983) model predicted curves with measured stress-flow data from the second loading cycle.

data quite well over the lower stress range but then tailed off at higher stresses. By changing σ_c by $2 \mu\text{m}$ from 19 to $17 \mu\text{m}$, a much better fit was obtained. If σ_c is supposed to represent the r.m.s. asperity height, we see that flow rates are quite sensitive to small changes in surface roughness. This is contrary to Swan's conclusion that surface roughness differences had little or no effect on the properties of the fractures he tested. The type of fracture he was using (cleavage planes in slate) and their unmated condition would explain the reduced role of surface roughness in this case. This apparent contradiction raises the question of the differences between the behaviour of mated and unmated fractures.

4.4 The Tsang and Witherspoon Void/Asperity Model

To properly model the stress - flow behaviour of fractures under increasing normal stress, Tsang and Witherspoon (1981) recognized that the traditional parallel plate approach of representing a fracture as two, smooth parallel surfaces had to be modified to account for fracture surface roughness. This was done previously (Witherspoon et al., 1980) by including an empirically determined correction factor in the cubic law model relating fracture flow rate to fracture aperture. However, that approach gave no insight into the actual physical processes involved for flow in a rough-walled fracture. Since roughness imparts a variable fracture aperture, they suggested that instead of using a single value for fracture aperture that it would be

more appropriate to use a statistical average aperture derived from the actual roughness of the fracture surfaces.

In their proposed model, a rough fracture was conceptualized as a series of voids between contacting asperities. The fracture can be treated as either a collection of voids or a distribution of asperities. Fracture closure under increasing normal stress was attributed to the deformation of the voids, not elastic compression of asperities as has been the approach used in the other theoretical models discussed thus far. As the size of the voids decreases under stress, more asperities on opposite sides of the fracture come into contact with each other, changing the aperture distribution and controlling the movement of fluids through the fracture plane. Thus the mechanical behaviour was described by a void model and the hydraulic behaviour by an asperity model, both being linked through a geometrical characterization of fracture roughness. The key to the model is that it leads to a mathematical aperture distribution function for different values of normal stress. This enables the computation of a statistical average aperture which can be used in a modified cubic law for determining fracture flow rates. The required input for the model includes stress-deformation measurements of both the fractured and intact rock and an estimate of the contact area at a specified normal stress.

Tsang and Witherspoon (1981) showed that analytical functions fitted to normal stress - deformation measurements for intact and fractured rock could be used to determine the Young's modulus and effective Young's modulus respectively

for different normal stresses. The ratio of the two moduli was shown to be related to the average length of the voids making up the fracture. As the fracture closes under applied stress, the average void length decreases and the number of areas of contact increases. The asperities-in-contact function was then plotted against fracture deformation and another analytical function was fitted to the data. This was used to obtain the asperity distribution function which also gives the aperture distribution function since they are related. Knowing the aperture distribution function enabled them to compute the statistical average aperture, $\langle b^3 \rangle$, as a function of fracture deformation, ΔV , and normal stress, σ , as follows:

$$\langle b^3(\Delta V, \sigma) \rangle = \frac{\int_0^{b_0 - \Delta V} (b_0 - \Delta V - h)^3 n(h) dh}{\int_0^{b_0} n(h) dh} \quad (4-7)$$

where b_0 is the maximum aperture of the fracture at zero stress and $n(h)dh$ is the asperity height distribution function. The value for b_0 can be obtained from an estimate of the fractional contact area for the fracture walls at a specified stress. Once $\langle b^3 \rangle$ is calculated, fracture flow as a function of normal stress can be determined from equation (1-3). The theory showed good agreement with the experimental data of Iwai (1976) for tension fractures in granite and basalt with contact area ratios between 10% and 20%.

An attempt was made to compare the Tsang and Witherspoon theory with the stress - flow data obtained from the final loading cycle in these experiments. First, analytic functions were fitted to the deformation measurements for the fracture and intact rock as shown in Figure 4.9. Note the nonlinear behaviour of the fracture deformation in the low stress range and how it becomes more linear and parallel to the rock deformation at higher stresses. The analytic functions were obtained from the use of a FORTRAN program called LEASQR (Gerald and Wheatley, 1984, p.561) for fitting polynomial equations to nonlinear data using the least squares method. The derivatives of these functions were used to calculate the Young's modulus for the rock and effective Young's modulus for the fracture which could then be used to determine the relative average void length at each stress. This facilitated the determination of the relative number of asperities in contact for various stresses and fracture deformations.

Next, the number of asperities in contact were plotted against fracture deformation as shown in Figure 4.10 and another best-fit analytic function was obtained using the LEASQR program. The waviness in the analytic function is caused by an observed fluctuation in rock deformation measurements during the initial stages of closure which permeated through all the calculations leading up to the asperities-in-contact function. The derivative of this function was used to determine the asperity height distribution function, $n(h) dh$. Having obtained $n(h) dh$ enables the statistical average aperture to be computed using equation (4-7). The

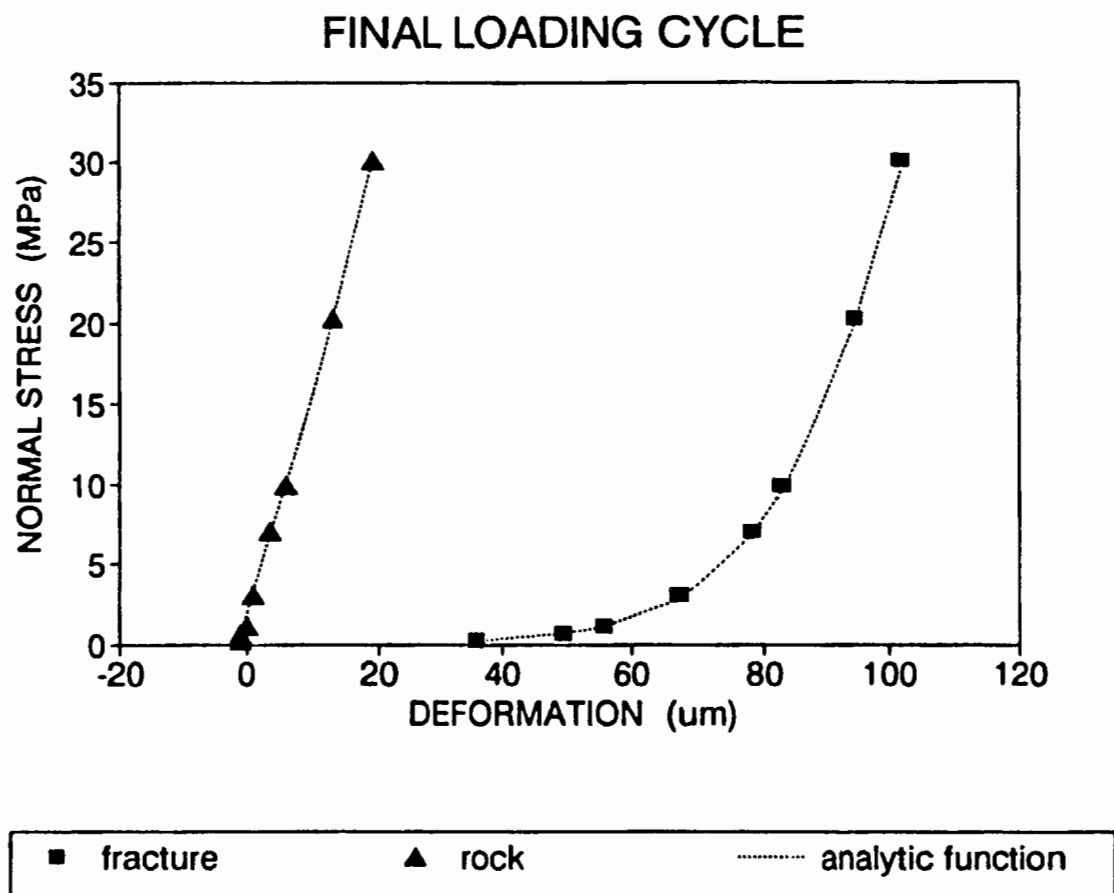


Figure 4.9 Analytic functions fitted to intact rock and fracture deformation measurements from the final loading cycle following the Tsang and Witherspoon (1981) model.

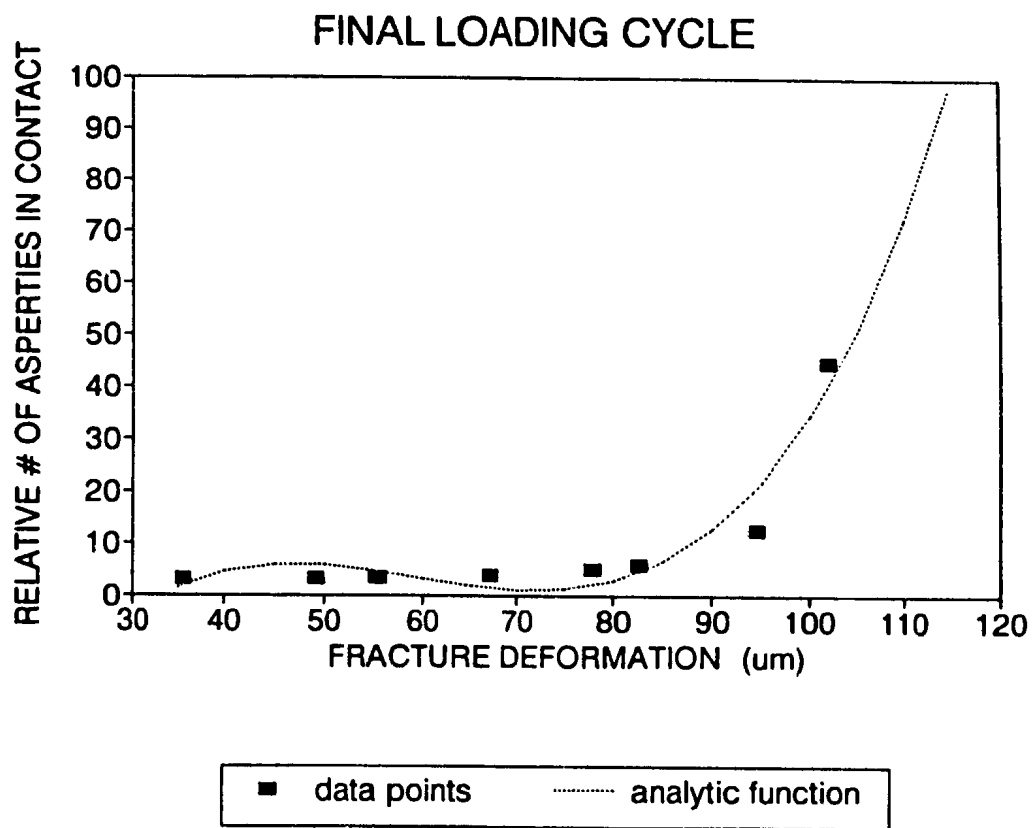


Figure 4.10 The 'asperities in contact' function for the final loading cycle following the Tsang and Witherspoon (1981) model.

measured contact area ratio of 5% at 1 MPa (Chapter 3) was used to estimate the maximum fracture aperture, b_0 , in equation (4-7). This yielded a b_0 value of 114 μm which compares favourably with the measured maximum fracture deformation of 102 μm . Using standard numerical integration techniques, the integrals in equation (4-7) were evaluated and the values of $\langle b^3 \rangle$ were substituted into the cubic law expression (equation 1-3) to obtain fracture flow as a function of normal stress. The results however, shown in Figure 4.11, do not agree with the measured flow rates as the predicted flow rates are generally two orders of magnitude higher except at the highest stresses. Assuming the contact area to be between 10% and 20% at 20 MPa, as was found by Iwai (1976) for granite fractures, did not improve the fit. The theoretical curve for a contact area of 15% at 20 MPa is shown in Figure 4.11.

These results indicate that the Tsang and Witherspoon model is not valid for natural fractures that have undergone several loading cycles. The poor agreement between experiment and theory in this case is not surprising since the governing equation in their model is only a modified version of the cubic law. While a statistical averaging of the variation in aperture is more appropriate for real fractures, the model still assumes that fracture flow is simply related to the cube of the aperture. The statistically averaged apertures were not much different than the calculated hydraulic apertures in Table 3.1 which were shown not to give good predictions of measured flow rates using the cubic relationship. The lack of agreement tends to worsen with increasing stress and increasing number of loading

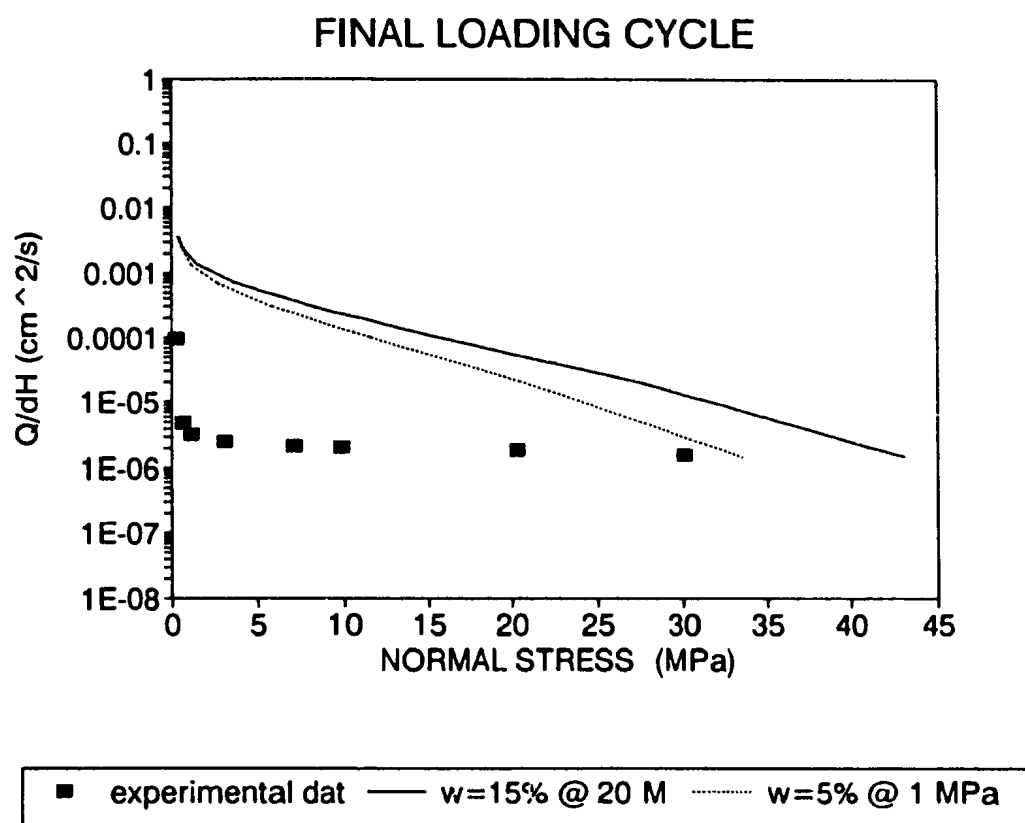


Figure 4.11 Comparison of the Tsang and Witherspoon (1981) model predicted curves with measured stress-flow data for the final loading cycle.

cycles. It was expected that the model would give a better comparison with the first or second loading cycles, however, difficulty was encountered in applying the model due to problems with the measurement of the intact rock deformations as reported by Raven and Gale (1985). As has already been shown, the modelling technique is very sensitive to the measured rock deformations and thus the results obtained were not realistic and could not be compared with the final loading cycle.

The discrepancy between the measured data and the theoretical predictions in Figure 4.11 can probably be attributed to tortuosity effects which are not included in the Tsang and Witherspoon model. Tsang and Witherspoon (1985) have shown that when the aperture distribution is dominated by small apertures and the contact area of the fracture surfaces is above 30% that the effects of tortuosity may lower flow rates by two or three orders of magnitude from that predicted by the cubic law representation. The measured aperture distribution for the fracture in this study, Figure 3.18, is indeed highly skewed towards small apertures. The aperture contour plot in Figure 3.23 shows the effect that tortuosity has in producing irregular flow channels across the fracture plane. Despite some of these shortcomings, the model still has some usefulness in showing the qualitative relationships between fracture roughness and observed mechanical and hydraulic behaviour. Tsang and Witherspoon (1983) have shown the versatility of the model in that it can be used to estimate the stress-deformation and fluid flow behaviour when the roughness

characteristics of the fracture are known or conversely to estimate the fracture roughness from an examination of the stress-closure and stress-flow data.

4.5 The Barton-Bandis Empirical Model

Barton and Bakhtar (1983) and Barton et al. (1985) describe a fully coupled stress-deformation-conductivity model derived from the results of literally hundreds of tests on natural fractures in a variety of rock types. The observed mechanical and hydraulic properties of fractures under both shear and normal stresses were found to be dependent on surface characteristics such as roughness and wall strength. Two parameters, namely the joint roughness coefficient (JRC) and the joint wall compression strength (JCS), form the basic input data for predicting shear stress-displacement behaviour and normal stress-closure behaviour. If an estimate of the initial fracture aperture is known, aperture changes can also be predicted which can then be related to conductivity changes as a function of applied stress. The key to the model is that the necessary input data can be obtained from a few simple index tests on pieces of intact and fractured core specimens from the rock in question.

Normal stress-closure modelling is based on the following hyperbolic model for loading and unloading found by Bandis et al. (1983) to give an excellent fit to an extensive set of experimental fracture closure data:

$$\sigma_n = \frac{\Delta V_j}{a - b\Delta V_j} \quad (4-8)$$

where ΔV_j is fracture closure and a and b are constants. Equation (4-8) is similar to the empirical expressions presented by Goodman (1976) for nonlinear normal closure behaviour but offers a better fit to the full range of data. It is shown that the asymptote to the hyperbola (a/b) equals the maximum fracture closure, V_m , while the constant a is equal to the reciprocal of the initial normal stiffness, K_{ni} . Bandis et al. (1983) present empirical relationships for V_m and K_{ni} that are functions of JRC, JCS and initial aperture, a_j , thus enabling the determination of the constants in equation (4-8) and fracture closure as a function of normal stress. One important finding from their work is that for the case of mated fractures, normal stiffness is not a linear function of normal stress as was suggested by Walsh and Grosenbaugh (1979) and Swan (1981, 1983).

In coupling normal closure behaviour with fracture permeability, Barton and Bandis make the distinction between the real mechanical aperture and the theoretical conducting aperture. They argue that the actual measured aperture, E , is not the same as the equivalent conducting aperture, e , used in the cubic law, except for extremely smooth fracture surfaces or very wide apertures. The mismatch between the two apertures, which is most pronounced at high stresses, was attributed to flow losses caused by tortuosity and surface roughness. From experimental data on E/e

ratios, they were able to derive a series of curves that showed the dependence of E/e on roughness and aperture. This leads to an equation relating mechanical aperture, E , and conducting aperture, e , of the form

$$e = E^2 / JRC^{2.5} \quad (4-9)$$

which is only valid for $E \geq e$. Since E at each stress level can be computed by subtracting the normal closure from the initial aperture, equation (4-9) provides the means for converting mechanical apertures (E) to conducting apertures (e) used in calculating fracture permeability ($k = e^2/12$). In the following discussion, the method for characterizing the Charcoal Grey granite fracture tested in this study is described and model predicted curves are compared with measured normal stress-closure-flow data.

The complete normal stress-closure-permeability behaviour of fractures can be predicted from three basic input parameters; the joint roughness coefficient (JRC), the joint wall compression strength (JCS) and the unconfined compression strength (σ_c). These parameters are determined from Schmidt hammer tests on the unweathered, intact rock and the weathered fracture surface, and, from tilt tests of both intact and fractured rock cores. Firstly, the JCS is determined by the following equation:

$$\log_{10} JCS = .00088 \gamma r + 1.01 \quad (4-10)$$

where γ is the rock density and r is the Schmidt hammer rebound number for the fracture surface. For the Charcoal Grey granite, a measured density of 26.83 KN/m^3 and an average Schmidt hammer rebound number of 45.2 yielded a value of 119.45 MPa for the JCS using equation (4-10). Secondly, the JRC is obtained from the relationship:

$$JRC = \frac{\alpha - \phi_r}{\log_{10}(JCS/\sigma'_{no})} \quad (4-11)$$

where α is the tilt angle at which the top half of a fractured core specimen begins to slide, ϕ_r is the residual friction angle determined from a tilt test using two intact rock cores and Schmidt hammer rebound tests on both the fracture surface and on intact rock, and σ'_{no} is the effective normal stress acting across the fracture when sliding occurs (under self-weight conditions). From tilt tests using a fractured core sample from the Charcoal Grey granite, sliding of the top half took place at an average angle of 62.5° . The basic friction angle, determined from tilt tests using two smooth pieces of core, was found to be 28.6° which leads to a residual friction angle of 21.7° . The effective normal stress on the fracture at sliding was determined to be 0.001 MPa. Using equation (4-11), the JRC was found to be 8.03 which is about medium roughness on a scale of 1 to 20.

As mentioned earlier, the coupling of normal closure and permeability using equation (4-9) requires an estimate of the initial fracture aperture, a_j . If these

measurements are lacking, an empirical equation has been derived for estimating a_j as follows:

$$a_j = \frac{JRC}{5} \left(0.2 \frac{\sigma_c}{JCS} - 0.1 \right) \quad (4-12)$$

The unconfined compression strength, σ_c , can be determined by substituting the Schmidt hammer rebound number, R , for the unweathered, intact rock into equation (4-10). Using an R value of 68.8 from Schmidt hammer tests on pieces of intact core gave a value for σ_c equal to 430.52 MPa. This was deemed to be unrealistically high for granite and a measured σ_c of 218.0 MPa from compression strength tests on the Charcoal Grey granite was used instead. Using the measured σ_c has little effect on the JCS and JRC calculations but does have a big effect on the initial aperture calculation (equation 4-12). The normal stress-closure-conductivity behaviour was modelled from the following input parameters:

$$JRC = 8.03$$

$$JCS = 119.45 \text{ MPa}$$

$$\sigma_c = 218.0 \text{ MPa}$$

In Figure 4.12, model-predicted normal closure curves for four loading-unloading cycles are compared with measured normal closure data from the laboratory tests. The experimental data shown is for the first, second, third and final loading cycles only. The model curve for the first cycle shows a very good

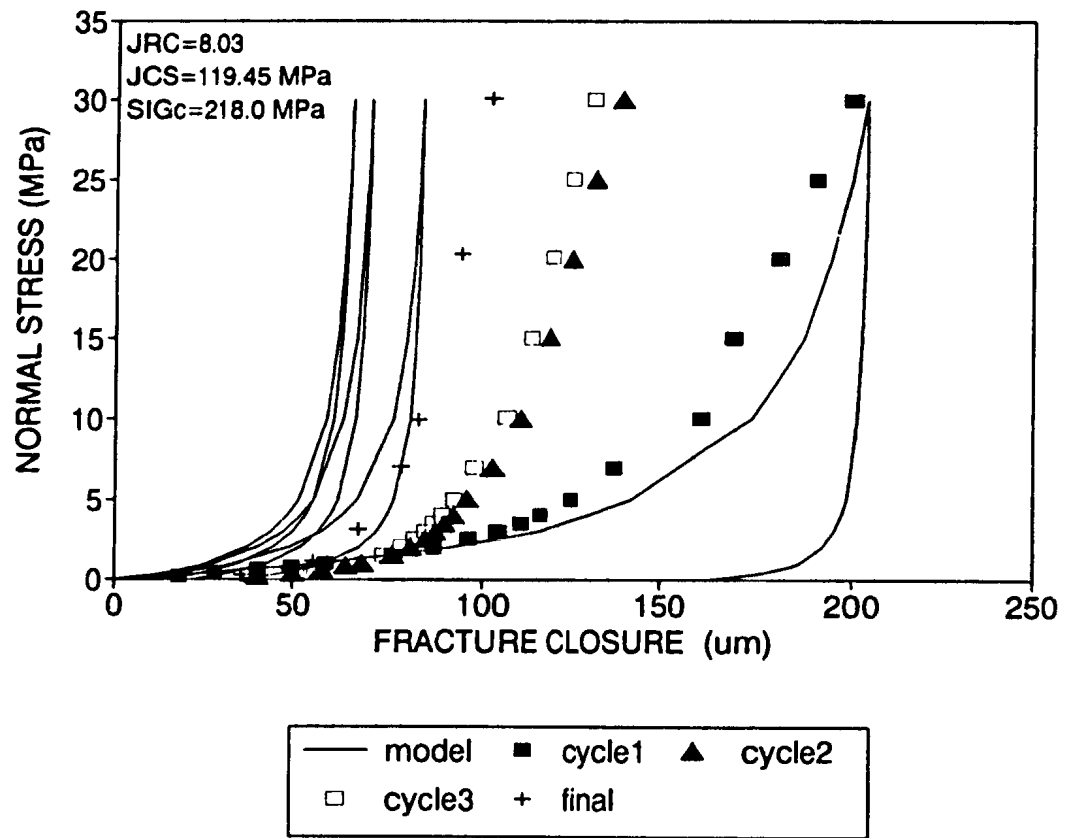


Figure 4.12 Comparison of the Barton-Bandis model curves for four loading cycles with measured stress - fracture closure data (cycle 1, 2 and 3 data from Gale and Raven, 1980).

approximation to the measured data and predicts a maximum fracture deformation of about $200 \mu\text{m}$. A large hysteresis is predicted between the first and second cycle and the model curves for the second, third and fourth cycles predict less deformation than was actually measured. The predicted maximum closure on the fourth cycle was $65 \mu\text{m}$ compared to the measured maximum closure on the final cycle of $102 \mu\text{m}$. The model curves do however correctly depict decreasing hysteresis between successive loading cycles and between the loading-unloading paths within each cycle.

Predicted flow rates using the Barton-Bandis model are compared with measured flow rates in Figure 4.13. In this figure, flow is expressed in terms of flow per unit head, $Q/\Delta H$, since fracture permeability or conductivity was not measured directly. The predicted flow rates were obtained by substituting the theoretical conducting apertures, e , calculated from equation (4-9) into the cubic law expression for flow, equation (1-3). Figure 4.13 shows that predicted flow rates are several orders of magnitude higher than the measured flow rates. One reason for this is due to the fact that the Barton-Bandis model predicted apertures that were larger than the actual apertures obtained from the resin studies. For example, the model aperture, e , at a normal stress of 1 MPa on the fourth unloading cycle was found to be $173 \mu\text{m}$. It should be closer to the mean aperture of $103 \mu\text{m}$ determined from the resin injection experiment at 1 MPa. The other reason is that the Barton-Bandis model uses the parallel plate model for relating aperture to flow rates and we have already seen that this approach does not appear to be valid for natural fractures

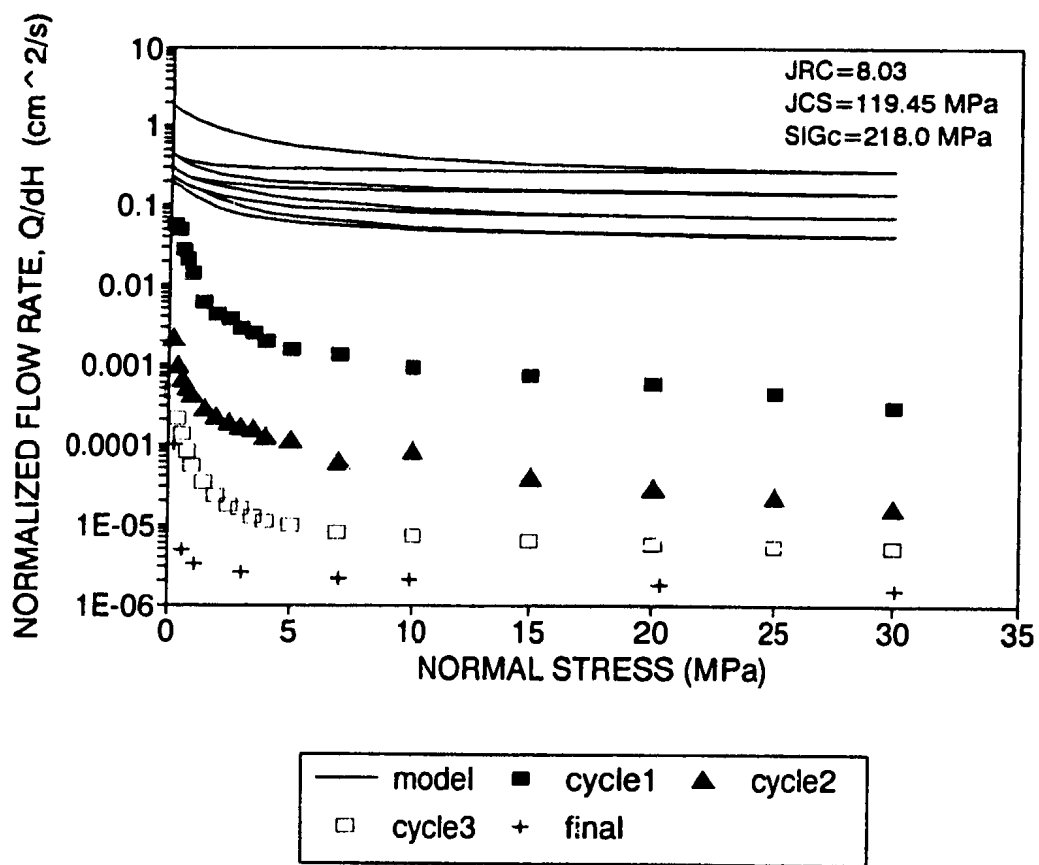


Figure 4.13 Comparison of the Barton-Bandis model curves for four loading cycles with measured fracture flow rate data (cycle 1, 2 and 3 data from Gale and Raven, 1980).

subjected to high normal stresses. The model-predicted curves are also sensitive to the value used for the initial aperture on the first loading cycle. The model predicts an initial aperture of $425 \mu\text{m}$ using equation (4-12). This is a reasonable estimate considering the measured aperture at 1 MPa for the resin (fifth) loading cycle was $103 \mu\text{m}$. However, decreasing the initial aperture by one half lowers the predicted flow rates by one to two orders of magnitude. Unfortunately, the true initial apertures of natural fractures are difficult to determine precisely.

Finally, the effects of changing the JRC and JCS parameters were studied to determine the relative sensitivity of the model curves to these two parameters and also to determine if a better fit to the experimental data could be obtained. Decreasing the JRC shifts the normal closure curves in Figure 4.12 to the left and reduces the hysteresis between the first and second cycles. This also has the effect of lowering the flow rate curves in Figure 4.13. For example, a JRC of 2.5 gives a better approximation of the measured flow rate data, especially for the first cycle, but would imply a very smooth fracture surface. Increasing the JRC, i.e making the surface rougher, basically has the opposite effect on the model curves but to a lesser degree.

Decreasing the JCS shifts the normal closure curves to the right; increasing the JCS moves them to the left. For example, a small decrease in the JCS from 119 MPa to 110 MPa increased the maximum closure on the first loading cycle by about $50 \mu\text{m}$. The predicted flow rates were not very sensitive to increasing or decreasing

the JCS with changes less than an order of magnitude either way when the JCS was cut in half or made to equal σ_c . Overall, a good fit to both the normal closure data and the measured flow rates could not be obtained using any combination of JRC and JCS values.

Chapter 5 SUMMARY AND CONCLUSIONS

The results of laboratory stress-flow tests on the medium-sized granite core used in this study are typical of the mechanical and hydraulic behaviour of single, natural fractures under applied normal stresses. In these tests, a relatively undisturbed natural fracture was subjected to four complete uniaxial compressive loading and unloading cycles at normal stresses up to 30 MPa. The most significant observation was the highly nonlinear relationship between normal stress, fracture closure and fracture flow rate. Rapid closure of the fracture and corresponding rapid reductions in flow rates were observed at low normal stresses followed by more gradual fracture closure and relatively constant flow rates at higher stresses. Permanent reductions in both closure and flow rates occurred between each successive cycle. Even after four loading cycles, and an apparent high degree of mating of the two fracture surfaces, the fracture could not be closed and small but significant flow rates could be measured.

The primary reason for the observed behaviour is due to surface roughness effects. Roughness controls the deformation of the fracture by creating points of contact between asperities on the adjoining surfaces while at the same time controlling the movement of fluids in the fracture by channelling flow through the parts of the fracture that remain open. As the normal stress changes, so does the distribution and shape of contacting asperities and fracture void space. While the effects of roughness are easily observed, the actual measurement of the geometrical

aspects of a fracture under stress is difficult. To accomplish this task, the fracture was loaded to a reference stress of 1 MPa after the final loading cycle and injected with an epoxy resin to bond the fracture together. The resin injection experiment enabled direct measurements of the roughness of both sides of the fracture, contact area and void space under known stress-flow conditions.

Two scales of roughness were measured from fracture profiles generated from the resin work; a large-scale roughness or waviness and a superimposed small-scale roughness or jaggedness. Large-scale asperity heights were of the order of 1 mm while small-scale asperity heights were of the order of 0.1 mm. In both cases, the asperity height distributions were well approximated by either a normal or log-normal distribution. The large-scale asperity height distributions for top and bottom surfaces were not mirror images of each other indicating some degree of mismatch between the two surfaces. Small-scale roughness was more uniform as evidenced by similar asperity height distributions for both surfaces. For mated or nearly-mated surfaces in contact, small-scale roughness has the most important effect on fracture flow by forming protrusions into the fracture plane that increase the resistance to fluid movement and by creating a series of tortuous flow channels around areas of contact. The measured contact area for the fracture used in this study was 5.3% at 1 MPa on the fifth loading cycle. The individual contact points were spread unevenly throughout the fracture plane with a mean contact length (in cross-section) of 1 mm.

Even at this low stress, the effects of contacting asperities in separating the fracture into smaller connected and unconnected flow channels were clearly observed.

The resin impregnation technique also enabled measurement of the variable aperture and irregular void spaces imparted by fracture roughness. The real fracture aperture was found to be highly irregular along the length of the fracture profile. The distribution of local apertures was skewed towards zero with a mean value of about 0.1 mm. The average measured aperture was more than an order of magnitude higher than the theoretical hydraulic aperture calculated using the parallel plate model yet the measured flow rates were lower than those predicted from the parallel plate relationship. This observation would suggest that the total volume of fluid contained in the fracture is greater than that implied by the parallel plate model, and that flow rate is not simply related to an average aperture.

If the fracture is thought of as a series of voids between areas of contact rather than two surfaces with some mean separation, a better understanding of how fluids move through the fracture is obtained. These voids are elongated, irregularly-shaped blebs that pinch out and are discontinuous in the plane of the profile, but may be continuous in the orthogonal direction. Fluids move through the fracture by following series of voids that are joined together to create flow channels or large aperture regions within the fracture plane. The size and shape of the fracture voids measured in this study were characterized in terms of cross-sectional area and aspect ratio respectively. The mean void size was determined to be about 1 mm^2 with most

of the voids being less than 2 mm^2 in cross-sectional area. The mean aspect ratio was about 7 indicating that the voids are flattened ellipses in the plane of the fracture. Both distributions were skewed and could be somewhat approximated by a log-normal distribution. The data measured from the resin work can be combined to show the spatial distribution of fracture aperture and void space as given by the two-dimensional contour plot in Figure 3.23 and the three-dimensional mesh diagram in Figure 3.25.

By far the most common approach to describing fluid flow in fractures has utilized the parallel plate analogy in which the two sides of the fracture are idealized as smooth, parallel surfaces. The fracture flow rate can be shown to be a function of the cube of the parallel plate aperture, also known as the cubic law. Even with modifications to account for roughness effects, the cubic law has only found limited success when applied to rough fractures in contact yet it has become firmly entrenched in the literature as the governing equation for fracture flow. The results of this study have shown that the cubic law is not valid for natural fractures. Figure 3.3 shows that the aperture-flow relationship deviates significantly from the cubic law, especially at high stresses and with increasing number of loading cycles. This same conclusion has been reached from other tests of natural fractures (Gale, 1982; Raven and Gale, 1985; Pyrak-Nolte et al., 1987; Gentier, 1990b). These findings suggest that the stress-flow relationship must be more complex than the cubic law implies with surface roughness, contact area, tortuosity and void space geometry all playing

an important role. The data obtained from these experiments have quantified some of these parameters and provide the basis for evaluating theoretical and experimental stress-flow models that exist in the literature. Examined in this study were the theoretical models proposed by Gangi (1978), Tsang and Witherspoon (1981), Walsh (1981) and Swan (1983) and the empirical model of Barton et al. (1985). All of the models were found to have serious limitations and only provided a semi-quantitative prediction of measured flow rates at best. The Gangi bed of nails model is essentially an asperity contact model that does not take into account the deformation of the fracture voids and tortuosity effects created by increased normal stress. The assumption of a constant contact area ratio proved to be a major limitation and attempts at modelling fracture flow rates were essentially curve-fitting exercises using adjustable parameters. Tsang and Witherspoon introduced a void-asperity model in which fracture closure was described in terms of deformation of the voids and aperture distribution as a function of asperities in contact. Both processes are related through a geometrical characterization of fracture roughness which leads to the calculation of a statistical average aperture to be used in the cubic law for flow rate as a function of normal stress. This modified cubic law was found to predict flow rates that were up to two orders of magnitude larger than measured flow rates. The model does not account for tortuosity effects.

Walsh and Swan both present coupled normal closure - conductivity models that incorporate surface roughness effects. Hertzian contact theory is used to relate

linear normal stiffness behaviour to the standard deviation of asperity heights - Walsh assuming an exponential asperity height distribution, Swan using actual roughness measurements. The models were extended to include contact area and aperture changes and hence hydraulic conductivity as a function of normal stress. Unfortunately, the assumption of linear normal stiffness has been shown not to be valid for natural fractures with mated or near-mated surfaces. If normal stiffness was assumed to be linear, at least over the lower stress range, some quantitative agreement was found between predicted and measured flow rates.

The Barton-Bandis empirical model characterizes the complete normal stress-closure-conductivity behaviour of fractures using a few basic input parameters determined from simple index tests on the rock in question. The model predicted behaviour showed some agreement with the measured normal closure behaviour in this study but overestimated the measured flow rates. This probably has to do with the fact the cubic law is used as the governing equation for fracture flow in the model. As far as ease of application is concerned and overall results, the Barton-Bandis model was found to be as useful as any of the theoretical models. The theoretical models require elaborate input data such as fracture closure tests, material property tests, surface roughness measurements or permeability tests at a given reference stress to test the models. The input for the Barton-Bandis model can be derived from comparatively simple index tests on pieces of fractured and intact rock cores.

The results from this study, including the model comparisons, have highlighted several conclusions that are fundamental to developing a complete fracture-flow theory. The first involves the concept of fracture aperture. Several definitions of fracture aperture are found in the literature, eg. effective fracture aperture, hydraulic aperture, real mechanical aperture, theoretical conducting aperture, mean aperture and equivalent uniform aperture. This has led to some confusion and has resulted in a variety of interpretations of the role of fracture aperture in stress-flow behaviour. One thing that is clear is that the fracture aperture cannot be represented by some single value and that it is the spatial distribution of apertures that is more important. The parallel plate model does not take the spatial distribution of apertures into account and hence does not model tortuosity effects. Unfortunately, all of the stress-flow models discussed above have used the parallel plate model for relating fracture aperture to fracture flow rates.

Secondly, any attempt at modelling stress-flow behaviour must consider both sides of the fracture. True measurements of surface roughness, contact area and aperture variations and their spatial distributions must include both sides of the fracture under different normal stress conditions. These measurements can then be combined with mechanical and hydraulic test results to understand fracture flow behaviour. Most of the work on stress-flow behaviour reported in the literature, including the models discussed above, have only considered one side of the fracture.

Thirdly, there are different scales of roughness and it is necessary to determine what scale is important for fluid flow considerations. This has important implications for the measurement and characterization of fracture roughness. It would appear that large-scale roughness has a much lesser impact on fluid flow than does the small-scale roughness features which tend to be of the same order as the fracture aperture itself. The fractal approach, which has recently gained a lot of attention in the literature, may be useful if the link between fractal roughness and fracture flow rates can be made.

The resin injection technique described in this study offers a method for addressing these issues. It has enabled quantitative measurements of surface roughness, contact area and void space for a fracture under stress. Measurements of this kind are necessary for understanding the processes involved in fracture-flow behaviour. It appears that this information has been lacking in the development of existing models and as a result no satisfactory quantitative modelling of the stress-flow behaviour of fractured rock from an analysis of surface roughness characteristics currently exists. It is recognized that there are some limitations to the resin injection technique. The method is a one-time only procedure that provides a "snapshot" of the fracture at a given stress. This negates the possibility of comparing other "snapshots" from the same sample. The method is also time consuming and does not lend itself easily to the testing of a great number of samples. However, if enough tests are done on different fractures over a range of different stresses and the

number of profiles needed to characterize the fracture can be reduced to a minimum, the method has the potential of providing the experimental data base necessary for developing a suitable stress-flow model. Fracture flow theory is lagging behind practice. It is hoped that studies like this will help close this gap.

REFERENCES

- Baker, W.J., 1955. Flow in fissured formations; *in* Proceedings of the 4th World Petroleum Congress, Rome, Section II/E, Paper 7, pp. 379-393.
- Bandis, S. Lumsden, A.C. and Barton, N.R., 1983. Fundamentals of Rock Joint Deformation; *International Journal of Rock Mechanics and Mining Sciences & Geomechanics Abstracts*, v. 20, no. 6, pp. 249-268.
- Barton, N.R., 1971. A Relationship Between Joint Roughness and Joint Shear Strength; *in* Rock Fracture, Proceedings of the International Symposium on Rock Mechanics, Nancy, International Society for Rock Mechanics, v.I, paper 1-8.
- Barton, N., 1973. Review of a New Shear-Strength Criterion for Rock Joints; *Engineering Geology*, v. 7, pp. 287-332.
- Barton, N. and Bandis, S., 1982. Effects of Block Size on the Shear Behaviour of Jointed Rock; Keynote Lecture, *in* Proceedings of the 23rd U.S. Symposium on Rock Mechanics, Berkeley.
- Barton, N. and Bakhtar, K., 1983. Rock Joint Description and Modeling for the Hydrothermomechanical Design of Nuclear Waste Repositories; Internal Reports TRE 83-10 and TRE 83-12, Submitted to CANMET, Mining Research Laboratories, Ottawa.
- Barton, N., Bandis, S. and Bakhtar, K., 1985. Strength, Deformation and Conductivity Coupling of Rock Joints; *International Journal of Rock Mechanics and Mining Sciences & Geomechanics Abstracts*, v. 22, no. 3, pp. 121-140.
- Brar, N.S. and Stesky, R.M., 1980. Permeability of Intact and Jointed Rock; *EOS*, v. 61 (46), pp. 1112.
- Brown, S.R., 1984. Fundamental Study of the Closure Property of Joints; Ph.D. Thesis, Columbia University, New York, 234 pp.
- Brown, S.R., 1987. Fluid Flow Through Rock Joints: The Effects of Surface Roughness; *Journal of Geophysical Research*, v. 92, no. B2, pp. 1337-1347.

- Bury, K.V., 1975. *Statistical Models In Applied Science*; John Wiley & Sons, New York, 625 pp.
- Carr, J.R. and Warriner, J.B., 1987. Rock Mass Classification Using Fractal Dimension; *in* Proceedings of the 28th U.S. Symposium on Rock Mechanics, Tucson, pp. 73-80.
- Chambers, J.M., Cleveland, W.S., Kleiner, B. and Tukey, P.A., 1983. *Graphical Methods for Data Analysis*; Wadsworth International Group, Belmont, California, 395 pp.
- Dight, P.M. and Chiu, H.K., 1981. Prediction of Shear Behaviour of Joints Using Profiles; *International Journal of Rock Mechanics and Mining Sciences & Geomechanics Abstracts*, v. 18, pp. 369-386.
- Engelder, T. and Scholz, C.H., 1981. Fluid Flow Along Very Smooth Joints at Effective Pressures up to 200 Megapascals; *in* Mechanical Behaviour of Crustal Rocks, American Geophysical Union, Monograph 24, pp. 147-152.
- Elliott, G.M., Brown, E.T., Boodt, P.I. and Hudson, J.A., 1985. Hydromechanical behaviour of joints in the Carnmenellis granite, S.W. England; *in* Proceedings of the International Symposium on Fundamentals of Rock Joints, Bjorkliden, Sweden, ed. O. Stephansson, International Society for Rock Mechanics, pp. 249-258.
- Fecker, E., 1978. Geotechnical Description and Classification of Joint Surfaces; *Bulletin of the International Association of Engineering Geologists*, v. 18, pp. 111-120.
- Gale, J.E., 1975. A Numerical, Field and Laboratory Study of Flow in Rocks With Deformable Fractures; Ph.D. Thesis, University of California, Berkeley, 255 pp.
- Gale, J.E., 1982. The Effects of Fracture Type (Induced Versus Natural) on the Stress, Fracture-Closure, Fracture-Permeability Relationships; *in* Proceedings of the 23rd U.S. Symposium on Rock Mechanics, Berkeley, pp. 290-298.
- Gale, J.E., 1984. Changes in Fracture Permeability as a Function of Sample Size, Fracture Type, and Stress History; *in* Proceedings of the International Symposium on Groundwater Utilization and Contaminant Hydrogeology, Montreal, International Association of Hydrogeologists, v.1, pp.43-53.

- Gale, J.E., 1985. Hydraulic Properties of Fractures; *in* Proceedings of the 17th International Congress of the International Association of Hydrogeologists, Tucson, v. XVII, part 1, pp. 1-16.
- Gale, J.E., 1987. Comparison of coupled fracture deformation and fluid flow models with direct measurements of fracture pore structure and stress-flow properties; *in* Proceedings of the 28th U.S. Symposium On Rock Mechanics, Tucson, pp. 1213-1222.
- Gale, J.E. and Raven, K.G., 1980. Effects of Sample Size on the Stress-Permeability Relationship for Natural Fractures; Technical Information Report No. 48, Swedish-American Cooperative Program on Radioactive Waste Storage in Mined Caverns in Crystalline Rock, Lawrence Berkeley Laboratory Report LBL-11865, Berkeley, 111 pp.
- Gangi, A.F., 1978. Variation of Whole and Fractured Porous Rock Permeability With Confining Pressure; *International Journal of Rock Mechanics and Mining Sciences & Geomechanics Abstracts*, v. 15, pp. 249-257.
- Gangi, A.F., 1981. The Variation of Mechanical and Transport Properties of Cracked Rock with Pressure; *in* Proceedings of the 22nd U.S. Symposium On Rock Mechanics, Cambridge, pp. 91-95.
- Gentier, S., 1990a. Morphological Analysis of a Natural Fracture; *in* Selected Papers on Hydrogeology from the 28th International Geological Congress, Washington, D.C., U.S.A., July, 1989, International Association of Hydrogeologists, ed. E.S. Simpson and J.M. Sharp, Jr., v. 1, pp. 315-326.
- Gentier, S., 1990b. Hydromechanical Behaviour of a Single Natural Fracture under Normal Stress; *in* Selected Papers on Hydrogeology from the 28th International Geological Congress, Washington, D.C., U.S.A., July, 1989, International Association of Hydrogeologists, ed. E.S. Simpson and J.M. Sharp, Jr., v. 1, pp. 327-338.
- Gerald, C.F and Wheatley, P.O., 1984. Applied Numerical Analysis (Third Edition); Addison-Wesley Publishing Co., Reading, Mass., 579 pp.
- Goodman, R.E., 1976. Methods of Geological Engineering in Discontinuous Rocks; West Publishing Co., St. Paul, Minn., 472 pp.

- Greenwood, J.A. and Williamson, J.B.P., 1966. Contact of Nominally Flat Surfaces; Proceedings of the Royal Society of London - Series A, v. 295, no. 1442, pp. 300-319.
- Greenwood, J.A. and Tripp, J.H., 1971. The Contact of Two Nominally Flat Rough Surfaces; Proceedings of the Institution of Mechanical Engineers, v. 185, pp. 625-633.
- Herdocia, A., 1985. Direct shear tests of artificial joints; in Proceedings of the International Symposium on Fundamentals of Rock Joints, Bjorkliden, Sweden, ed. O. Stephansson, International Society for Rock Mechanics, pp. 123-132.
- Hopkins, D.L., Cook, N.G.W. and Myer, L.R., 1987. Fracture stiffness and aperture as a function of applied stress and contact geometry; in Proceedings of the 28th U.S. Symposium on Rock Mechanics, Tucson, pp. 673-680.
- Huitt, J.L., 1956. Fluid Flow in Simulated Fractures; American Institute of Chemical Engineering Journal, v. 2, pp. 259-263.
- Hutson, R.W. and Dowding, C.H., 1987. Computer Controlled Cutting of Multiple Identical Joints in Real Rock; Rock Mechanics and Rock Engineering, v. 20, no. 1, pp. 39-55.
- ISRM Suggested Methods, 1978. Suggested Methods for the Quantitative Description of Discontinuities in Rock Masses; International Society for Rock Mechanics Commission on Standardization of Laboratory and Field Tests, International Journal of Rock Mechanics and Mining Sciences & Geomechanics Abstracts, v. 15, pp. 319-368.
- Iwai, K., 1976. Fundamental Studies of Fluid Flow Through a Single Fracture; Ph.D. Thesis, University of California, Berkeley, 208 pp.
- Jackson, R., Annor, A., Wong, A.S. and Betournay, M., 1985. Preliminary Results of Rock Joint Testing on URL Core; Division Report ERP/MRL 85-14(TR), CANMET, Energy, Mines and Resources, Canada, 38 pp.
- Jones, F.O., 1975. A Laboratory Study of the Effects of Confining Pressure on Fracture Flow and Storage Capacity in Carbonate Rocks; Journal of Petroleum Technology, January, pp. 21-27.

- Krahn, J. and Morgenstern, N.R., 1979. The Ultimate Frictional Resistance of Rock Discontinuities; *International Journal of Rock Mechanics and Mining Sciences & Geomechanics Abstracts*, v. 16, pp. 127-133 and *Authors' Reply*, v. 17, p. 79.
- Kranz, R.L., Frankel, A.D., Engelder, T. and Scholz, C.H., 1979. The Permeability of Whole and Jointed Barre Granite; *International Journal of Rock Mechanics and Mining Sciences & Geomechanics Abstracts*, v. 16, pp. 225-235.
- Lam, T.S.K. and Johnston, I.W., 1985. A Scanning Device to Quantify Joint Surface Roughness; *Geotechnical Testing Journal*, v. 8, no. 3, pp. 117-124.
- Lee, Y.H., Carr, J.R., Barr, D.J. and Haas, C.J., 1990. The Fractal Dimension as a Measure of the Roughness of Rock Discontinuity Profiles; *International Journal of Rock Mechanics and Mining Sciences & Geomechanics Abstracts*, v. 27, n.6, pp. 453-464.
- Lomize, G., 1951. *Water Flow in Jointed Rock* (in Russian); All-Union Energetics Publishers, Moscow, 127 pp.
- Louis, C., 1969. *A Study of Groundwater Flow in Jointed Rock and Its Influence on the Stability of Rock Masses*; Imperial College Rock Mechanics Research Report No. 10, London, 90 pp.
- Maini, Y.N.T., 1971. *In Situ Hydraulic Parameters in Jointed Rock - Their Measurement and Interpretation*; Ph.D. Thesis, University of London, Imperial College, London.
- Mandelbrot, B.B., 1977. *Fractals*; W.H. Freeman Co., New York, 365 pp.
- Nelson, R.A. and Handin, J.W., 1977. Experimental Study of Fracture Permeability in Porous Rock; *American Association of Petroleum Geologists Bulletin*, v. 61, no. 2, pp. 227-236.
- Neuzil, C.E. and Tracy, J.V., 1981. Flow Through Fractures; *Water Resources Research*, v. 17, no. 1, pp. 191-199.
- Nolte, D.D., Pyrak-Nolte, L.J. and Cook, N.G.W., 1987. The Fractal Geometry of the Flow Paths in Natural Fractures in Rock and the Approach to Percolation; Preprint submitted to PAGEOPH - Special Issue on Fractals in Geophysics.

- Patton, F.D., 1966. Multiple Modes of Shear Failure in Rock; *in* Proceedings of the 1st Congress of the International Society for Rock Mechanics, Lisbon, v. 1, pp. 509-513.
- Pearce, R. and Murphy, H., 1979. Roughness Effects on Flow in Hydraulic Fractures: Survey of the Literature; Unpublished Report, Los Alamos Scientific Laboratory, University of California, Los Alamos, 37 pp.
- Piteau, D.R., 1971. Geological Factors Significant to the Stability of Slopes Cut in Rock; *in* Symposium on Planning Open Pit Mines, Johannesburg, 1970, Balkema, Amsterdam, 1971, pp. 33- 53.
- Pratt, H.R., Swolfs, H.S., Brace, W.F., Black, A.D. and Handin, J.W., 1977. Elastic and Transport Properties of an In Situ Jointed Granite; *International Journal of Rock Mechanics and Mining Sciences & Geomechanics Abstracts*, v. 14, no. 1, pp. 35-45.
- Pyrak-Nolte, L.T., Myer, L.R., Cook, N.G.W. and Witherspoon, P.A., 1987. Hydraulic and Mechanical Properties of Natural Fractures in Low Permeability Rock; *in* Proceedings of the 6th Congress of the International Society for Rock Mechanics, Montreal, v. 1, pp. 225-231.
- Raven, K.G. and Gale, J.E., 1985. Water Flow in a Natural Rock Fracture as a Function of Stress and Sample Size; *International Journal of Rock Mechanics and Mining Sciences & Geomechanics Abstracts*, v. 22, no. 4, pp. 251-261.
- Reeves, M.J., 1985. Rock Surface Roughness and Frictional Strength; *International Journal of Rock Mechanics and Mining Sciences & Geomechanics Abstracts*, v. 22, no. 6, pp. 429-442.
- Rengers, N., 1970. Influence of Surface Roughness on the Friction Properties of Rock Planes; *in* Proceedings of the 2nd Congress of the International Society for Rock Mechanics, Belgrade, paper 1-31.
- Rissler, P., 1978. Determination of the Water Permeability of Jointed Rock; (English edition), Vol. 5, Publications of the Institute for Foundation Engineering, Soil Mechanics, Rock Mechanics and Water Ways Construction, RWTH (University) Aachen, Federal Republic of Germany, ed. W. Wittke, 150 pp.
- Romm, J.S., 1966. Flow Phenomena in Fissured Rock (in Russian); Moscow, 248 pp.

- Sakellariou, M., Nakos, B. and Mitsakaki, C., 1991. On the Fractal Character of Rock Surfaces; Technical Note, International Journal of Rock Mechanics and Mining Sciences & Geomechanics Abstracts, v. 28, n. 6, pp. 527-533.
- Sato, K., Watanabe, K. and Kotajima, N., 1984. Fundamental Study on Flow Resistance in Rock Fissures; Soils and Foundations, v. 24, no. 1, pp. 1-8.
- Sharp, J.C., 1970. Fluid Flow Through Fissured Media; Ph.D. Thesis, University of London, Imperial College, London, 181 pp.
- Sharp, J.C. and Maini, Y.N.T., 1972. Fundamental Considerations on the Hydraulic Characteristics of Joints in Rock; in Percolation Through Fissured Rock, Proceedings of the International Symposium on Rock Mechanics, Stuttgart, International Society for Rock Mechanics, Paper T1-F, pp. 1-15.
- Stimpson, B., 1982. A Rapid Field Method For Recording Joint Roughness Profiles; International Journal of Rock Mechanics and Mining Sciences & Geomechanics Abstracts, v. 19, pp. 345-346.
- Sun, Z., 1985. Asperity Models for Closure and Shear; in Proceedings of the International Symposium on Fundamentals of Rock Joints, Bjorkliden, Sweden, ed. O. Stephansson, International Society for Rock Mechanics, pp. 173-183.
- Swan, G., 1980. Stiffness and associated joint properties of rock; in Proceedings of the Conference on Application of Rock Mechanics to Cut and Fill Mining, University of Lulea, Sweden, June 1-3, 1980, Institute of Mining and Metallurgy, London, pp. 169-178.
- Swan, G., 1981. Tribology and the Characterisation of Rock Joints; in Proceedings of the 22nd U.S. Symposium on Rock Mechanics, Boston, pp. 432-437.
- Swan, G., 1983. Determination of Stiffness and Other Joint Properties From Roughness Measurements; Rock Mechanics and Rock Engineering, v. 16, pp. 19-38.
- Thomas, T.R. (editor), 1982. Rough Surfaces; Longman Inc., New York, 261 pp.
- Thorpe, R.K., 1986. Experimental Characterization of the Hydraulic and Mechanical Behaviour of a Jointed Rock Specimen; Ph.D. Thesis, University of California, Berkeley, 188 pp.

- Tsang, Y.W. and Witherspoon, P.A., 1981. Hydromechanical Behavior of a Deformable Rock Fracture Subject to Normal Stress; *Journal of Geophysical Research*, v. 86, no. B10, pp. 9287-9298.
- Tsang, Y.W. and Witherspoon, P.A., 1982. Correlations Between Fracture Mechanical and Fluid Flow Properties; *in Proceedings of the 23rd U.S. Symposium on Rock Mechanics, Berkeley*, pp. 560-567.
- Tsang, Y.W. and Witherspoon, P.A., 1983. The Dependence of Fracture Mechanical and Fluid Flow Properties on Fracture Roughness and Sample Size; *Journal of Geophysical Research*, v. 88, no. B3, pp. 2359-2366.
- Tsang, Y.W. and Witherspoon, P.A., 1985. Effects of Fracture Roughness on Fluid Flow Through a Single Deformable Fracture; *in Proceedings of the 17th International Congress of the International Association of Hydrogeologists, Tucson*, v. XVII, part 2, pp. 683-694.
- Tse, R. and Cruden, D.M., 1979. Estimating Joint Roughness Coefficients; *International Journal of Rock Mechanics and Mining Sciences & Geomechanics Abstracts*, v. 16, pp. 303-307.
- Turk, N. and Dearman, W.R., 1985. Investigation of Some Rock Joint Properties: Roughness Angle Determination and Joint Closure; *in Proceedings of the International Symposium on Fundamentals of Rock Joints, Bjorkliden, Sweden*, ed. O. Stephansson, International Society for Rock Mechanics, pp. 197-204.
- Voegele, M., Hardin, E., Lingle, D., Board, M. and Barton, N., 1981. Site Characterization of Joint Permeability Using the Heated Block Test; *in Proceedings of the 22nd U.S. Symposium on Rock Mechanics, Boston*, pp. 126-133.
- Voss, C.F., Bastian, R.J. and Shotwell, L.R., 1986. A Coupled Mechanical - Hydrological Methodology For Modeling Flow in Jointed Rock Masses Using Laboratory Data for the Joint Flow Model; *in Proceedings of the 27th U.S. Symposium on Rock Mechanics, University of Alabama*, pp. 906-909.
- Walsh, J.B., 1981. Effect of Pore Pressure and Confining Pressure on Fracture Permeability; *International Journal of Rock Mechanics and Mining Sciences & Geomechanics Abstracts*, v. 18, pp. 429-435.

- Walsh, J.B. and Grosenbaugh, M.A., 1979. A New Model For Analyzing the Effect of Fractures on Compressibility; *Journal of Geophysical Research*, v. 84, no. B7, pp. 3532-3536.
- Wang, J.S.Y., Narasimhan, T.N. and Scholz, C., 1988. Aperture Correlation of a Fractal Fracture; *Journal of Geophysical Research*, v. 93, no. B3, pp. 2216-2224.
- Westerman, A.R., Reeves, M.J. and Attewell, P.B., 1982. Rock Surface Roughness and Discontinuity Closure at Depth; *Developments in Geotechnical Engineering*, v. 32, pp. 63-67.
- Witherspoon, P.A., Wang, J.S.Y., Iwai, K. and Gale, J.E., 1980. Validity of the Cubic Law for Fluid Flow in a Deformable Rock Fracture; *Water Resources Research*, v. 16, no. 6, pp. 1016-1024.
- Wong, T., Fredrich, J.T. and Gwanmesia, G.D., 1989. Crack Aperture Statistics and Pore Space Fractal Geometry of Westerly Granite and Rutland Quartzite: Implications for an Elastic Contact Model of Rock Compressibility; *Journal of Geophysical Research*, v. 94, no. B8, pp. 10,267-10,278.
- Wu, T.H. and Ali, E.M., 1978. Statistical Representation of Joint Roughness; *International Journal of Rock Mechanics and Mining Sciences & Geomechanics Abstracts*, v. 15, pp. 259-262.
- Zimmerman, R.W., Kumar, S. and Bodvarsson, G.S., 1991. Lubrication Theory Analysis of the Permeability of Rough-Walled Fractures; *International Journal of Rock Mechanics and Mining Sciences & Geomechanics Abstracts*, v. 28, n. 4, pp. 325-331.

APPENDIX A
STRESS - FLOW DATA

STRESS = Applied normal stress (MPa)

dH = Head differential (cm)

Q/dH = Normalized flow rate (cm²/s)

LVDT 90 = Displacement measured with LVDT at 90° position (μm)

LVDT 210 = Displacement measured with LVDT at 210° position (μm)

LVDT 330 = Displacement measured with LVDT at 330° position (μm)

LVDT ROCK = Displacement measured with LVDT on intact rock (μm)

S.G.#x = Strain measured with strain gauge #x (μe)

T-H2O = Water temperature (°C)

T-AIR = Air temperature (°C)

deltaFR = Average fracture+rock deformation (μm)

deltaF = Average fracture deformation (μm)

2bs = Smooth hydraulic aperture (μm)

2br = Rough hydraulic aperture (μm)

STRESS (MPa)	dH (cm)	Q/dH (cm ² /s)	LVDT 90 (um)	LVDT 210 (um)	LVDT 330 (um)	LVDT ROCK (um)
FINAL						
0.00			0.00	0.00	0.00	0.00
0.26	217.5	9.77E-05	47.20	27.43	29.15	-1.11
0.66	255.5	4.82E-06	57.89	44.29	42.10	-1.05
1.14	318.9	3.22E-06	61.11	53.32	49.58	-0.94
3.10	410.6	2.54E-06	69.00	68.32	66.46	0.87
7.03	398.9	2.17E-06	78.56	81.79	83.83	3.40
9.91	389.7	2.04E-06	84.06	88.65	91.97	5.60
20.32	381.9	1.79E-06	101.82	108.83	110.66	12.61
30.09	373.9	1.54E-06	115.72	123.66	122.75	18.89
20.34	368.1	1.62E-06	106.74	113.18	115.42	11.41
9.95	361.5	1.78E-06	93.01	100.41	102.32	3.53
3.11	354.0	2.15E-06	78.78	87.21	82.00	-1.79
1.13	315.8	2.77E-06	70.75	71.00	64.12	-2.89
0.28	340.2	9.06E-06	53.16	39.84	40.29	-3.23
RESI ^m						
0.00			0.00	0.00	0.00	0.00
0.21	313.1	6.51E-06	44.01	25.99	20.76	0.21
0.40	309.1	3.61E-06	53.96	38.59	29.17	0.35
0.60	327.4	3.29E-06	59.30	47.97	34.34	0.36
0.80	317.4	2.99E-06	61.72	54.29	38.59	0.32
1.01	304.7	2.87E-06	63.38	58.72	42.29	0.19

STRESS (MPa)	S.G.#1 (ue)	S.G.#2 (ue)	S.G.#3 (ue)	S.G.#4 (ue)	S.G.#5 (ue)	S.G.#6 (ue)
FINAL						
0.00	0.00	0.00	0.00	0.00	0.00	0.00
0.26	-34.72	-30.48	-199.87	5.97	6.52	9.63
0.66	-25.37	-41.19	-275.92	7.26	9.67	11.21
1.14	-19.96	-42.08	-339.36	9.40	14.85	-12.28
3.10	-15.65	-46.15	-383.48	2.06	24.22	6.58
7.03	-3.92	-75.17	-462.41	-22.52	28.60	-18.45
9.91	-12.68	-96.07	-485.29	-38.43	32.07	-32.76
20.32	-7.90	-150.28	-606.31	-106.39	19.81	-109.94
30.09	-22.18	-174.93	-390.78	-177.41	-9.12	-185.12
20.34	-21.26	-92.00	-131.54	-91.19	42.34	-85.08
9.95	26.32	-5.69	-75.22	-16.04	71.68	9.09
3.11	75.47	59.88	-121.95	35.41	76.34	73.20
1.13	72.78	86.18	-233.85	52.93	83.65	101.09
0.28	72.72	101.58	-267.22	59.50	89.12	119.34
RESIN						
0.00	0.00	0.00	0.00	0.00	0.00	0.00
0.21	30.32	6.01	-84.28	7.93	15.53	3.30
0.40	49.98	8.71	-97.96	9.98	19.79	2.99
0.60	61.68	15.35	39.89	14.58	28.27	5.16
0.80	71.00	20.53	99.52	17.99	33.86	5.39
1.01	52.36	25.01	694.93	21.32	41.16	7.80

STRESS (MPa)	S.G.#7 (ue)	S.G.#8 (ue)	S.G.#9 (ue)	S.G.#10 (ue)	S.G.#11 (ue)	S.G.#12 (ue)
FINAL						
0.00	0.00	0.00	0.00	0.00	0.00	0.00
0.26	82.53	1.48	0.97	2.22	-0.60	-0.83
0.66	329.87	-1.03	-1.71	2.59	-10.33	-1.39
1.14	482.89	-1.54	-6.04	3.65	-19.95	-1.66
3.10	628.39	0.28	-26.78	8.44	-55.12	-0.96
7.03	752.03	5.42	-67.58	16.96	-121.79	4.75
9.91	921.84	11.51	-95.45	24.53	-167.81	11.12
20.32	943.17	36.05	-210.71	54.55	-315.02	41.41
30.09	1023.44	61.49	-323.94	85.23	-441.57	71.65
20.34	2362.59	36.04	-205.28	56.47	-320.35	39.49
9.95	1579.64	11.01	-92.23	28.11	-173.38	7.47
3.11	1807.33	1.14	-21.38	14.44	-57.52	-5.59
1.13	2005.89	2.85	8.63	12.89	-23.75	-4.53
0.28	2155.77	7.63	20.79	14.57	-4.19	-3.56
RESIN						
0.00	0.00	0.00	0.00	0.00	0.00	0.00
0.21	542.65	4.09	1.04	4.55	1.67	3.12
0.40	792.45	4.30	-0.61	5.39	-2.18	3.72
0.60	1372.75	6.11	-0.52	7.86	-6.24	1.98
0.80	1853.74	7.32	-2.53	9.30	-10.04	0.35
1.01	2673.63	8.32	-3.55	11.56	-14.28	-1.65

STRESS (MPa)	T-H2O (°C)	T-AIR (°C)	deltaFR (um)	deltaF (um)	2bs (um)	2br (um)
FINAL						
0.00	29.2	30.4	0.00	0.00	105.85	108.27
0.26	28.3	30.1	34.59	35.70	70.15	72.57
0.66	28.6	30.2	48.09	49.14	56.71	59.13
1.14	28.5	29.6	54.67	55.61	50.24	52.66
3.10	28.3	29.8	67.93	67.05	38.79	41.22
7.03	28.2	29.7	81.39	77.99	27.85	30.28
9.91	28.0	29.6	88.23	82.63	23.22	25.64
20.32	28.1	29.5	107.10	94.49	11.36	13.78
30.09	28.0	29.2	120.71	101.82	4.03	6.45
20.34	27.5	28.9	111.78	100.37	5.48	7.90
9.95	27.6	28.9	98.58	95.06	10.79	13.21
3.11	27.6	28.9	82.66	84.45	21.40	23.82
1.13	27.7	29.2	68.62	71.52	34.33	36.75
0.28	28.0	29.2	44.43	47.66	58.19	60.61
RESIN						
0.00	29.5	31.5	0.00	0.00	59.56	62.54
0.21	29.3	31.1	30.25	30.04	29.52	32.50
0.40	29.6	31.1	40.57	40.23	19.33	22.32
0.60	28.7	30.3	47.21	46.85	12.71	15.69
0.80	28.2	29.8	51.53	51.21	8.35	11.33
1.01	27.5	29.1	54.80	54.61	4.95	7.93

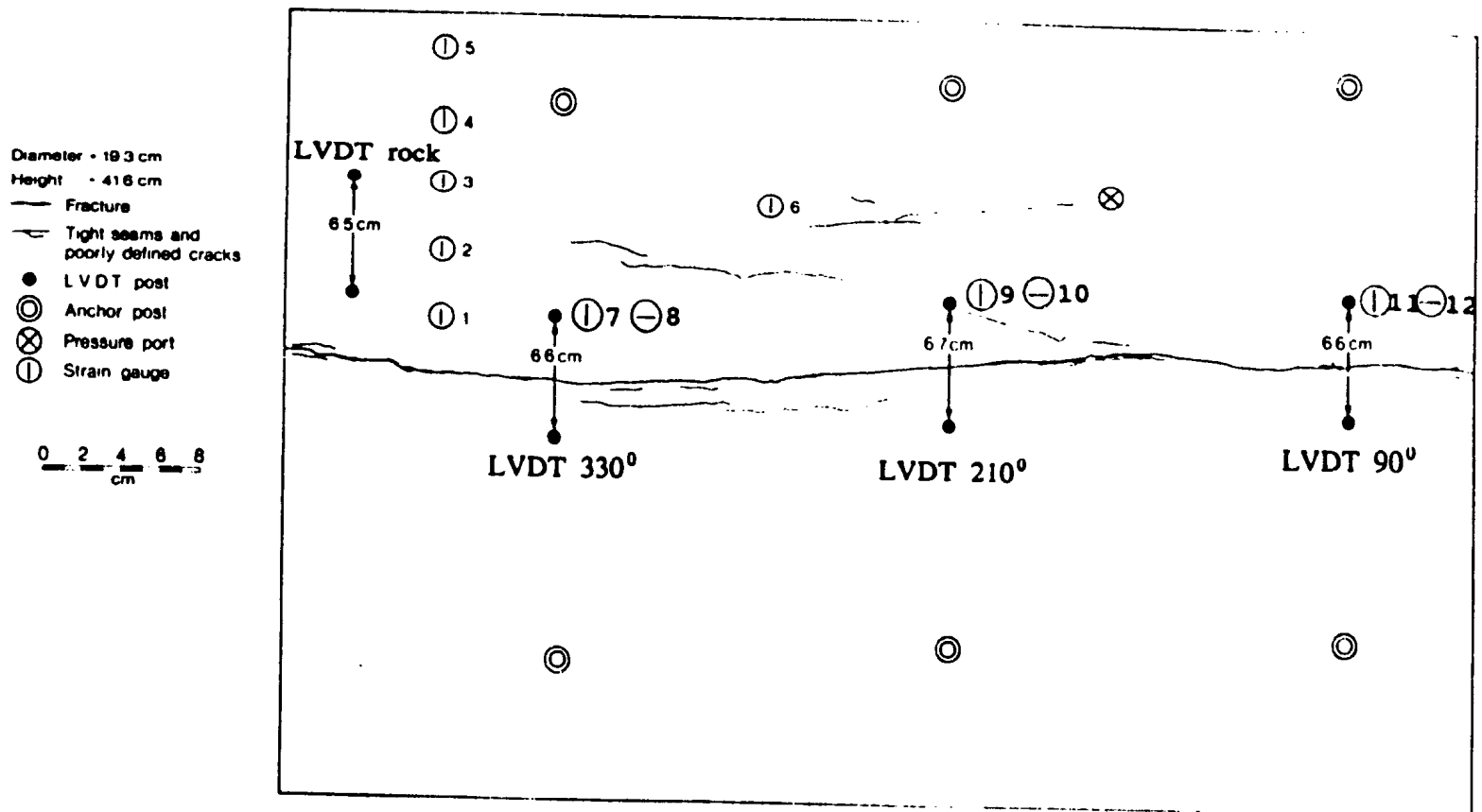


Figure A.1 Surface map of sample showing location of LVDT posts, anchor posts, pressure port and strain gauges with respect to the fracture (modified after Gale and Raven, 1980).

